ISTANBUL TECHNICAL UNIVERSITY ★ GRADUATE SCHOOL OF SCIENCE ENGINEERING AND TECHNOLOGY

NONPLANAR SLIP BOUNDARY CONDITIONS IN RAREFIED GAS FLOWS

Ph.D. THESIS

Ali DİNLER

Department of Mathematics

Mathematics Engineering Programme

OCTOBER 2012

ISTANBUL TECHNICAL UNIVERSITY ★ GRADUATE SCHOOL OF SCIENCE ENGINEERING AND TECHNOLOGY

NONPLANAR SLIP BOUNDARY CONDITIONS IN RAREFIED GAS FLOWS

Ph.D. THESIS

Ali DİNLER

Department of Mathematics

Mathematics Engineering Programme

Advisor: Doç. Dr. Kamil ORUÇOĞLU

OCTOBER 2012

İSTANBUL TEKNİK ÜNİVERSİTESİ ★ FEN BİLİMLERİ ENSTİTÜSÜ

SEYRELTİLMİŞ GAZ AKIŞLARI İÇİN EĞRİSEL YÜZEYLERDE KAYMA SINIR KOŞULLARI

DOKTORA TEZİ

Ali DİNLER

Matematik Mühendisliği Anabilim Dalı

Matematik Mühendisliği Programı

Tez Danışmanı: Doç. Dr. Kamil ORUÇOĞLU

EKİM 2012

Ali Dinler, a **Ph.D.** student of ITU at **Department of Mathematics** with a student ID **509072002**, successfully defended the **dissertation** entitled as"**NONPLANAR SLIP BOUNDARY CONDITIONS IN RAREFIED GAS FLOWS**", which he prepared after fulfilling the requirements specified in the associated legislations, before the jury whose signatures are below.

Thesis Advisor :	**Doç. Dr. Kamil ORUÇOĞLU** Istanbul Technical University	.....
Jury Members :	**Prof. Dr. Ünal ALDEMİR** Istanbul Technical University	.....
	Prof. Dr. Faruk GÜNGÖR Dogus University	.....
	Prof. Dr. Fırat Oğuz EDİS Istanbul Technical University	.....
	Doç. Dr. Ersin ÖZUĞURLU Bahcesehir University	.....

Date of Submission : 24 July 2012
Date of Defense : 1 October 2012

To my parents,

FOREWORD

The author would like to thank Assoc. Prof. Dr. Kamil Oruçoğlu for all his help and encouragement in preparation of this dissertation. The research leading to this work has been conducted at the Centre for Microfluidics and Microsystems Modelling of STFC Daresbury Laboratory in United Kingdom and the author thanks Dr. Robert Barber and Prof. Dr. David Emerson for their tremendous help. The author would also like to thank Prof. Dr. Stefan Stefanov from Bulgarian Academy of Sciences. In addition, the author is thankful to Prof. Dr. Irina Graur and Dr. Pierre Perrier for their warm welcome during the author's visit in Marseille, France, where the author studied the discrete velocity method for the solution of the Boltzmann equation. This dissertation has been subject of six international conference papers (including 28th Rarefied Gas Dynamics Conference and 1st European Micro Gas Flows Conference, which is eventually published in Journal of Applied Physics Conference series) and three journal papers (including one in Physical Review E). The research leading to this dissertation has received funding from the European Community's Seventh Framework Programme (ITN - FP7/2007-2013) under the GASMEMS project with a grant agreement no: 215504.

June 2012 Ali DİNLER

TABLE OF CONTENTS

Page

ABBREVIATIONS

BE	**:** Boltzmann equation
BGK	**:** Bhatnagar, Gross and Krook
DSMC	**:** Direct simulation Monte Carlo
DV	**:** Discrete velocity
KL	**:** Knudsen layer
MEMS	**:** Micro-electro-mechanical systems

LIST OF TABLES

Page

LIST OF FIGURES

Page

NONPLANAR SLIP BOUNDARY CONDITIONS IN RAREFIED GAS FLOWS

SUMMARY

The breakdown of the no-slip boundary condition at a fluid-solid interface and the importance of accounting for velocity slip have been recognized in micro/nanofluidics for many years. Although many gas-phase microfluidic devices contain curved surfaces, relatively little research has been conducted on the degree of slip over nonplanar surfaces, and consequently, the relationship between the curvature of the surface and the degree of boundary slip has not been understood sufficiently well. In the present study, the kinetic theory of gases, numerical solution of the Boltzmann equation and its boundary conditions in bounded domains have been investigated. Higher-order velocity-slip Navier-Stokes continuum description and a direct simulation Monte Carlo (DSMC) approach have been employed to address important issues related to the degree of boundary slip over curved surfaces. The Boltzmann equation has also been solved numerically using the discrete velocity method. The present study demonstrates the influence of the surface shape (*i.e.* convex/concave) on the velocity slip and formation of the Knudsen layer. The study considers a number of flow cases and examines the curvature effects over the convex and concave surfaces. The results reveal that the degree of slip depends effectively on the surface shape (i.e. convex/concave), with the surface curvature having an opposing effect on the boundary slip over moving concave and convex surfaces. The results also show that as surface curvature increases, the boundary slip becomes negligible over a concave surface while it becomes increasingly important over a convex surface. In addition, novel boundary slip formulae are proposed that can accurately predict the tangential velocities and boundary slips over convex and concave surfaces. These formulae are found to be in very good agreement with DSMC data for a range of accommodation coefficients and boundary curvatures. Using the corrected slip velocities at the inner and outer cylinders, the present study then reassesses the mechanism of the intriguing phenomenon of velocity inversion which has, until the present results, often been mistakenly attributed solely to the effects of boundary curvature.

The study also considers the accuracy of the velocity-slip boundary conditions. Although it is generally accepted that slip boundary conditions that are higher-order in Knudsen number (Kn) can extend the validity of slip models beyond the conventionally-accepted upper limit of Kn=0.1, the present study demonstrates that the effects of the Knudsen layer cannot explain why slip models perform poorly for nonplanar flow cases in comparison to the equivalent planar case; nor can the presence of Knudsen layers explain why slip models show larger discrepancies over convex surfaces. The study highlights the dramatic effects of curvature, and profound influence of the S-layer over convex surfaces in the accuracy of slip models. In addition, it reveals that there is a simple relationship between the shear stress exerted on the surface and the velocity defect in the Knudsen layer.

SEYRELTİLMİŞ GAZ AKIŞLARI İÇİN EĞRİSEL YÜZEYLERDE KAYMA SINIR KOŞULLARI

ÖZET

Mikro-akışlar, makro ölçekteki akışlardan önemli ölçüde farklıdır. Mikro-akışlarda, yüzey-hacim oranı yüksektir ve akışkan-yüzey etkileşimleri önem kazanmaktadır. Gaz mikro-akışları Knudsen sayısının büyüklüğüne göre sınıflandırılır. Knudsen sayısı, serbest-yol uzunluğunun karakteristik uzunluğa oranıdır. Serbest-yol uzunluğu bir gaz molekülünün başka bir gaz molekülüyle çarpışana kadar aldığı ortalama yoldur, ve molekül kütlesi, ortam sıcaklığı ve yoğunluğunun bir fonksiyonudur. Karakteristik uzunluk ise akış bölgesini belirleyen bir uzunluktur. Dolayısıyla, serbest yol sabit tutulup, akış bölgesi (karakteristik uzunluk) küçülürse Knudsen sayısı büyür. Bu durumda Knudsen sayısı *ölçek parametresi* olarak da düşünülebilir. Atmosferik koşullar altında Knudsen sayısı, küçülen karakteristik uzunluğa bağlı olarak büyük olabilir.

Knudsen sayısı 0.001'den daha küçük olduğunda, akış kaymazlık sınır koşulu kullanılarak Navier-Stokes denklemleri ile modellenebilir. Knudsen sayısının değeri 0.001 ile 0.1 arasında ise, gaz davranışı Navier-Stokes denklemlerinin kayma sınır ve sıcaklık sıçrama koşulları kullanılarak çözülmesi ile belirlenebilir. Ancak, birçok mikro-elektro-mekanik sistemler (MEMS) erken geçiş rejimi ($0.1 < \mathrm{Kn} < 1$) ve ötesinde ($\mathrm{Kn} > 1$) çalışır. Bu durum, daha yüksek Knudsen sayıları için kayma modellerinin geçerliliğinin arttırılmasını gerektirmektedir. Erken geçiş rejiminde, Newton gerilme ve Fourier ısı transferi ilişkileri yüzey üzerinde geçersiz olmaya ve gaz-yüzey etkileşimleri akış davranışını değiştirmeye başlar. Yüzey üzerinde oluşan bu etkili tabakaya Knudsen sınır tabakası denir ve hesaplamalı modellenmesi mikro-teknolojilerde giderek önem kazanmaktadır.

Mikro-teknolojilerde son gelişmeler kaymazlık sınır koşulunun birçok uygulamada geçersiz olduğunu göstermiştir. Akışkanın yüzeyde kayması, özellikle gaz mikro/nano-akışlarında sıkça görülen bir durumdur. Gerçekçi mikro gaz sistemlerinin birçoğu eğrisel yüzeyler içermesine rağmen, nispeten az sayıda çalışmada eğrisel mikro-yüzeylerde gaz davranışı incelemiştir.

Bu çalışmada öncelikle, gazların kinetik teorisi, Boltzmann denklemi ve bu denklemin sınır koşulları incelenmiştir. Boltzmann denklemi gaz kinetik teorinin temel denklemi olup gaz molekül dağılım fonksiyonunun değişimini modeller. Bütün Knudsen sayılarında ve tüm gaz akış rejimlerinde geçerlidir. Dahası, Boltzmann denkleminin çözümü olan moleküler dağılım fonksiyonu bulunduğunda; yoğunluk, hız ve sıcaklık gibi tüm makroskopik büyüklükler Boltzmann denkleminin çözümü olan dağılım fonksiyonunun momentleri ile hesaplanabilir. Ancak Boltzmann denkleminde gaz moleküllerinin çarpışmasını modelleyen çarpışma terimi, bu denklemi bir doğrusal-olmayan integro-diferansiyel denklem yapar. Bu doğrusal-olmayan integro-diferansiyel denklemin genel çözümü mevcut değildir. Ayrıca, Boltzmann denkleminde bilinmeyen dağılım fonksiyonu bir, iki ve üç boyutta

sırasıyla, 3, 5, 7 değişkene bağlıdır. Bu durum sayısal çözümde de birçok zorluğu yanında getirmektedir.

Boltzmann denkleminde, büyük zorluklara neden olan çarpışma teriminin basitleştirilmesi önem taşımaktadır. Yeni basitleştirilmiş çarpışma terimi orijinal çarpışma terimine benzemeli ve temel fiziksel özellikleri içermelidir. Basitleştirilmiş çarpışma terimli Boltzmann denklemi, kinetik model veya model kinetik denklem olarak adlandırılır. İki önemli kinetik model olan BGK (Bhatnagar, Gross ve Krook) ve Shakhov kinetik modelleri bu çalışmada ele alınmıştır.

Tezin üçüncü bölümünde, doğrudan benzetim Monte Carlo (direct simulation Monte Carlo (DSMC)) yaklaşımı incelenmiştir. Boltzmann denklemi bu doğrudan benzetim Monte Carlo metodu ile sayısal çözüldü, ve sınır koşullarının bu benzetim metodunda uygulanması ayrıntılı bir biçimde anlatıldı. Tezde, silindirik bir geometri için DSMC yöntemi Fortran dilinde kullanıldı. Bu yöntemin kullanılışı, ele alınan probleme göre değişiklik gösterdiğinden, her bölümde ayrıca anlatıldı. Doğrudan Monte Carlo benzetim metodu, Boltzmann denklemini çözmek için moleküler stokastik bir yöntemdir. Bu metotta, her molekül çok sayıda molekülü temsil eder, böylece moleküler dinamik benzetim yaklaşımına göre çok avantajlıdır. DSMC yönteminin başka bir önemli özelliği de koşulsuz kararlı olmasıdır. DSMC yöntemi, Boltzmann denkleminin çarpışma terimini moleküler kaos varsayımına dayanarak rastgele sayılar kullanarak modeller. Bununla birlikte, DSMC moleküllerinin sayısı az olduğu durumda, istatistiksel (stokastik) gürültü ortaya çıkar.

Dördüncü bölümde, diğer bir Boltzmann denklemini sayısal çözme yöntemi olan ayrık hızlar metodu (discrete velocity method) tanıtıldı ve Fortran dilinde uygulandı. Boltzmann denkleminin karmaşık çarpışma terimi, Shakhov çarpışma terimi ile değiştirildi. Yeni oluşan model denklem, sıcaklık gradyenlerinin varlığı altında ayrık hızlar metodu ile çözüldü ve doğrudan Monte Carlo benzetim yöntemi ile karşılaştırıldı. Sonuçlar mikro-akışlarda gaz-yüzey arasındaki ısı iletiminin, eğrisel yüzeylerde doğrusal yüzeylere göre farklı olduğunu gösterdi. Ayrıca sonuçlar, zamandan bağımsız, küçük ısı değişimine sahip akışlarda Shakhov kinetik model çözümünün doğrudan Monte Carlo benzetim metoduna göre daha hızlı çözüme yaklaştığını göstermektedir.

Beşinci bölümde, Navier-Stokes denkleminin çıkartılışındaki varsayımlar incelendi; gerilme ve ısı transfer terimlerinin yüzey etkilerinden dolayı mikro-akışlarda geçersiz olabileceği sonucuna varıldı. Kaynaklarda daha önce önerilmiş kayma sınır koşulları listelenmiş ve eğrisel yüzeyler için yeni bir yüksek-mertebe sınır koşulu tanıtıldı.

Altıncı bölümde, salınım yapan eğrisel yüzeylerde gaz akışı doğrudan Monte Carlo benzetim metodu ve iki farklı ikinci-mertebe kayma sınır koşulu ile incelendi. Seyreltme ve salınım frekansı etkileri tartışıldı. Sonuçlar açıkça eğrilik etkilerinin erken geçiş rejiminde önemli bir rol oynadığını, ve eğrilik ile kayma modellerinin (kayma sınır koşullarına sahip Navier-Stokes denklemlerinin) doğruluğunun azaldığını ortaya koymaktadır. Ayrıca sonuçlar dışbükey yüzey üzerinde S sınır tabakasının varlığını göstermektedir.

Yedinci bölümde, aniden harekete başlayan eğrisel yüzey üzerinde zamana bağlı gaz hareketi, Heaviside operasyonel metot ile incelendi. Çalışmada önerilen kayma sınır koşulları karmaşık bir fonksiyonel yapıya sahip olduğundan, değişkenlere ayırma yöntemi veya Fourier ve Laplace integral dönüşüm yöntemlerinin kullanılması uygun değildir. Bu nedenle operasyonel bir yöntem kullanıldı. Bu yöntemde operatör ile (türev operatörü) sabit bir sayıymış gibi işlem yapılır ve böylece parça türevli

denklem adi türevli hale dönüştürülerek çözülür. Daha sonra da Heaviside açılım teoremi kullanılarak, ele alınan parça türevli denklemlerin aranan genel çözümleri bulundu. Yedinci bölümde, operasyonel yöntem ile ilgili temel teori verildi. Eğrisel yüzey üzerinde üç farklı akış problem, Heaviside operasyonel yöntem ile ayrıntılı incelendi. Knudsen ve S sınır tabakalarının oluşumu ve yüzey kaymaları hesaplandı.

Sekizinci bölümde, iki silindir arasına yerleştirilmiş ince kabuk üzerinde gaz davranışı incelendi. Yüzeyin içbükey veya dışbükey olmasının akış üzerindeki etkileri gösterildi. Knudsen sınır tabakasının oluşumunda gaz tarafından yüzeye uygulanan gerilmenin etkili olduğu sonucu elde edildi. Yüzey geometrisinin değişmesi ile yüzey gerilmesi değiştiğinden, yüzey geometrisinin Knudsen sınır tabakasının oluşmasında ve gaz davranışı üzerinde önemli etkileri olduğu gösterildi. Ayrıca S sınır tabaksının dışbükey yüzeylerde beklenenden çok daha fazla gaz davranışında etkili olduğu belirlendi.

Dokuzuncu bölümde, eğrisel yüzeylerde hız kayma miktarları incelendi. Yüzeyin içbükey ve dışbükey olmasının ile yüzey eğriliğinin kayma miktarı üzerindeki etkileri araştırıldı. Yüzey kaymalarının bulunması için yeni formüller önerildi ve sonuçlar doğrudan Monte Carlo benzetim metodunun sonuçları ile karşılaştırıldı. Böylece, önerilen formüllerin doğruluğu içbükey ve dışbükey yüzeyler için gösterildi. Ayrıca kayma formülleri kullanılarak ilginç bir mikro-akış davranışı olan hız yön değiştirmesi incelendi. Bu gaz davranışı silindiriksel Couette mikro-akışlarda, iç silindirin döndüğü ve dış silindirin sabit durduğu durumda, gazın teğetsel hızının dönen iç silindirden sabit duran dış silindire doğru artması ile ortaya çıkar. Bu beklenmedik davranış, Knudsen sayısı büyük ve konaklama katsayısı nispeten küçük olduğunda sadece görülür. Ayrıca bu bölümde yeni bir hız yön değiştirmesi kriteri teklif edildi. Sonuçlar sanılanın aksine hız yön değiştirmesinin sadece eğrilik etkilerinden kaynaklanmadığını göstermektedir: hız yön değiştirmesi, dış silindir konaklama sabitinin küçük olduğu ve iç silindir üzerindeki S sınır tabakasının yeterince kaymaya sebep olduğu durumda gerçekleşmektedir. Böylece hız yön değiştirmesinin, neden dış silindir dönerken ve iç silindir sabit durduğu durumda oluşmadığı da açıklandı.

1. INTRODUCTION

Richard Feynman in his famous talk entitled as “There’s plenty of room at the bottom” in 1959 envisaged a future with miniaturized machines. By the late 1980s small-scale devices began to be manufactured and the research of flows within micro-electro-mechanical systems (MEMS) emerged. Today, by the development of fabrication techniques, a nano-motor with size 10 nm has been built (Shen, 2005). Now on, as pointed out by Mohammed Gad-El-Hak (1999), it is very important to answer many questions associated with flow phenomena within micro-scale devices from the mathematical point of view.

The dynamics of gas microflows differ significantly from the dynamics of macroscopic flows and cannot always be predicted by the conventional fluid dynamic (the Navier-Stokes) equations with the no-slip boundary condition. The no-slip boundary condition assumes that the fluid will have zero velocity relative to the velocity of the boundary. The breakdown of the no-slip boundary condition at a fluid-solid interface and the importance of taking into account velocity slip have been recognized in micro/nanofluidics for many years (Vinogradova, 1999; Zhu and Granick, 2002; Majumder et al., 2005; Holt et al., 2006; Whitby and Quirke, 2007). However, relatively few studies have investigated the phenomenon of slip flow over nonplanar surfaces, and consequently, the relationship between the curvature of the surface and the degree of boundary slip has not been understood sufficiently well.

A theoretical understanding of boundary slip is clearly of great importance in the design of microfluidic devices. However, accounting for the complex interactions between the factors that affect the boundary slip (such as surface roughness, the wettability of the surface, the presence of nanobubbles/gaseous layers and the surface curvature) remains a formidable challenge, as reviewed by Neto et al. (2005) and Lauga et al. (2007).

In micro gas flows, the phenomenon of boundary slip is frequently encountered. As the length scales of microfluidic devices are decreased towards the micro/nano-scale,

the degree of slip can substantially alter the flow behaviour, highlighting the need for better descriptive models for quantifying the boundary slip. In addition, the presence of boundary slip can significantly influence the operating performance of a gas-phase micro-system and can also have profound effects on convective heat transfer (Colin, 2012). In reality, most microdevices contain nonplanar surfaces. Surprisingly, however, relatively little research has been conducted on slip effects over nonplanar walls. Understanding the slip behaviour and controlling the degree of slip in the presence of surface curvature is also essential for improving the reliability of gas-phase micro-systems.

In microflows, the surface-to-volume ratio is high and the gas-surface interactions become important. Moreover, the characteristic length scale is small and therefore rarefaction effects are important due to the high Knudsen number (Kn), which is the ratio of the molecular mean-free path to the characteristic length of the flow domain. Even under the atmospheric conditions, the Knudsen number may be large due to the small characteristic length. When the Knudsen number is less than 0.001, the flow can be described by the Navier-Stokes equations using conventional no-slip boundary conditions. When the Knudsen number is in the range between 0.001 and 0.1, which is referred as the slip-flow regime, the Navier-Stokes equations are still able to capture the essential flow characteristics but velocity-slip and temperature-jump boundary conditions must be employed. However, many micro-electro-mechanical systems (MEMS) operate in the early transition regime (i.e. $0.1<Kn<1$) and it is therefore important to be able to extend the validity of slip models to higher Knudsen numbers. In the early transition regime, the Newtonian stress and Fourier heat transfer relations start to break down and the Knudsen layer, which is the nonlinear region extending approximately one mean-free path from the surface, has a critical influence on the flow behaviour. When the Knudsen number increases beyond unity, alternative models such as the moment method or the Boltzmann equation must be used.

The present study starts with an introduction to the theoretical framework of the kinetic theory of gases and introduces the Boltzmann equation in Chapter 2. The Boltzmann equation is the central equation of the gas kinetic theory, which explains the gas behaviour from the atomic point of view. The Boltzmann equation is crucially important to predict the flow behaviour within the gas-phase microdevices,

since the Boltzmann equation is valid in all flow regimes at all Knudsen numbers. However, the general solution of the Boltzmann equation is not available due to the complicated collision term. Chapter 2 investigates the nonlinear collision term of the Boltzmann equation and boundary conditions for the Boltzmann equation in detail. Derivations of the Boltzmann and the moment equations have been studied. The moment equations which are macroscopic flow equations obtained from the Boltzmann equation have been explained. These macroscopic equations represent the conservation laws with five equations containing thirteen unknowns. To form a determined system of equations, the Chapman-Enskog expansion or the moment method must be used. The Chapman-Enskog method is used for finding the stress and heat flux terms as functions of density, velocity, temperature and their spatial derivatives. Alternatively, the moment method finds the stress and heat flux terms by calculating the higher-order moments. However, both methods share the problem of how to describe the boundary conditions for higher derivatives and higher moments.

The numerical solution of the Boltzmann equation is crucially important in modelling micro gas flows. Chapter 3 has been devoted to the direct simulation Monte Carlo method (DSMC) which is one of the most effective techniques for solving the Boltzmann equation (Bird, 1994; Oran et al., 1998). The DSMC method is a stochastic particle approach based on kinetic theory which can be shown to converge to the solution of the nonlinear Boltzmann equation in the limit of infinitesimal discretization if a sufficiently large number of particles are used in the simulation (Wagner, 2011). Each simulation particle in the DSMC method represents a large number of gas molecules and therefore a relatively small number of particles are needed in the simulation. This is an important advantage of DSMC method compared to molecular dynamics approaches. Another important feature of the DSMC method is that it is unconditionally stable. However, when the number of particles is small, the statistical noise increases considerably due to the fact that the collision term of the Boltzmann equation is simulated using random numbers based on the molecular chaos assumption of the collision process. The macroscopic properties of the gas (i.e. the physically observable quantities such as pressure and temperature) are postulated to be the averaged values of the microscopic random motion, and therefore the macroscopic quantities are calculated by averaging the

microscopic values. The theoretical foundations and implementation details of the DSMC method have been presented in Chapter 3.

DSMC simulations are implemented initially in Matlab for the planar Couette flow case in Chapter 3. However, simulations are implemented in Fortran for the rest of the study in the case of nonplanar flows. The present study adopts the standard DSMC algorithm proposed by Bird (1994) with the exception of a small modification in the calculation of the maximum collision number in a cell, as described by Stefanov et al. (1998). Weighting factors for improving the particle number balance in the radial direction were not included in the present algorithm since the simulations did not consider large ratios of cylinder radii. The simulations considered a hard-sphere model for argon and implemented isothermal fully diffusive reflections at the surfaces. The one-dimensional flow domain was discretized using 200 cells in the radial direction with each cell containing from 100 to 1000 simulation particles depending on the flow problem. Approximately 100 ensemble averages are calculated in order to obtain mean-time flow profiles for the time dependent flow problems.

In Chapter 3, the results of several flow cases which are of great importance in order to understand gas flows within micro/nano-systems have also been demonstrated. Since, in microflows, the momentum and heat transfer between gas and wall are closely related to gas-wall interactions, implementation of different gas-wall interactions models (i.e. scattering kernels) into the DSMC simulation has been studied. Finally, velocity profiles of three different Couette flows namely, (a) flow between two parallel plates, (b) flow between two rotating cylinders, and (c) flow within a rotating cylinder have been examined.

An alternative numerical approach to solve the Boltzmann is the discrete velocity method. The discrete velocity method can be considered as the finite difference solution of the Boltzmann equation; therefore the solution does not contain any noise, unlike the DSMC results. The discrete velocity method for steady (i.e. time-independent) flows associated with small velocity and/or temperature variation can outperform the DSMC approach in terms of computational time. Since many micro-electro-mechanical systems (MEMS) operate in non-isothermal conditions, Chapter 4 takes into account thermal effects and investigates the solution of the Boltzmann equation using discrete velocity method. The chapter replaces the problematic

collision with the Shakhov collision term and then examines the numerical solution of the nonlinear Shakhov model kinetic equation subject to the Maxwell boundary condition using the discrete velocity method.

In Chapter 4, the discrete velocity method is implemented in a cylindrical domain using Fortran. The angular period and the annular clearance between concentric cylinders are both divided into 100 equal intervals. For the velocity space, the magnitudes of the molecular velocity are mapped onto 20 Gauss quadrature points with their associated weights. Integrals for calculating the macroscopic quantities are obtained using the Gauss quadrature rule at each iteration. When the difference between macroscopic temperatures of successive iterations is smaller than a certain tolerance value, the convergence criterion is assumed to be fulfilled.

In Chapter 5, the assumptions made in the derivation of the Navier-Stokes equations have been investigated in detail to understand the limiting conditions of these equations. In classical fluid mechanics, the stress tensor and heat flux are assumed to be linearly proportional to the temperature gradient and the rate of strain, respectively. However, these assumptions are invalid when representing the gas-surface interactions in gas microflows. The continuum assumption, which is another assumption made in the derivation of the Navier-Stokes equations, is also invalid when the Knudsen number increases beyond 10. In the slip-flow regime (i.e. $0.001<Kn<0.1$), the momentum and heat transfer properties of microflows differ from that of macroflows; the gas effectively slides over the surface and a temperature-jump exists between the surface and the gas. For the slip-flow regime, the Navier-Stokes equations can still capture the flow characteristics by means of the velocity-slip and temperature-jump boundary conditions. In Chapter 5, the slip boundary conditions proposed in the literature have been reviewed. Slip boundary conditions that are higher-order in Knudsen number are important to extend the validity of slip models (the Navier-Stokes equations with slip boundary conditions) into the early transition regime (i.e. $0.1<Kn<1$). Second-order velocity-slip boundary conditions for the early transition regime have been investigated. Although several second-order velocity-slip boundary conditions have been proposed in the literature, most of them can only be applied to planar surfaces. Nevertheless slip boundary conditions proposed by Maxwell (1879) and Myong (2004) are applicable to microflows over nonplanar (i.e. curved) surfaces, they are first-order in Knudsen

number and show considerable discrepancies against the DSMC data in the early transition regime. A second-order velocity-slip boundary condition has recently been developed by Taheri and Struchtrup (2009) using the regularized 13-moment (R13) equations. Their boundary condition is applicable to cylindrical geometry. Therefore, a generic second-order velocity-slip boundary condition applicable to a wider range of flow geometries has been developed.

Micro-electro-mechanical systems (MEMS) with oscillatory structures are commonly used in a number of applications such as resonating sensors, actuators, accelerometers and gyroscopes. In Chapter 6, two fundamental rarefied oscillatory flows, a confined Couette flow between two concentric oscillating cylinders and an unconfined flow around an oscillating cylinder (i.e. the cylindrical form of Stokes' second problem), have been investigated. The effects of rarefaction, oscillation frequency and surface curvature on the flow characteristics have been examined. For these nonplanar flow cases, the second-order velocity-slip boundary condition proposed by Taheri and Struchtrup (2009) for cylindrical geometry and a generic nonplanar second-order boundary condition are employed. The flow profiles have been found for the fully diffusive case (i.e. a tangential momentum accommodation coefficient of unity). The results have been compared against DSMC data. At a Knudsen number of 0.1, the analytical solutions are found to be in very good agreement with the DSMC data presented by Emerson et al. (2007).

The effects of curvature have been investigated for the cylindrical form of Stokes' second problem. The curvature is defined as the inverse of the oscillating cylinder radius. The velocity profiles at different values of curvature show that changes in the velocity profile due to curvature effects are more prominent at high Knudsen numbers. The penetration depth is defined as the distance from the oscillating surface to the location where the amplitude of the velocity oscillation decays to 1% of the surface velocity. The velocity profiles show that the penetration depth decreases as the Knudsen number and curvature increase.

For the planar oscillatory Couette flow case, Hadjiconstantinou (2005) has reported that the second-order slip solution is in very good agreement with DSMC data up to $Kn \approx 0.4$. On the other hand, for the nonplanar case, Emerson et al. (2007) have shown that the first-order slip solution shows large discrepancies with the DSMC data at $Kn=0.5$. The results indicate that second-order boundary conditions are

unable to improve the accuracy of the solution for nonplanar flows, and show that there are still significant discrepancies between the second-order slip solution and the DSMC data. This demonstrates the important effect of surface curvature. Moreover, the effects of curvature have been investigated for different values of the Stokes number. The analysis shows that the amount of slip over an oscillating inner cylinder is larger than the slip over an oscillating outer cylinder. This has been explained by the smaller surface area of the inner cylinder.

The effects of curvature have also been investigated for cylindrical Couette flow. The amount of slip over the oscillating inner cylinder increases as the curvature increases. Conversely, in the case of an oscillatory outer cylinder, the amount of slip over the oscillating cylinder decreases as the curvature increases. This opposing effect can be explained by the different surface shapes (i.e. convex/concave) on the inner and outer cylinders.

The accuracy of two recent second-order slip boundary conditions has been investigated by calculating the mass flow rate discrepancies for two fundamental oscillatory flows: a confined Couette flow between two concentric oscillating cylinders and the cylindrical form of Stokes' second problem. The discrepancies between the mass flow rates of the analytical slip solutions and the DSMC data have been evaluated at a Knudsen number of 0.5 for different values of curvature and Stokes number. The results indicate that slip models with an oscillating inner cylinder show larger discrepancies against the DSMC data in comparison to the case of an oscillatory outer cylinder. In the early transition regime, the growing influence of the Knudsen layer is expected to reduce the predictive capability of slip models. However, this does not explain why slip models are performing poorly for the nonplanar oscillatory flow case in comparison to the planar case; nor does it explain why slip models show larger discrepancies against the DSMC solution on the convex surface. These effects may be explained by the existence of the S-layer over the inner cylinder as first described by Sone (1973). The S-layer can only exist over a convex surface and its thickness is proportional to the curvature of the surface.

Many microfluidic devices contain curved boundaries. Recent studies (Emerson et al., 2007; Dinler et al., 2010a; Dinler et al., 2010b) have shown that the effects of curvature and the surface shape can play an important role in the flow behaviour. In Chapter 7, we have focused on three fundamental time-dependent nonplanar

microflows, namely, (a) flow inside an impulsively-started rotating cylinder, (b) flow between impulsively-started rotating concentric cylinders, and (c) flow over an impulsively-started rotating cylinder (i.e. the cylindrical form of Stokes' first problem) have been investigated in the early transition regime (i.e. $0.1<Kn<1$). The first- and second-order velocity-slip boundary conditions have been employed and Stokes-type (linear) partial differential equations have been solved using the Heaviside's operational method in order to understand the unsteady motion of the micro gas flows subject to the slip boundary conditions. Important to note that separation of variables technique cannot be applied straightforwardly here due to the complex form of the boundary condition of our interest; and nor can the Laplace and Fourier transform methods be used easily. Integral transform methods require transformation of the boundary condition into the integral domain where equations could be treated, and the transform method eventually gives an expression requiring an inverse transformation which would be very problematic.

The velocity profiles have been examined in order to highlight the effects of curvature and the surface shape. The results support the existence of the S-layer over a convex surface. In addition, the magnitudes of the vorticity and shear stress on the surface of the cylinders have been examined.

- The results show that the steady-state vorticities of all three flow cases are independent of the radial distance. Moreover, in flow cases (a) and (c), the magnitudes of the steady-state vorticities are independent of the Knudsen number. On the other hand, in flow case (b), the magnitude of the vorticity decreases when the Knudsen number increases.
- The research shows that the magnitudes of the steady-state shear stress exerted onto the surfaces in flow cases (b) and (c) decrease with the Knudsen number. However, in flow case (a), the magnitude of the shear stress is zero. As a result, the steady-state motion of the gas is equivalent to a solid body rotation in flow case (a).
- In flow cases (b) and (c), as the Knudsen number increases, the gas slides more effectively over the cylinder surfaces. However, in flow case (a), the Knudsen number is only influential in the time taken to reach steady-state, and the slip model predicts zero slip-velocity at steady-state for all Knudsen

numbers. This is interpreted as a result of the concave shape of the rotating cylinder surface.

- Curvature is defined as the inverse of the rotating cylinder radius. In flow case (b), the slip-velocity on the rotating inner cylinder increases with curvature. Conversely, the slip-velocity on the rotating outer cylinder decreases with curvature. This shows that there is an opposing effect of curvature on the slip at the inner and outer cylinder surfaces. Interestingly, this contrary curvature effect may explain why velocity inversion occurs in a flow between rotating concentric cylinders while it does not occur in the equivalent flow case between two parallel plates.

In Chapter 8, a gas microflow driven by a thin rotating cylindrical shell, which is positioned in the middle of the gap between two concentric cylinders, has been investigated. The flow geometry of this shell problem allows us to highlight the profound role of the surface shape in the flow behaviour by eliminating the effects of curvature and surface area. The research demonstrates anomalous velocity and temperature profiles that appear due to the curved shape of a micro-surface. The results also show the velocity defect over the convex side of the shell is larger compared to that over the concave side. Moreover, the velocity defect over the concave surface decreases with curvature but in contrast, the velocity defect over the convex surface increases with curvature. In addition, the velocity defect in the equivalent planar flow case defines a lower and an upper limit for the velocity defect over convex and concave surfaces, respectively. Furthermore, the results show a more clear relationship between the shear stress and the velocity defect. In the case of a concave surface, the relationship between the stress and velocity defect is linear; on the other hand, it is slightly non-linear over a convex surface. In the case of a concave surface, a linear function of shear stress has been fitted to the velocity defect with a slope of 0.472. In this fit, the root mean square error (RMSE) is 0.00025 and the coefficient of determination is 99.72%. On the other hand, in the case of a convex surface, a non-linear relation has been proposed with an additional term including the squared value of the shear stress where the coefficient of determination is 99.18%.

Since relatively few studies have investigated the phenomenon of slip flow over nonplanar surfaces, the relationship between the curvature of the surface and the

degree of boundary slip has not been understood sufficiently well. In Chapter 9, we have delved further into the fluid behaviour over nonplanar surfaces. A direct simulation Monte Carlo (DSMC) approach and a second-order velocity-slip Navier-Stokes continuum description have been used to address important issues related to the degree of boundary slip for gas-phase flow over curved surfaces. The study considers cylindrical Couette flow between two concentric cylinders and examines the curvature effects over the convex and concave surfaces. The results reveal that the degree of slip depends effectively on the surface shape (i.e. convex/concave), with the surface curvature having an opposing effect on the boundary slip over rotating concave and convex surfaces. The results also show that as surface curvature increases, the boundary slip becomes negligible over a concave surface while it becomes increasingly important over a convex surface. In addition, novel boundary slip formulae are proposed that can accurately predict the tangential velocities (and boundary slips) over convex and concave surfaces. These formulae are found to be in very good agreement with DSMC data for a range of accommodation coefficients and boundary curvatures. Using the corrected slip velocities at the inner and outer cylinders, the present study then reassesses the mechanism of the intriguing phenomenon of velocity inversion which has, until the present study, often been mistakenly attributed solely to the effects of boundary curvature.

The comparison of the DSMC and the Navier-Stokes slip solution indicate that the accuracy of the slip boundary condition deteriorates over convex surfaces and should be used with caution due to the existence of the S-layer. A series of boundary slip correction formulae, which suggest a direct relationship between the boundary slip and the shear stress exerted on the wall, have been proposed in order to predict the degree of boundary slip accurately. These formulae have been found to be in excellent agreement with the DSMC data up to Kn=0.5. The effects of curvature and the surface shape, and the intriguing phenomenon of velocity inversion have then been investigated using these boundary slip corrections.

The results in Chapter 9 reveal that the degree of slip depends essentially on the surface shape, with the surface curvature having an opposing effect on the boundary slip over rotating concave and convex surfaces. The results show that as the surface curvature increases, the boundary slip becomes negligible over a concave surface

while it becomes increasingly influential for the flow over a convex surface. This dramatic effect of the surface shape on boundary slip, namely, the opposing effect of curvature, has been investigated in detail. It is shown that for rarefied Couette flow between two concentric cylinders, the opposing effect can sometimes break down over a stationary cylinder or over a rotating cylinder with a low accommodation coefficient.

The Chapter 9 also investigates the intriguing and highly non-intuitive phenomenon of velocity inversion which can occur when the inner cylinder is rotating and the outer cylinder is stationary. Under certain conditions, namely when the Knudsen number is relatively high and the accommodation coefficient of the outer cylinder is relatively low, it is possible to obtain an inverted velocity profile where the velocity increases from the rotating inner cylinder to the stationary outer cylinder. This unusual phenomenon has often been attributed to the effects of curvature since it does not occur in the equivalent planar case of Couette flow between two parallel plates. However, the present study demonstrates that the phenomenon of velocity inversion cannot be explained solely by the effects of curvature. Instead, the results show that velocity inversion occurs due to an acceleration of the gas molecules at the outer cylinder associated with the breakdown of the opposing effect. The study also shows that the presence of the hydrodynamic S-layer at the convex surface plays an important role in the velocity inversion mechanism.

2. BOLTZMANN EQUATION IN BOUNDED DOMAINS

2.1 Introduction to the Kinetic Theory

The kinetic theory of gases explains the gas behaviour from the atomic point of view. Theory initially assumes that the gas consists of a large number of molecules (a molecule can be a single atom as well as can be made of several atoms) which are constantly moving and colliding with each other. The gas molecules are considered as identical hard spheres (like billiard balls) with a radius of about 10^{-10} m (0.1 nanometre). The molecules elastically collide with each other or bounce off the boundary where the conservation of momentum and energy are perfectly conserved. The average distance between molecules is much greater than molecule diameter. The subtle and possibly the most important notion in the gas theory is the intrinsic uncertainty of the location and velocity of a gas molecule. The macroscopic properties (i.e. physically observable quantities) of the gas such as pressure and temperature are postulated to be the average values of the microscopic random motion of gas molecules.

From the microscopic point of view, molecules are constantly bombarding the wall of the container, and as a result the impact of molecules exerts a force on the wall. Let a container has a volume V containing N molecules. If a velocity of a striking molecule has a velocity vector $\boldsymbol{c}$ with a normal component c_x towards the wall, then the molecule will bounce back with a momentum of $m(-c_x)$ and therefore the momentum change of a single molecule can be written as

$$mc_x - m(-c_x) = 2mc_x \qquad \textbf{(2.1)}$$

where m is the molecular mass. During a time interval Δt, half of the all molecules at a distance $c_x \Delta t$ from the wall will strike the wall, and the other half will be moving away from the wall since they have bounced back. The number of molecules that will strike the wall sweeps the volume $c_x \Delta t A$ where A is the area of the wall.

Hence, the ratio of number of striking molecules to the total number of molecules can be written

$$\frac{\text{Number of molecules that strike the wall}}{\text{Total number of molecules in the container}} = \frac{c_x \Delta t A}{V}. \quad \textbf{(2.2)}$$

Consequently, the total momentum imparted to the wall is

$$2mc_x \frac{c_x \Delta t A}{V} \frac{N}{2} = \frac{Nmc_x^2 A}{V} \Delta t \,. \quad \textbf{(2.3)}$$

The force F on the wall is the rate of momentum change, and then it can be written as

$$F = \frac{Nmc_x^2 A}{V}. \quad \textbf{(2.4)}$$

The pressure P is then can be obtained as force per unit area

$$P = \frac{Nmc_x^2}{V} \text{ in other words } PV = Nmc_x^2 \quad \textbf{(2.5)}$$

In reality, each molecule has different c_x which is randomly distributed according to a certain distribution function. Moreover, pressure is, in fact, related to the average velocity in all (three) directions, $1/3\left|\langle \mathbf{c} \rangle\right|^2$; where $\langle \mathbf{c} \rangle$ is the average velocity over all possible velocities. Hence,

$$PV = \frac{1}{3} Nm \left|\langle \mathbf{c} \rangle\right|^2 \quad \textbf{(2.6)}$$

The average total energy, E, which is only composed of kinetic energy, is

$$E = N \frac{1}{2} m \left|\langle \mathbf{c} \rangle\right|^2. \quad \textbf{(2.7)}$$

Therefore, a formula relating the pressure, volume and energy is obtained as

$$PV = \frac{2}{3} E \,. \quad \textbf{(2.8)}$$

Using ideal gas law, $PV = N/N_A RT$, where N_A is the Avogadro number and R is the ideal gas constant,

$$PV = \frac{2}{3}E = \frac{1}{3}Nm\left|\langle \mathbf{c} \rangle\right|^2 = \frac{N}{N_A}RT \tag{2.9}$$

Therefore an important relation can be obtained as

$$\frac{3}{2}k_B T = \frac{1}{2}m\left|\langle \mathbf{c} \rangle\right|^2 \tag{2.10}$$

where $k_B = R/N_A$ is the Boltzmann constant. Equation (2.10) gives the relation between temperature and the kinetic energy of a single molecule (Baaquie and Willeboordse, 2009). This relation also implies that kinetic energy does not depend on the type of gas (each which has different molecular mass) at the same pressure. Importantly, this relation also relates the (average) velocity of molecules to the macroscopic temperature.

The mean free path is particularly important property when analysing gas-wall interactions. The mean free path, λ, is the average distance that a molecule travels between two successive collisions. The mean free path can be estimated as the ratio of the distance travelled in a time interval Δt by a molecule to the number of molecules encountered in this travel. A molecule travels a distance in one direction on average $\langle c \rangle \Delta t$. Let the number of molecules per unit volume (i.e. number density) is *n*. Since a collision occurs when the distance between two molecules are two radii ($2r$), collisions sweep a cylindrical volume $\sigma_{cs}\langle c \rangle \Delta t$, with a cross section $\sigma_{cs} = \pi(2r)^2$. Therefore the mean free path of a molecule can be expressed as

$$\lambda = \frac{\langle c \rangle \Delta t}{n\sigma_{cs}\langle c \rangle \Delta t} \tag{2.11}$$

Considering all particles moving, the mean free path can be estimated in an equilibrium gas as dividing Eq. (2.11) by an additional factor $\sqrt{2}$ (Chapman and Cowling, 1970)

$$\lambda = \frac{1}{\sqrt{2}\, n\sigma_{cs}} \tag{2.12}$$

The number of collisions per second can be given by $\lambda/\langle c \rangle$, yielding about 10^9 collisions per second. In Eq. (2.12), the mean free path is inversely proportional to the number density and the molecular radius. This implies that as the molecular weight increases or density increase, the mean free path decreases.

The Chapman-Enskog theory relates the coefficient of viscosity to the cross section at temperature *T* as (Chapman and Cowling, 1970)

$$\mu = 5m/16\ (2\pi RT)^{1/2}/\sigma_{cs} \qquad \textbf{(2.13)}$$

where *m* is the molecular mass and *R* is the gas constant. The cross section is eliminated from Eq. (2.12) using Eq. (2.13), thus the mean free path for the *hard sphere collision model* is written as

$$\lambda_{HS} = 16\mu/5\ (2\pi RT)^{-1/2}/\rho \qquad \textbf{(2.14)}$$

where $\rho = nm$ is the density. In case the factor $16/5 = 3.2$ is replaced by π, the mean free path for hard spheres corresponds to the mean free path definition provided by Maxwell (Maxwell, 1879).

The hard sphere mean free path definition (2.14) is associated with the viscosity and accordingly with the heat conductivity as (function of the temperature), $\mu(T) = \mu(T_{ref})\sqrt{T/T_{ref}}$ and $k(T) = k(T_{ref})\sqrt{T/T_{ref}}$, respectively, where T_{ref} is the reference temperature. In fact, an inverse power law (the intermolecular potential with only repulsive part) can be introduced into the collision model in order to employ a more realistic molecular collision model. When an intermolecular potential is taken into account, the *variable hard sphere collision (VHS) model* yields, $\mu(T) = \mu(T_{ref})(T/T_{ref})^{\omega}$ and $k(T) = k(T_{ref})(T/T_{ref})^{\omega}$. The VHS model alters the cross section σ_{cs} and therefore the mean free path definition changes to

$$\lambda_{VHS} = (2\mu/15)(7-2\omega)(5-2\omega)(2\pi RT)^{-1/2}/\rho \qquad \textbf{(2.15)}$$

The expression (2.15) for $\omega = 0.5$ gives the mean free path for the hard sphere molecules and for $\omega = 1$ gives the mean free path for the Maxwell molecules.

2.2 The Boltzmann Equation

The Boltzmann equation (BE), which is the central equation in the kinetic theory of gases, models the change of a single molecule distribution function. Remarkably, it is valid in all gas flow regimes, at all Knudsen numbers. The relation between the microscopic and macroscopic descriptions is postulated as: all macroscopic quantities such as density, velocity and temperature can be described in terms of the microscopic states, which are the solution of the BE (Harris, 2004). The state of the gas is given in terms of a distribution function $f(\mathbf{x},\mathbf{v},t)$, where $\mathbf{x}\in\mathbb{R}^3$ is the position vector and $\mathbf{v}\in\mathbb{R}^3$ is the velocity vector of a molecule at time t. If the distribution function is known, all the moments, for example mass density, energy density, pressure and heat flux can be computed; but this is never the case because the general solution of the BE is not available.

The collision term in the BE causes tremendous difficulties. Therefore simplifying the problematic collision term is of great importance. The new simplified collision term must share main properties of the original collision term and satisfy the conservation laws, the entropy condition, and it must vanish in thermodynamic equilibrium (Cercignani, 2000). The BE with the simplified collision term is called the kinetic model or the model equation. Two important kinetic models are BGK (Bhatnagar, Gross and Krook) and Shakhov models.

The unknown distribution function in the BE depends on 3, 5, 7 variables in one-, two- and three-dimensions, respectively. Moreover the collision term makes the BE a nonlinear integro-differential equation. But by multiplying the BE with the mass m, the momentum mv and the molecular kinetic energy $1/2m|v|^2$, $v\in\mathbb{R}^3$ using collision invariant property of the collision operator and integrating from $-\infty$ to ∞, five equations of the conservation laws of the macroscopic flow can be obtained without solving the original BE. These five equations represent the conservation laws containing thirteen unknowns. Therefore either stress and heat flux terms must be found in terms of density, velocity, temperature and their space derivatives, or additional equations for stress and heat flux must be found using higher-order moments in order to end up with a closed system. These two approaches are called the Chapman-Enskog method and the moment method, respectively, and will be described briefly in Section 2.3.

In the free molecular flow regime, the influence of collisions is negligible; and in absence of external force, the BE reduces to the three-dimensional first-order wave equation and can be solved by the method of characteristics.

2.2.1 Derivation of the Boltzmann equation

Ludwig Boltzmann formulated the Boltzmann equation in 1872 considering the dilute gas and monatomic gas molecules moving and colliding with each other constantly and randomly. For a system of N molecules, the phase space, where all possible states occur, is $6N$ dimensional due to the three position (physical space) and three velocity (velocity space) components for each molecule. (Liou and Fang, 2005).

The Boltzmann equation states that

$$\begin{bmatrix}\text{Rate of change of the number of}\\ \text{molecules within the phase}\\ \text{space element } dV\end{bmatrix} = \begin{bmatrix}\text{Molecule flow rate}\\ \text{in through the surface}\end{bmatrix} + \begin{bmatrix}\text{Molecule flow rate}\\ \text{in through the surface}\\ \text{due to the external force}\end{bmatrix} + \begin{bmatrix}\text{Molecule flow rate}\\ \text{in through the surface due}\\ \text{to the molecular collisions}\end{bmatrix}$$

The probability density function of the velocity for a single molecule within phase space element dV is $F(\mathbf{v})$ and

$$\int_{dV} F d\mathbf{v} = 1 \qquad \textbf{(2.16)}$$

The rate of change of the number of molecules at an instant time is

$$\frac{\partial}{\partial t}\int_{dV} nF d\mathbf{x} d\mathbf{v} \qquad \textbf{(2.17)}$$

where $n(\mathbf{x},t)$ is the number density and nF is the number of molecules.

The molecule flow rate into the phase space is

$$-\int_{dS} (nF\mathbf{v})\cdot\mathbf{n} dS d\mathbf{v} \qquad \textbf{(2.18)}$$

The molecule flow rate into the phase space caused by an external force $\mathbf{X}$ per unit mass is

$$-\int_{dS} (nF\mathbf{X}dt)\cdot\mathbf{n}dSd\mathbf{v} \tag{2.19}$$

The external force is any force acting on particles such as the gravitational body force.

Using divergence theorem

$$\begin{aligned}&\int_{dV}\frac{\partial}{\partial t}nFd\mathbf{x}d\mathbf{v}+\int_{dV}\nabla\cdot(nF\mathbf{v})d\mathbf{x}d\mathbf{v}+\int_{dV}\nabla\cdot(nF\mathbf{X}dt)d\mathbf{x}d\mathbf{v}\\&=\int_{dV}\Delta_c(nF)d\mathbf{x}d\mathbf{v}\end{aligned} \tag{2.20}$$

where $\Delta_c(nF)$ is the rate of change of the number of molecules due to the intermolecular collisions. Then defining the distribution function as $f(\mathbf{x},\mathbf{v},t)=n(\mathbf{x},t)F(\mathbf{v})$ and using the relation $\nabla\cdot(h\mathbf{v})=\mathbf{v}\cdot\nabla h+h\nabla\cdot\mathbf{v}$ we obtain

$$\int_{dV}\left[\frac{\partial f}{\partial t}+\ \mathbf{v}\cdot\nabla f+f\nabla\cdot\mathbf{v}\ +\ \mathbf{X}\cdot\nabla fdt+f\nabla\cdot\mathbf{X}dt\ \right]d\mathbf{x}d\mathbf{v}=\int_{dV}\Delta_c f\,d\mathbf{x}d\mathbf{v} \tag{2.21}$$

Velocity of the molecules and the external force within the phase element do not change, and then Eq. (2.21) can be written as

$$\frac{\partial f}{\partial t}+\sum_{i=1}^{3}\left(\mathbf{v}\cdot\frac{\partial f}{\partial x_i}+\mathbf{X}\cdot\frac{\partial f}{\partial v_i}\right)=Q(f_1,f_2) \tag{2.22}$$

where the collision term, $Q(f_1,f_2)$, maps the pre-collision distribution functions of colliding molecules, f_1 and f_2, to the post-collision distribution functions f_1' and f_2' (i.e. $(f_1,f_2)\rightarrow(f_1',f_2')$). Equation (2.22) is the Boltzmann equation and models the change of a single molecule distribution function. The distribution function depends on three, five, seven variables in one-, two- and three-dimension, respectively.

In the molecular free flow regime, the intermolecular collisions are negligible and by neglecting the external force, the BE can be reduced to the three-dimensional first-order wave equation without problematic collision term as

$$\frac{\partial f}{\partial t}+\mathbf{v}\cdot\frac{\partial f}{\partial\mathbf{x}}=0 \tag{2.23}$$

The Cauchy problem with the initial condition $f(\mathbf{x},\mathbf{v},t=0)=f_0(\mathbf{x},\mathbf{v})$ in Eq. (2.23) is a quasi-linear first-order partial differential equation and can be solved by method of characteristics (McOwen, 1996). The general solution can be obtained easily as

$$f(\mathbf{x},\mathbf{v},t)=f_0(\mathbf{x}-\mathbf{v}t,\mathbf{v}) \tag{2.24}$$

where f_0 is the initial condition, $\mathbf{x}$ is the position vector and $\mathbf{v}$ is the velocity vector of a molecule at time *t*.

2.2.2 Nonlinear collision operator of the Boltzmann equation

The collision operator of the Boltzmann equation models the variation of velocities of particles through collisions. The gas is assumed to be dilute enough that only two particles collide with each other at a given time and position, in other words only binary collisions take place. Without loss of generality, chemical and electrostatic effects can be assumed to be negligible.

Since the Boltzmann equation describes the statistical behaviour of the gas molecules, the collision operator contains an inherent uncertainty. Boltzmann in 1872 modelled the quadratic collision operator in polar coordinates (r,φ) as

$$\int_{\mathbb{R}^3} dv_2 \int_0^{\infty} r dr \int_0^{2\pi} d\varphi \left|v_1-v_2\right|^{\omega} \quad f(t,x,v_1')\,f(t,x,v_2') - f(t,x,v_1)\,f(t,x,v_2) \tag{2.25}$$

which portrays a collision mapping from v_1,v_2,r,φ to v_1',v_2' at $t\geq 0$ and at a position $x\in\mathbb{R}^3$; where $v_1,v_2\in\mathbb{R}^3$ are the pre-collision velocities, $v_1',v_2'\in\mathbb{R}^3$ are the post-collision velocities of particles and $0\leq\omega\leq 1$ is the exponent of interaction potential.

The collision procedure is supposed to conserve momentum and energy (i.e. elastic collisions). Conservation of momentum reads as

$$v_1'+v_2'=v_1+v_2, \qquad \mathrm{v}_1,v_2,v_1',v_2'\in\mathbb{R}^3 \tag{2.26}$$

and conservation of energy gives

$$\left|v_1'\right|^2+\left|v_2'\right|^2=\left|v_1\right|^2+\left|v_2\right|^2, \qquad \mathrm{v}_1,v_2,v_1',v_2'\in\mathbb{R}^3 \tag{2.27}$$

which construct four equations instead of six. Even if we know the scattering angle $\theta\in[0,\pi]$ between pre- and post-collision velocities, conservation laws (2.26, 2.27)

above give a relation between pre- and post-collision velocities in terms of a deflection vector ϖ such that

$$v_1' = \frac{v_1 + v_2}{2} + \frac{|v_1 - v_2|}{2}\varpi$$
$$v_2' = \frac{v_1 + v_2}{2} - \frac{|v_1 - v_2|}{2}\varpi \qquad \textbf{(2.28)}$$

where $\varpi \in S^2$ varies in unit sphere in $\mathbb{R}^3$ depending on the relative velocity $v_1 - v_2$ and the scattering angle θ. By introducing a collision kernel (or an interaction potential), the collision procedure can be modelled deterministically. Then, by switching to integration over the surface of the unit sphere, the nonlinear collision integral can be written in terms of the collision kernel, $B(v_1 - v_2, \varpi)$, as

$$\int_{\mathbb{R}^3} dv_2 \int_{S^2} d\varpi B(v_1 - v_2, \varpi) \; f(t,x,v_1') f(t,x,v_2') - f(t,x,v_1) f(t,x,v_2) \qquad \textbf{(2.29)}$$

with $B(v_1 - v_2, \varpi) = B(|v_1 - v_2|, \cos\theta)$ and $\theta = \arccos \frac{(v_1 - v_2, \varpi)}{|v_1 - v_2|}$, where $(\cdot,\cdot)$ is the scalar product in $\mathbb{R}^3$.

The collision kernel can be computed through measuring the collision cross section experimentally for specific gases at certain conditions. In modelling, the collision kernel is modelled via an interaction potential model (inverse power law of repulsion model) in the form of

$$1/r^{\eta}, \qquad \eta > 1 \qquad \textbf{(2.30)}$$

where *r* is the distance between the two molecule centres as mentioned in Section 2.1. The collision kernel is described, in general, as

$$B(v_1 - v_2, \varpi) = C_{\varpi} |v_1 - v_2|^{2(1-\omega)} \qquad \textbf{(2.31)}$$

where C_{ϖ} is a function of θ (and accordingly function of ϖ) and ω can be expressed in terms of the power law exponent, η. The collision kernel in Equation (2.31) is called variable hard sphere collision kernel. In case of $\omega = 0.5$, Equation (2.31) gives the collision kernel for hard sphere gas model; and in case of $\omega = 1$, it gives the collision kernel for Maxwellian gas model.

The tensor products, $f(t,x,v_1')f(t,x,v_2') = f(t,x,v_1') \otimes f(t,x,v_2')$ and $f(t,x,v_1)f(t,x,v_2) = f(t,x,v_1) \otimes f(t,x,v_2)$ in the collision operator (2.29) makes the Boltzmann equation nonlinear integro-differential equation. In fact, multiplication of distribution functions shows intrinsically that distributions are uncorrelated.

Since the collision process is modelled deterministically by the conservation laws in Equations (2.28) and an interaction potential in Equation (2.31), the collision process implies time reversibility. When the pre-collision velocities are known, post-collision velocities can be found, and vice versa. This reversibility is local, which means that it is only reversible in very small time of the collision process at a given local time and position; and this is referred as micro-reversibility property of the Boltzmann operator. On the other hand, the velocities of particles which are about to collide are uncorrelated. This brings an uncertainty and we do not know exactly which particles are going to collide before collision. This is called chaos assumption of the Boltzmann equation. But when they collide, post-collision velocities are determined through the collision process. Thus, this is sometimes called one-sided chaos (Villani, 2002).

2.3 Gas-Wall Interactions and Scattering Kernels for the Boltzmann Equation

We consider in this thesis the Boltzmann equation in bounded domains due to its crucial importance in micro technologies. In micro gas flows, surface-to-volume ratio is high and therefore gas-wall interactions gain extra importance when modelling flow behaviour. The momentum and heat transfer between gas and wall are closely related to the gas-wall interaction model. In this chapter, scattering kernels for the Boltzmann equation, which models gas-wall interactions, are examined. Their implementation in the solution of the Boltzmann equation will be described in Chapter 4 through discrete velocity method technique; and their implementation in the direct simulation Monte Carlo method will be discussed in detail in Chapter 3.

The Boltzmann equation requires boundary conditions, which describe the reflection probability of molecules from a solid boundary. Then the question is how to relate the distribution of impinging (incoming) molecules to the reflected molecules. It is not surprising that the answer is a scattering kernel function, *R*. The scattering kernel is a probability function for a single molecule with a velocity *v* at the point **x** and time *t* in order to be reflected with a velocity v' at the same point after a time interval τ . When the distribution of impinging molecules, $f(\mathbf{x},\mathbf{v},t)$, is known, the distribution of reflected molecules, $f(\mathbf{x},\mathbf{v},t)$, can be obtained using the scattering kernel.

The number flux of striking molecules to a surface element *dA* in vicinity of point **x** in the time interval between *t* and $t+\tau$ is

$$F_{imp} = f(\mathbf{x},\mathbf{v},t)\mathbf{v}\cdot\mathbf{n}dtdAd\mathbf{v} \qquad \textbf{(2.32)}$$

where f^- is the distribution function of impinging molecules, **n** is the normal unit vector outwards from the surface at point **x**. Therefore, for impinging molecules $\mathbf{v}\cdot\mathbf{n}<0$, and for reflected molecules $\mathbf{v}'\cdot\mathbf{n}>0$ are written. Similarly, the number flux of reflected molecules is

$$F_{ref} = f(\mathbf{x},\mathbf{v}',t+\tau)\mathbf{v}'\cdot\mathbf{n}dtdAd\mathbf{v}' \qquad \textbf{(2.33)}$$

where f^+ is the distribution function of reflected molecules. When the permanent adsorption on the surface is excluded, the number flux of impinging and reflected molecules must be equal, $F_{ref}=F_{imp}$. However, we must know the probability relation between **v** and $\mathbf{v}'$, $R(\mathbf{v}\to\mathbf{v}',\mathbf{x},t\to t+\tau)$, in order to find the distribution of reflected molecules. Hence, assuming the adsorption time (or time delay in bouncing process) is negligible (i.e. $\tau=0$) we obtain

$$f(\mathbf{x},\mathbf{v}',t) = \int_{\mathbf{v}} R(\mathbf{v}\to\mathbf{v}',\mathbf{x},t)\, f(\mathbf{x},\mathbf{v},t)d\mathbf{v} \qquad \textbf{(2.34)}$$

where *R* is the scattering kernel. The scattering kernel is supposed to have following properties (Cercignani, 2000):

1. The scattering kernel is a nonnegative valued function

$$R(\mathbf{v}\to\mathbf{v}',\mathbf{x},t)\geq 0 \qquad \textbf{(2.35)}$$

2. Total probability of all possible reflections must be equal to unity

$$\int_{\mathbf{v}'} R(\mathbf{v} \to \mathbf{v}', \mathbf{x}, t) d\mathbf{v}' = 1 \tag{2.36}$$

3. The reciprocity principal states the *energy* reversibility of scattering process at local equilibrium

$$\begin{aligned} &R(\mathbf{v} \to \mathbf{v}', \mathbf{x}, t) \exp\ -E_{imp} / kT_w\ \ (\mathbf{v} \cdot \mathbf{n}) = \\ &-R(-\mathbf{v}' \to -\mathbf{v}, \mathbf{x}, t) \exp\ -E_{ref} / kT_w\ \ (\mathbf{v}' \cdot \mathbf{n}) \end{aligned} \tag{2.37}$$

where E_{imp} and E_{ref} are the energy of impinging and reflected molecules, respectively, k is the Boltzmann constant, T_w is the wall temperature and $\exp(-E/kT)$ is the most probably energy state of the molecule (Shen, 2005).

2.3.1 Specular and diffusive reflection models

The specular and diffusion reflection model was first developed by Maxwell (1879) assuming that contact surface is elastic and smooth. Maxwell, in this paper, conveyed a statistical calculation of the effective sliding of gas over a surface and derived a macroscopic slip boundary condition. The specular reflection is simply a "mirror" reflection; a reflected molecule will have a reversed normal velocity of incident molecule while other velocity components remain unchanged during the gas-wall collision. Hence, the distribution function of reflected molecule simply can be written

$$f(\mathbf{x}, \mathbf{v}', t) = f(\mathbf{x}, \mathbf{v} - 2\mathbf{n}(\mathbf{v} \cdot \mathbf{n}), t) \tag{2.38}$$

where **n** is the normal vector outwards from the surface at point **x**, $\mathbf{v} - 2\mathbf{n}(\mathbf{v} \cdot \mathbf{n})$ is the velocity vector of impinging molecule where the direction of normal velocity component is reversed. The scattering kernel of the specular reflection can be written as

$$R_s(\mathbf{v} \to \mathbf{v}', \mathbf{x}, t) = \delta(\mathbf{v} - 2\mathbf{n}(\mathbf{v} \cdot \mathbf{n})) \tag{2.39}$$

where $\delta(\mathbf{u})$ is the Dirac delta function concentrated at **u**.

The diffuse reflection manifests that a molecule is reflected in any direction uncorrelated with impinging molecule at the equilibrium state of the wall. The distribution of diffuse reflection is the Maxwellian distribution

$$f(\mathbf{x},\mathbf{v}',t)=\left(\frac{m}{2\pi kT_w}\right)^{3/2}\exp\left(-\frac{m}{2kT_w}\mathbf{v}'^2\right) \tag{2.40}$$

where T_w is the temperature of the wall. Thus the scattering kernel of diffuse reflection using can be written as [see for details (Sone, 2002; Shen, 2005)]

$$R_d(\mathbf{v}\to\mathbf{v}',\mathbf{x},t)=\frac{2}{\pi}\left(\frac{m}{2T_w}\right)^2\exp\left(-\frac{m}{2kT_w}\mathbf{v}'^2\right). \tag{2.41}$$

Maxwell (1879) considered that σ portion of the impinging molecules are reflected diffusively and rest ($(1-\sigma)$ portion) of the molecules are reflected specularly. σ is later will be called as tangential momentum accommodation coefficient.

$$\begin{aligned}R_M(\mathbf{v}\to\mathbf{v}',\mathbf{x},t)&=(1-\sigma)R_s+\sigma R_d\\&=(1-\sigma)\delta(\mathbf{v}-2\mathbf{n}(\mathbf{v}\cdot\mathbf{n}))+\sigma\frac{2}{\pi}\left(\frac{m}{2T_w}\right)^2\exp\left(-\frac{m}{2kT_w}\mathbf{v}'^2\right).\end{aligned} \tag{2.42}$$

2.3.2 Cercignani, Lampis and Lord (CLL) model

Cercignani and Lampis (1971) developed an alternative model to The Maxwell scattering gas-wall interaction model in Eq. (2.42). The Cercignani-Lampis scattering kernel is characterized by two adjustable parameters, namely; the energy accommodation coefficient, σ_T , and the tangential momentum accommodation coefficient, σ . In this model, the tangential and normal velocity components of the reflected molecules are assumed to be uncorrelated. The scattering kernel for the tangential velocity component is written as

$$R_t(v_t\to v_t',\mathbf{x},t)=\pi\sigma(2-\sigma)^{-1/2}\exp\left(-\frac{v_t'-(1-\sigma)v_t{}^2}{\sigma(2-\sigma)}\right) \tag{2.43}$$

where v_t and v_t' are the tangential velocity components of impinging and reflected molecules, respectively. The scattering kernel for the normal velocity component is written as

$$R_n(v_n \to v_n', \mathbf{x}, t) = \frac{2v_n'}{\sigma_T} I_0\left(\frac{2(1-\sigma_T)^{1/2} v_n v_n'}{\sigma_T}\right) \exp\left(-\frac{v_n'^2 + (1-\sigma_T)v_n^2}{\sigma_T}\right) \quad \textbf{(2.44)}$$

where v_n and v_n' are the normal velocity components of impinging and reflected molecules, respectively, and $I_0(\cdot)$ is the zeroth-order modified Bessel function of the first kind. It is important to note that velocity components in Eqs. (2.43) and (2.44) are normalized by the most probably molecular speed at the surface temperature, $\sqrt{2RT_w}$, where R is the gas constant.

Lord (1991) and Lord (1995) adapted and implemented the Cercignani-Lampis model in DSMC. Therefore this model is often called Cercignani-Lampis-Lord (CLL) model.

2.4 Moment Models

The moment method can be considered as a bridge between the kinetic theory and the continuum mechanics. The general solution of the Boltzmann equation is not available, however the macroscopic flow equations can be obtained without solving it. By multiplying the Boltzmann equation with the mass m, the momentum mv and the molecular kinetic energy $1/2m|v|^2$, $v \in \mathbb{R}^3$, and integrating from $-\infty$ to ∞, five equations of the conservation laws of the macroscopic flow can be obtained as (Chapman and Cowling, 1991; Liou and Fang, 2005; Shen, 2005):

$$\frac{\partial \rho}{\partial t} + \sum_{i=1}^{3} \frac{\partial}{\partial x_i}(\rho v_i) = 0 \quad \textbf{(2.45)}$$

$$\frac{\partial v_i}{\partial t} + \sum_{j=1}^{3}\left(v_i \frac{\partial v_i}{\partial x_j} + \frac{1}{\rho}\frac{\partial \tau_{ij}}{\partial x_j}\right) = 0 \quad \textbf{(2.46)}$$

$$\frac{\partial p}{\partial t} + \sum_{i=1}^{3}\left(\frac{\partial\ pv_i}{\partial x_i} + \frac{2}{3}\frac{\partial q_i}{\partial x_i} + \frac{2}{3}\sum_{j=1}^{3}\tau_{ij}\frac{\partial v_i}{\partial x_j}\right) = 0 \quad \textbf{(2.47)}$$

where, ρ is the density, $\mathbf{v}$ is the velocity vector, τ is the stress tensor, p is the pressure and $\mathbf{q}$ is the heat flux vector. These five equations represent the conservation laws containing thirteen unknowns. Therefore either stress and heat flux terms must be found in terms of density, velocity, temperature and their space

derivatives, or additional equations for stress and heat flux must be found using higher-order moments in order to end up with a closed system. These two approaches are called the Chapman-Enskog method and the moment method, respectively.

For the closure problem above, Chapman and Enskog independently expanded the distribution function into series in terms of powers of Knudsen number, assuming Knudsen number is small. Using this expansion (Chapman-Enskog expansion) stress and heat flux expressions can be obtained from the Boltzmann equation. Then substituting these expressions into the macroscopic flow equations mentioned above, the Euler, the Navier-Stokes, the Burnett and the super-Burnett equations are obtained as the zeroth-, first-, second- and third-order approximation of the Chapman-Enskog expansion (Struchtrup, 2005).

While the Chapman-Enskog method finds the stress and the heat flux in terms of density, velocity, temperature and their space derivatives, Grad (1949) obtained thirteen equations for thirteen unknowns expanding the distribution function into the Hermite polynomials. He expanded the distribution function into Hermite polynomials (see (Sone, 2002; Sone, 2007) for asymptotic approaches for the Boltzmann equation) then he substituted the expansion into the Boltzmann equation and evaluated the higher-order moments.

The macroscopic flow equations can be obtained using the Chapman-Enskog and the moment method. However, they share the problem of how to describe the boundary conditions for higher moments and higher derivatives (Struchtrup, 2005). The main challenge again is the correct form of the boundary condition.

3. NUMERICAL SOLUTION OF THE BOLTZMANN EQUATION USING DIRECT SIMULATION MONTE CARLO (DSMC) METHOD

3.1 Introduction

The Boltzmann equation (BE) describes the change of the number of gas particles inside a unit volume. It is valid at all Knudsen numbers for all flow regimes. The unknown function in the BE is a probability density function and contains seven variables, namely; time, three spatial components and three velocity components. The collision term of the BE makes the equation a nonlinear integro-differential equation and the general solution of the BE is not available. Moreover, numerical solution of the BE is not easy and often computationally time consuming. This chapter considers the direct simulation Monte-Carlo method which is one of the most effective techniques for solving the BE (Bird, 1994).

The DSMC method is a stochastic particle method based on the kinetic theory and assumptions of the collision operator of the Boltzmann equation. The idea behind the DSMC is the separation of the transport and collision parts of the Boltzmann equation and solving them sequentially during each time interval. Therefore, the simulation time step must be less than the time taken between two collisions (molecular mean collision time, for air at STP conditions is around 10^{-10} seconds). Each simulated particle represents a large number of molecules, and therefore we do not have to track a tremendous number of particles at each time step. This is an important advantage of the DSMC over the molecular dynamics approach. Another important feature of the DSMC method is that it is unconditionally stable, which means that we are free to choose the magnitudes of the time step, the cell size and the number of particles, and DSMC will eventually converge without any constraints. However, when the number of particles is small and/or the cell size is large, statistical noise significantly increases, macroscopic quantities are evaluated with considerable error, and therefore reliability of results becomes an issue. This is due to the fact that, the collision term of the Boltzmann equation is simulated by random

numbers based on the molecular chaos assumption of the collision procedure. This collision procedure introduces a statistical noise which is in the order of $1/\sqrt{N}$, where N is the sample size (i.e. total number of particles in the simulation). Important to note that, flows associated with micro-devices are generally slow and capturing real flow motion among the gas molecules, which travel in air at the speed of sound, is difficult in the presence of statistical noise. In addition, the flow domain is divided into cells where each cell dimension should be set to be less than one mean free path (generally specified as $\leq \lambda/3$), since the flow properties should not change inside a cell (Oran et al., 1998). Additionally, the time step is specified as less than the mean collision time due to the uncoupling of the molecular motions and the intermolecular interactions.

Since the DSMC method converges unconditionally to a solution, it is crucial to be aware of the reliability of the result. In order to do that, we need to consider the presence of three possible types of error in a DSMC simulation. The first type of error is the numerical error, which has three main causes (1) the finite cell size, (2) finite size of time step and (3) the fewer number of simulation particles compared to the real number of particles. The second type of the error is the result of uncertainty, which occurs due to the chaos assumption of the collision operator and the statistical nature of the gas-wall interactions, which are both modelled using random numbers. The third type of the error is the result of inadequacies due to the choice of input parameters such as collision interaction potential (or the choice of the cross section, (see Chapter 2)), for example choosing the hard-sphere or Maxwellian gas model. All these errors can be controlled by using appropriate values of parameters at the initiation process of the DSMC procedure.

Let the domain D of a gas divided into M cells, $\mathbf{dC}^{(l)} \quad l = 1, 2, \ldots, M$, and let $\mathbf{x}^{(l)} \in \mathbf{dC}^{(l)}$ is an arbitrary point represents the cell. Then the velocity distribution function can be written as (Sone, 2007)

$$f(\mathbf{x}^{(l)}, \mathbf{v}, t)\mathbf{dC}^{(l)} = \Delta \sum_{j=1}^{N^{(l)}} \delta(\mathbf{v} - \mathbf{v}_{(j)}^{(l)}), \qquad \mathbf{x}^{(l)} \in \mathbf{dC}^{(l)} \tag{3.1}$$

and

$$f(\mathbf{x},\mathbf{v},t)=\Delta\sum_{l=1}^{M}\sum_{j=1}^{N^{(l)}}\delta(\mathbf{x}-\mathbf{x}_{(j)}^{(l)})\delta(\mathbf{v}-\mathbf{v}_{(j)}^{(l)}),\qquad \mathbf{x}\in D \tag{3.2}$$

where δ is the three-dimensional Dirac delta function, Δ is a constant and $N^{(l)}$ is the particles in $\mathbf{dC}^{(l)}$. The initial position $\mathbf{x}_{(j)}^{(l)}\in\mathbb{R}^3$ and velocity $\mathbf{v}_{(j)}^{(l)}\in\mathbb{R}^3$ of particles are determined by initial Maxwellian distribution (density distribution, accordingly) subject to the initial temperature, bulk velocity and number of simulation particles *N*. The constant Δ is $V^{(l)}/N^{(l)}$ where $V^{(l)}$ is the volume of $\mathbf{dC}^{(l)}$ and $N^{(l)}$ is the number of particles in $\mathbf{dC}^{(l)}$, so that Δ is inversely proportional to the number density. It is important to note that number of particles, $N^{(l)}$, in $\mathbf{dC}^{(l)}$ will vary with time through collisions.

When position $\mathbf{x}_{(j)}^{(l)}$ and velocity $\mathbf{v}_{(j)}^{(l)}$ of all particles are given at time *t*, due to the advection (left-hand) part of the Boltzmann equation, the position and velocity of particles can be shifted as $\mathbf{x}_{(j)}^{(l)}+\mathbf{v}_{(j)}^{(l)}dt$ and $\mathbf{v}_{(j)}^{(l)}+\mathbf{F}(\mathbf{x}_{(j)}^{(l)},\mathbf{v}_{(j)}^{(l)},t)dt$ where $\mathbf{F}$ is the external force in the Boltzmann equation. Then the distribution function *f* is shifted to

$$f(\mathbf{x},\mathbf{v},t)=\Delta\sum_{l=1}^{M}\sum_{j=1}^{N^{(l)}}\delta(\mathbf{x}-\mathbf{x}_{(j)}^{(l)}-\mathbf{v}_{(j)}^{(l)}dt)\delta(\mathbf{v}-\mathbf{v}_{(j)}^{(l)}-\mathbf{F}(\mathbf{x}_{(j)}^{(l)},\mathbf{v}_{(j)}^{(l)},t)dt),\qquad \mathbf{x}\in D \tag{3.3}$$

A particle can enter a different cell after shift, and the indexing must be amended as $(i,j)\to(\bar{i},\bar{j})$. After shifting, if any particles strikes into the boundary ∂D, appropriate boundary condition must be employed, which is described in detail in Section 3.2.

For collision process, let the probability of finding the parameter $\varpi\in S^2$ in a solid angle element $d\Omega^{(s)}$ for a velocity pair $(\mathbf{v}_{(j)}^{(l)},\mathbf{v}_{(k)}^{(l)})$ is

$$P^{(s)}(\mathbf{v}_{(j)}^{(l)},\mathbf{v}_{(k)}^{(l)})d\Omega^{(s)}=\frac{\Delta dt}{m\mathbf{dC}^{(l)}}B\left(\left|(\mathbf{v}_{(k)}^{(l)}-\mathbf{v}_{(j)}^{(l)})\cdot\varpi\right|\Big/\left|\mathbf{v}_{(k)}^{(l)}-\mathbf{v}_{(j)}^{(l)}\right|,\left|\mathbf{v}_{(k)}^{(l)}-\mathbf{v}_{(j)}^{(l)}\right|\right)d\Omega^{(s)} \tag{3.4}$$

where $B(v_1-v_2,\varpi)$ is the collision kernel described in the previous chapter, *m* is the molecular mass, and $(\cdot,\cdot)$ is the scalar product in $\mathbb{R}^3$. Velocity pair $(\mathbf{v}_{(j)}^{(l)},\mathbf{v}_{(k)}^{(l)})$ in $\mathbf{dC}^{(l)}$ is chosen randomly by ignoring locations of particles. If ϖ realizes in $d\Omega^{(s)}$

for some *s*, particles collide and velocities are transformed from $(\mathbf{v}_{(j)}^{(l)}, \mathbf{v}_{(k)}^{(l)})$ to $(\mathbf{v}_{(j)}'^{(l)}, \mathbf{v}_{(k)}'^{(l)})$ by the formula

$$\mathbf{v}_{(j)}'^{(l)} = \mathbf{v}_{(j)}^{(l)} + [(\mathbf{v}_{(k)}^{(l)} - \mathbf{v}_{(j)}^{(l)}) \cdot \boldsymbol{\varpi}^{(s)}]\boldsymbol{\varpi}^{(s)} \tag{3.5}$$

and

$$\mathbf{v}_{(k)}'^{(l)} = \mathbf{v}_{(k)}^{(l)} - [(\mathbf{v}_{(k)}^{(l)} - \mathbf{v}_{(j)}^{(l)}) \cdot \boldsymbol{\varpi}^{(s)}]\boldsymbol{\varpi}^{(s)} \tag{3.6}$$

Hence, the probability that any pair $(\mathbf{v}_{(j)}^{(l)}, \mathbf{v}_{(k)}^{(l)})$ collides is

$$\begin{aligned} P(\mathbf{v}_{(j)}^{(l)}, \mathbf{v}_{(k)}^{(l)}) &= \sum_s P^{(s)}(\mathbf{v}_{(j)}^{(l)}, \mathbf{v}_{(k)}^{(l)}) d\Omega^{(s)} \\ &= \frac{\pi r^2 \Delta}{m} \frac{dt}{\mathbf{dC}^{(l)}} \left| \mathbf{v}_{(k)}^{(l)} - \mathbf{v}_{(j)}^{(l)} \right| \end{aligned} \tag{3.7}$$

where *r* is the distance between the two molecule centres. The probability of no collision is, accordingly, $1 - P(\mathbf{v}_{(j)}^{(l)}, \mathbf{v}_{(k)}^{(l)})$. Sampling from Eq. (3.7) is carried out by the acceptance-rejection approach, since its cumulative distribution functions cannot be obtained straightforwardly.

The process of DSMC can be summarized as follows. At the beginning of the DSMC method, initial conditions are assigned; nevertheless they do not affect the final result but has an effect on convergence time. The initial position and velocity of particles are determined by Maxwellian distribution function at the initial conditions. Physical domain is divided into computational cells taking into account the flow geometry. Then, the transport part (left-hand side) of the Boltzmann equation is simulated (advection sub-step). Particles are let move for a time less than the molecular mean collision time. All particles are tracked and indexed, and if they interact with a surface, a boundary condition is used. Now all particles have new location and they are indexed again.

Next, the collision procedure is employed using the no-time counter technique (Bird, 1994). Only binary collisions take place and pairs are chosen randomly. We will describe and use slightly modified version of no-time counter technique in this thesis. After the advection and collision sub-steps, we need to average the cell-based data in order to capture crucial information about macroscopic behaviour of the gas. The process above takes place again and again for a pre-assigned number of steps

until the macroscopic quantities are obtained within prescribed accuracy. Figure 3.1 shows the DSMC flowchart.

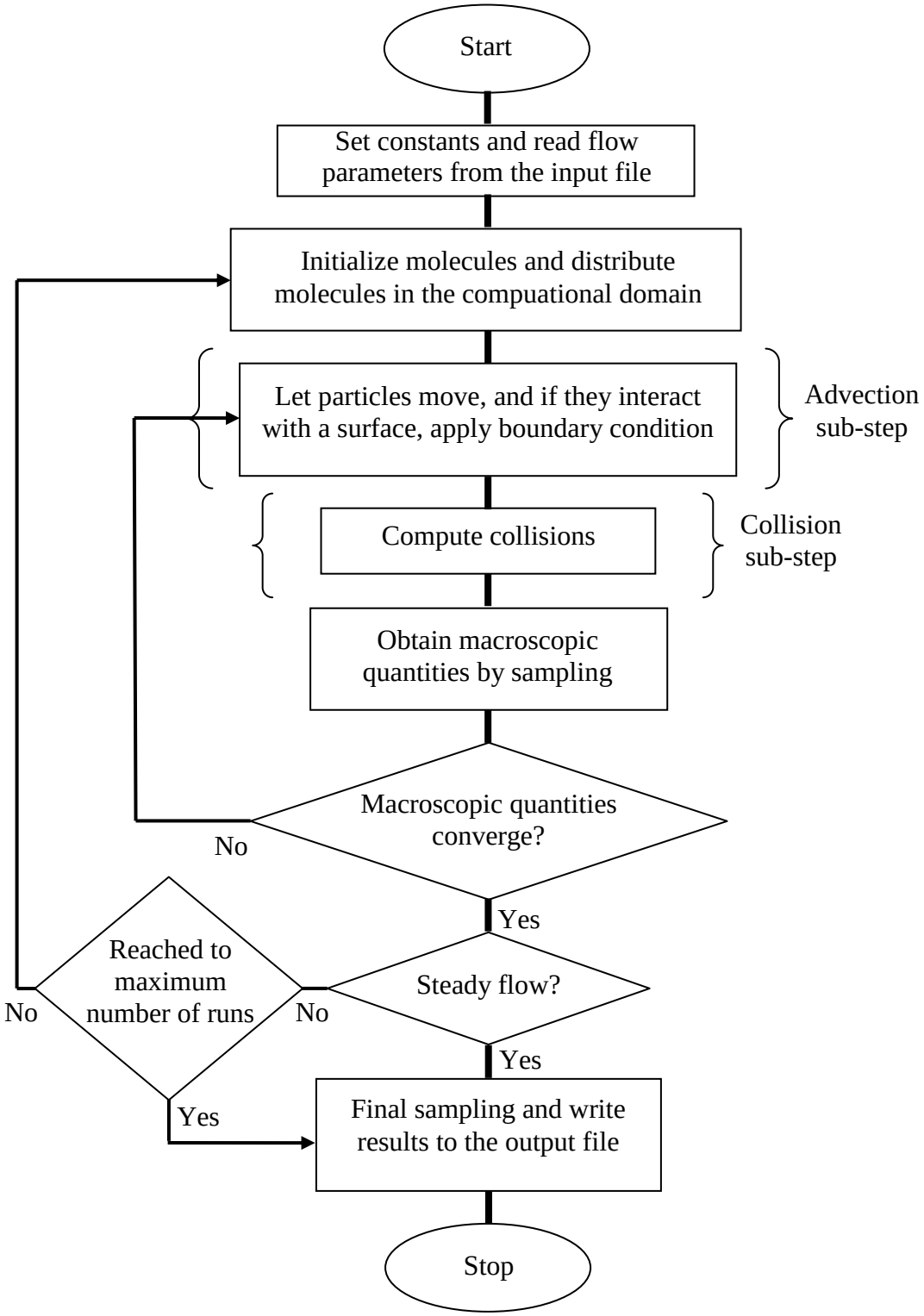

Figure 3.1: DSMC flowchart.

The DSMC method is inherently time-dependent, and a simulation runs in time marching manner that can be related to physical time. However, in unsteady flows, independent simulations with identical initial conditions must be run many times and then results must be sampled in order to obtain meantime flow profiles.

3.2 Obtaining the Macroscopic Quantities

At each DSMC step as shown in Figure 3.1, macroscopic quantities must be calculated by averaging the microscopic values obtained in the centre of each cell. The flow density and velocities in *x*-, *y*- and *z*-directions can be obtained using following equations (Liou and Fang, 2005):

$$\rho = \frac{1}{N_t}\frac{N F_{num}}{\Delta V} m \tag{3.8}$$

$$U = \frac{1}{N}\sum_{i=1}^{N_t}\sum_{j=1}^{N_i} c_{U,j}, \quad \mathrm{V} = \frac{1}{N}\sum_{i=1}^{N_t}\sum_{j=1}^{N_i} c_{V,j}, \quad \mathrm{W} = \frac{1}{N}\sum_{i=1}^{N_t}\sum_{j=1}^{N_i} c_{W,j} \tag{3.9}$$

where $N = \sum_{i=1}^{N_T} N_i$ is the total number of particles that are indexed, N_i is the number of particles in *i*-th time step, N_t is the number of total time steps, ΔV is the volume element, F_{num} is the number of real molecules which are simulated and represented by a particle, m is the molecular mass, and $c_{U,j}$, $c_{V,j}$ and $c_{W,j}$ are the molecular velocity components in the *x*-, *y*, and *z*-directions, respectively, of *j*-th molecule. The temperatures in the *x*-, *y*, and *z*-directions are obtained as

$$T_x = \frac{m}{k_B}\left[\frac{1}{N}\sum_{i=1}^{N_t}\sum_{j=1}^{N_i} c_{U,j}^2 - \left(\frac{1}{N}\sum_{i=1}^{N_t}\sum_{j=1}^{N_i} c_{U,j}^2\right)^2\right] \tag{3.10}$$

$$T_y = \frac{m}{k_B}\left[\frac{1}{N}\sum_{i=1}^{N_t}\sum_{j=1}^{N_i} c_{V,j}^2 - \left(\frac{1}{N}\sum_{i=1}^{N_t}\sum_{j=1}^{N_i} c_{V,j}^2\right)^2\right] \tag{3.11}$$

$$T_z = \frac{m}{k_B}\left[\frac{1}{N}\sum_{i=1}^{N_t}\sum_{j=1}^{N_i} c_{W,j}^2 - \left(\frac{1}{N}\sum_{i=1}^{N_t}\sum_{j=1}^{N_i} c_{W,j}^2\right)^2\right] \tag{3.12}$$

where k_B is the Boltzmann constant. Then the flow temperature and pressure can be obtained as

$$T = \frac{T_x + T_y + T_z}{3} \tag{3.13}$$

$$p = \left(\frac{1}{N_t} \frac{N F_{num}}{\Delta V} m \right) k_B T \tag{3.14}$$

The shear stress τ_w and heat flux q_w on the surface and can be obtained as

$$\tau_w = \frac{F_{num}}{t_S \Delta A} \sum_{j=1}^{N_S} m\left(c_{t,j}^r - c_{t,j}^i \right) \tag{3.15}$$

$$q_w = \frac{F_{num}}{t_S \Delta A} \left[\sum_{j=1}^{N_S} \frac{1}{2} m\left((c_j^2)^r - (c_j^2)^i \right) \right] \tag{3.16}$$

where ΔA is are element that gas-wall interaction takes place, t_S is the time interval that gas-wall interaction occurs, N_S is the total number of particles striking into the wall, c_t is the molecular velocity of the tangential component, the superscripts "*i*" and "*r*" denote the molecular velocity of the particle before and after the impact, respectively.

3.3 Implementation of Gas-Wall Interaction Models In Direct Simulation Monte Carlo (DSMC) Method

DSMC method is one of the most effective techniques for solving the Boltzmann equation (Bird, 1994). It is proven that DSMC method converges to the solution of the Boltzmann equation in limit of infinitesimal discretization if a large number of particles are used in the simulation (Wagner, 1992; Rjasanov and Wagner, 2005). Some recent improvements in DSMC for application to (low-speed) microflows can be found (Fan and Shen, 2001; Macrossan 2001; Homolle and Hadjiconstantinou, 2007; Radtke et al., 2011; Stefanov, 2011).

In the implementation of the Maxwell (specular-diffusive) gas-wall interaction model in the DSMC simulations, $1-\sigma$ portion of the molecules reflects specularly (mirror reflection) from the surface while σ portion of the molecules reflects diffusively. Implementation of the specular reflection model in the DSMC method is straightforward. When a particle strikes into the wall, the normal velocity component of the particle is simply inverted and directed back into the flow domain. Other

velocity components remain unchanged. For the diffuse reflection, the reflected tangential velocity of the particle is considered to be uncorrelated with its impinging velocity and particle bounces off the surface according to the Maxwell distribution:

$$f = \left(\frac{\beta}{\pi^{1/2}} \right)^3 \exp\left(-\beta^2 (\mathbf{v}') \right) \quad \textbf{(3.17)}$$

where $\beta = \left(2 \frac{k}{m} T_w \right)^{-1/2}$.

Therefore the normal component distribution of the reflected molecule can be related as

$$f_n \propto \exp\left(-\beta^2 v_n'^2 \right). \quad \textbf{(3.18)}$$

Hence the reflecting normal velocity can be sampled from expression (3.18) using the inversion of cumulative distribution technique [see for details (Shen, 2005; Liou and Fang, 2005)] as

$$v_n' = \left(-\ln(rand) \right)^{1/2} / \beta \quad \textbf{(3.19)}$$

where *rand* is a random number generated from uniform distribution between 0 and 1.

On the reflecting surface, according to the cosine law proposed by Knudsen (1915), particle reflections over each azimuth are uniformly distributed. Thus in tangential plane (η, ξ), reflecting tangential velocity components can be sampled as

$$v_\eta' = V' \cos\theta \text{ and } v_\xi' = V' \sin\theta \quad \textbf{(3.20)}$$

where $V' = \sqrt{v_\eta'^2 + v_\xi'^2} = \left(-\ln(rand_1) \right)^{1/2} / \beta$. Azimuth angle, θ, is sampled as

$$\theta = 2\pi \, rand_2 \quad \textbf{(3.21)}$$

where $rand_1$ and $rand_2$ are two independent random numbers generated from uniform distribution between 0 and 1.

Using CLL (Cercignani-Lampis-Lord) scattering kernel for the tangential and normal velocity components mean velocities $\overline{v}_t'$ and $\overline{v}_n'$ can be obtained as

$$\begin{aligned}\overline{v}_t' &= \int_{-\infty}^{\infty} v_t' R_t(v_t \to v_t', \mathbf{x}, t) dv_t' \\ &= \int_{-\infty}^{\infty} v_t' \left(\pi\sigma(2-\sigma)\right)^{-1/2} \exp\left(-\frac{\left(v_t' - (1-\sigma)v_t\right)^2}{\sigma(2-\sigma)}\right) dv_t' = (1-\sigma)v_t\end{aligned} \tag{3.22}$$

and

$$\begin{aligned}\overline{v}_n' &= \int_{-\infty}^{\infty} v_n' R_n(v_n \to v_n', \mathbf{x}, t) dv_n' \\ &= \int_{-\infty}^{\infty} v_n' \frac{2v_n'}{\sigma_T} I_0\left(\frac{2(1-\sigma_T)^{1/2} v_n v_n'}{\sigma_T}\right) \exp\left(-\frac{v_n'^2 + (1-\sigma_T)v_n^2}{\sigma_T}\right) dv_n' \\ &= \sqrt{\sigma_T}\left((1-2\gamma)I_0(\gamma) - 2\gamma I_1(\gamma)\right)\sqrt{\pi}\exp(\gamma)\end{aligned} \tag{3.23}$$

where $I_0(\cdot)$ and $I_1(\cdot)$ are the zeroth- and first-order modified Bessel functions of the first kind, respectively, and $\gamma = (-1+\sigma_T)v_n^2/(2\sigma_T)$. Notice that, for $\sigma_T = 1$, mean normal velocity is $\sqrt{\pi}$.

The tangential component distribution of the reflected molecule can be related as

$$f_t \propto \exp\left(-\frac{V'^2}{\sigma(2-\sigma)}\right) \tag{3.24}$$

where $V' = v_t' - (1-\sigma)v_t$. Hence the reflecting tangential velocity can be sampled from Eq. (3.24) using the inversion of cumulative distribution technique (Shonkwiler and Mendivil, 2009) as

$$V' = \left(-\sigma(2-\sigma)\ln(rand)\right)^{1/2} \tag{3.25}$$

According to the cosine law (Knudsen, 1915), particle reflections over each azimuth is uniformly distributed. Therefore multiplying $V' = v_t' - (1-\sigma)v_t$ with $\cos\theta$ and $\sin\theta$, we obtain

$$V'\cos\theta = v_t'\cos\theta - (1-\sigma)v_\eta \text{ and } V'\sin\theta = v_t'\sin\theta - (1-\sigma)v_\xi \tag{3.26}$$

Therefore

$$v_\eta' = V'\cos\theta + (1-\sigma)v_\eta \text{ and } v_\xi' = V'\sin\theta + (1-\sigma)v_\xi \tag{3.27}$$

where azimuth angle, θ, is sampled as

$$\theta = 2\pi\, rand \tag{3.28}$$

here *rand* is a random number generated from uniform distribution between 0 and 1.

The reflecting normal velocity can be considered as combination of tangential components and sampled as

$$\begin{aligned} v_n' &= \sqrt{v_\eta' + v_\xi'} \\ &= \sqrt{V'^2 + (1-\sigma)^2 v_n^2 + 2V'(1-\sigma)v_n} \end{aligned} \tag{3.29}$$

For two dimensional case, Eq. (3.29) is written as

$$v_n' = \sqrt{V'^2 + (1-\sigma)^2 v_n^2 + 2V'(1-\sigma)v_n \cos\theta}\,. \tag{3.30}$$

3.4 Direct Simulation Monte Carlo (DSMC) Solutions of Three Fundamental Flow Problems

Using DSMC, solutions to three isothermal Couette flows, namely, (a) flow between two parallel plates, (b) flow between two rotating cylinders, and (c) flow within a rotating cylinder are obtained. The first- and second-order slip models have also been solved and compared with the DSMC data. Slip boundary conditions are explained in detail in Chapter 5. Finally, velocity profiles are examined in order to highlight the significance of the surface shape and distinguish the Knudsen layer and S-layer effects.

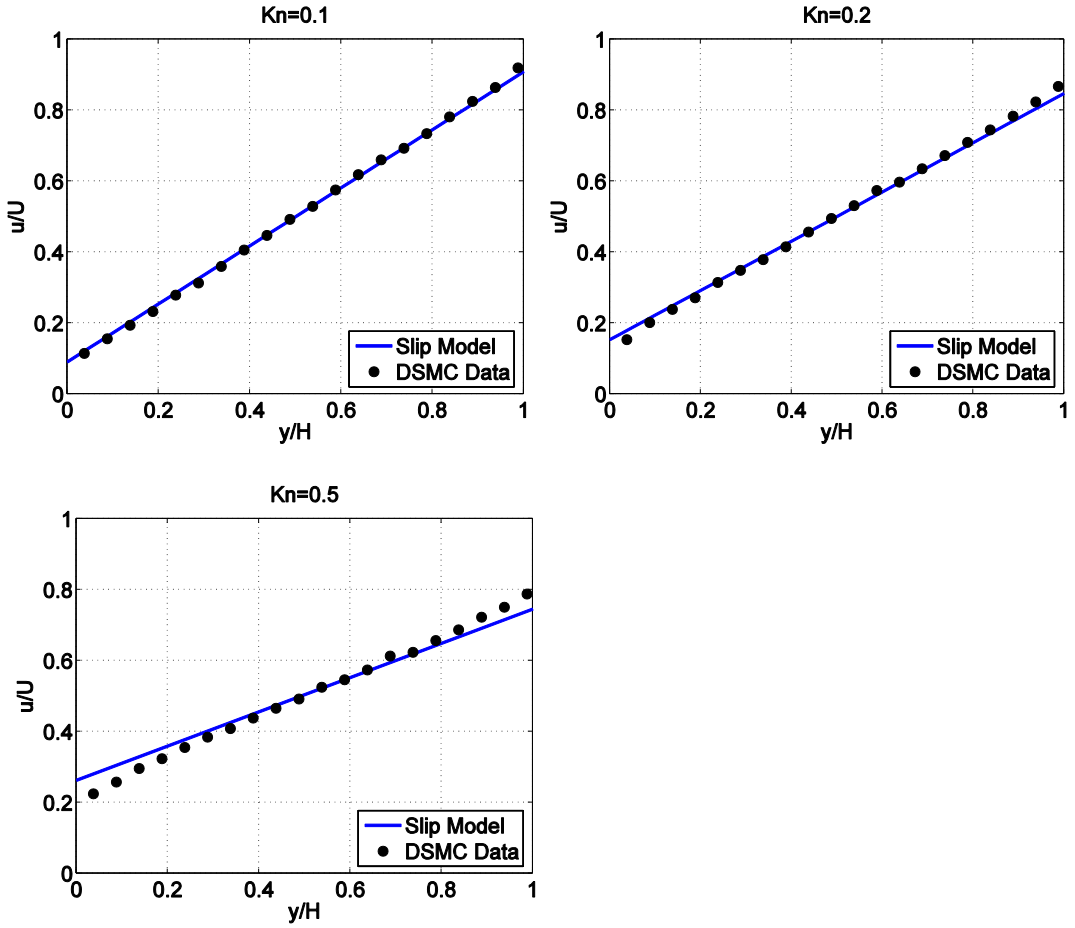

Figure 3.2: The velocity profiles of planar Couette flow. H is the gap between plates. Solid lines represent second-order slip model with $A_1 = 1.11$ and $A_2 = 0.61$. Dotted lines represent DSMC data.

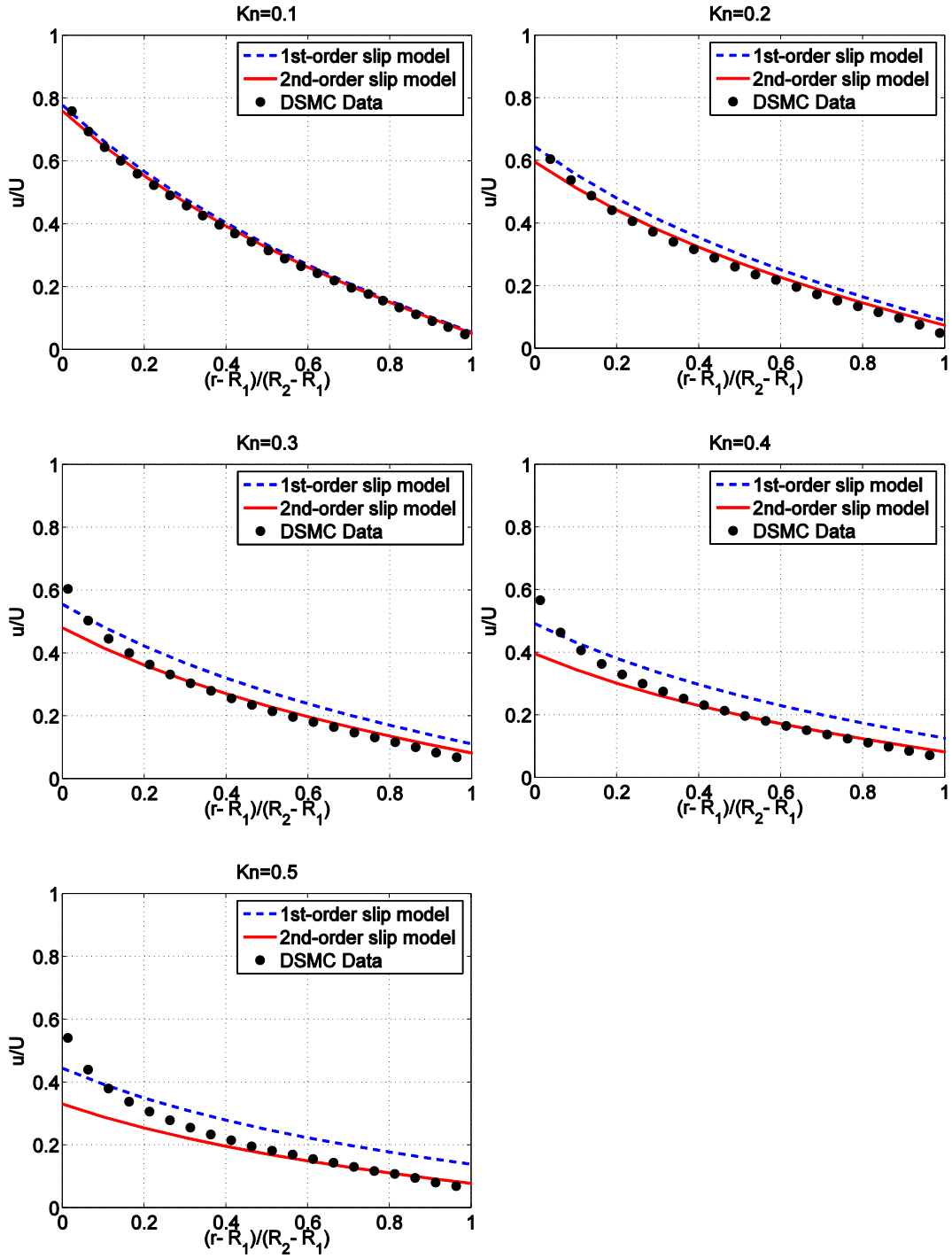

Figure 3.3: The velocity profiles of the cylindrical Couette flow. The inner cylinder is rotating while the outer cylinder is stationary. Solid line is second-order slip solution, dashed line is first-order slip solution and dotted line is DSMC data. The ratio between cylinder radii is 2, (i.e. $R_2 / R_1 = 2$).

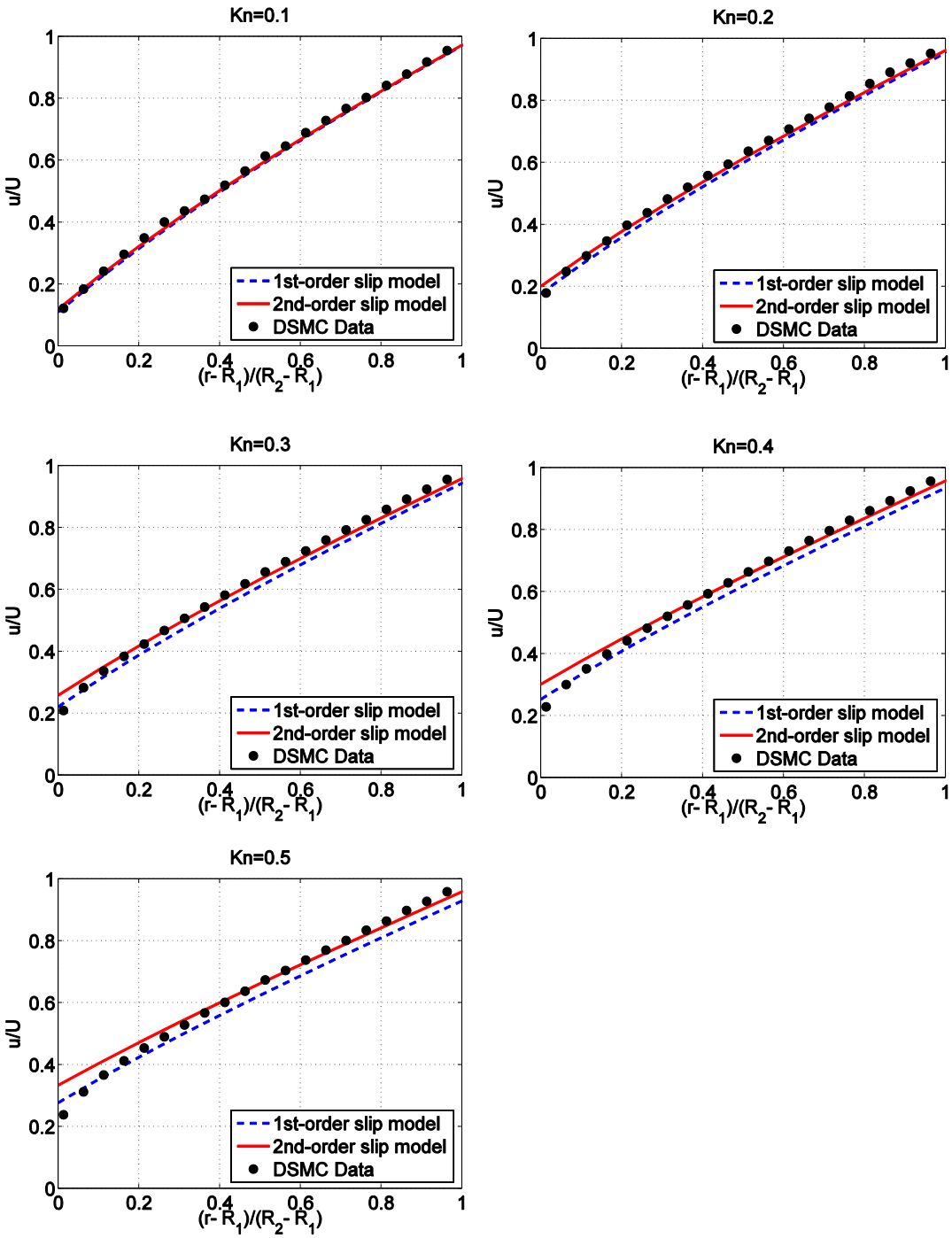

Figure 3.4: The velocity profiles of the cylindrical Couette flow. The outer cylinder is rotating while the inner cylinder is stationary. Solid line is second-order slip solution, dashed line is first-order slip solution and dotted line is DSMC data. The ratio between cylinder radii is 2, (i.e. $R_2 / R_1 = 2$).

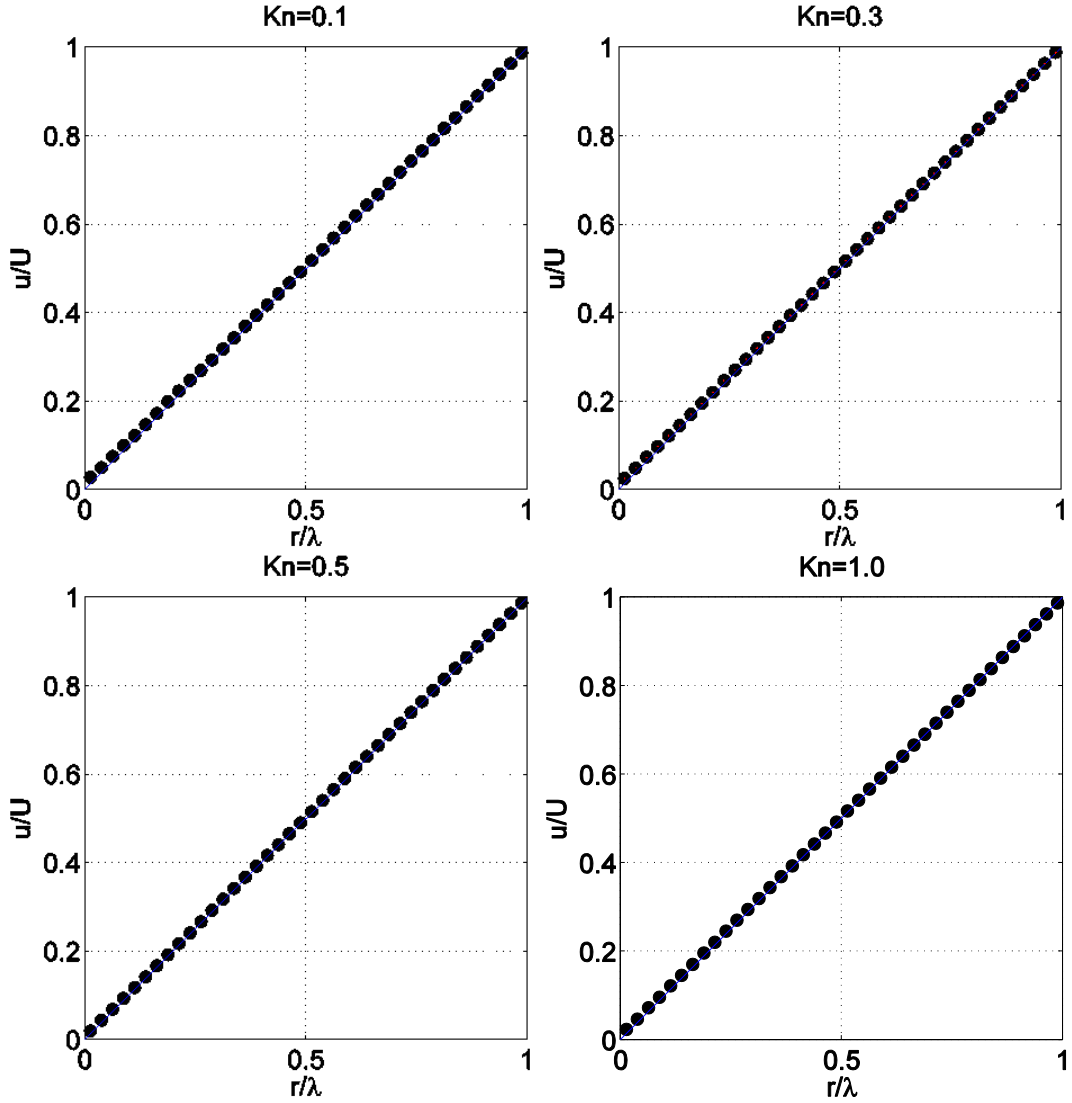

Figure 3.5: The velocity profiles of the flow inside a rotating cylinder. The dotted lines represent DSMC data whereas solid lines (which completely coincide with the DSMC solution) represent the slip model profile. Figures show that there is no slip at the cylinder surface although a Knudsen layer is expected to form on the surface.

4. NUMERICAL SOLUTION OF THE BOLTZMANN EQUATION USING DISCRETE VELOCITY (DV) METHOD

4.1 Introduction

In this chapter, we consider the deterministic numerical solution of the Boltzmann equation using the discrete velocity (DV) method. The DV method can be considered as the finite difference solution of the Boltzmann equation; therefore the solution data do not contain any noise, unlike the DSMC results. The DV method for steady (i.e. time-independent) flows associated with simple geometries can outperform the DSMC approach in terms of computational time. Since many micro-electro-mechanical systems (MEMS) operate in non-isothermal conditions, this chapter considers thermal effects and solves a heat conduction problem through a rarefied gas between two stationary concentric cylinders using the DV method and compare the results with the first- and second-order temperature-jump models.

Through discrete velocity method, the present chapter investigates the importance of the surface shape in a micro-scale heat conduction problem. A heated infinitely-thin cylindrical shell is positioned in the middle of two concentric cylinders, and the heat transfer through a rarefied gas between the shell and the confining inner (or outer) cylinder is investigated. The study initially considers the solution of the first- and second-order temperature-jump models (i.e. the conventional heat equation with temperature-jump boundary conditions). The study then examines the numerical solution of the nonlinear Shakhov model kinetic equation subject to the Maxwell boundary condition using the DV method. The variable-hard-sphere molecular interaction model is taken into account in the temperature-jump models allowing the presence of significant temperature differences between surfaces to be considered. Anomalous temperature profiles near the convex (or concave) side of the shell are attributed to the effects of surface shape.

The Boltzmann equation is written as

$$\frac{\partial f}{\partial t}+\sum_{i=1}^{3}\left(\mathbf{v}\cdot\frac{\partial f}{\partial x_i}+\mathbf{X}\cdot\frac{\partial f}{\partial v_i}\right)=Q(f_1,f_2) \qquad \textbf{(4.1)}$$

where $f(\mathbf{x},\mathbf{v},t)$ is the distribution function, $\mathbf{x}\in\mathbb{R}^3$ is the position vector and $\mathbf{v}\in\mathbb{R}^3$ is the velocity vector of a molecule at time *t*; ***X*** is the external force and $Q(f_1, f_2)$ is the collision term with distribution functions of the colliding molecules f_1 and f_2 The collision term has been described in detail in Chapter ?, therefore we refer reader to section.

In the Boltzmann equation (4.1), the left-hand side is simply the transport equation. Roughly speaking, the left-hand side of the Eq. (4.1) manifests the conservation of mass. Therefore, when the collision term simulated using the DSMC approach appropriately, left-hand side of the Boltzmann equation (4.1) is satisfied as far as none of the particles disappears. On the other hand, this transport part of the Boltzmann equation is discretized using the finite difference approach in DV method.

The collision operator is assumed to have three main properties (Cercignani, 2000)

1. Gas is dilute enough that only binary collisions take place; in other words, only two molecules are allowed to collide at an instance.
2. Collisions are *elastic* so that momentum and (kinetic) energy are conserved. This assumption leads to *micro-reversibility* property that each collision is (locally) time reversible. The conservation of momentum and energy, can be written, respectively as

   $$v+v_*=v'+v'_* \qquad \textbf{(4.2)}$$

   $$|v|^2+|v_*|^2=|v'|^2+|v'_*|^2 \qquad \textbf{(4.3)}$$

   where v and v_* are the velocities before the collision, v' and v'_* are the velocities after the collision.
3. The velocities of colliding molecules are assumed to be uncorrelated. Although the (elastic) collision process can be modelled using Eqs. (4.2) and (4.3), molecules which are about to collide are not known. However, after any collision, the velocities of the reflecting molecules can be determined

using Eqs. (4.2) and (4.3). This is named as *one-sided chaos*, which is another subtle property of the collision operator.

The BGK (Bhatnagar, Gross and Krook) model proposed by Bhatnagar et al. (1954) and Shakhov model proposed by Shakhov (1968a) and Shakhov (1968b) kinetic equations are obtained by replacing the problematic collision term of the Boltzmann equation by a simpler collision model. The Shakhov model is generally accepted to be more accurate for flows associated with heat transfer compared to the BGK model, since the BGK model is associated with a wrong Prandtl number, which is equal to unity (i.e. Pr=1) instead of Pr=2/3 for monatomic gases (Graur and Polikarpov, 2009).

From the point of view of real applications, understanding the role of heat flow is an essential part of designing various MEMS and NEMS devices. Several microelectronic devices are exposed to a significant quantity of heat in operation, while many microdevices are based on heat transfer phenomena such as thermo-elastic actuators and thermal anemometers (Pelesko and Bernstein, 2003; Nguyen and Wereley, 2006). Some other MEMS devices are designed to enhance the heating or cooling performance by incorporating more complex manifold geometries. However, the role of surface shape and curvature in the heat transfer between a micro-system and its environment has not been fully understood.

The present chapter does not present only the implementation of DV method, but also investigates the importance of the surface shape in micro-scale heat conduction around an infinitely-thin cylindrical shell. A heated cylindrical shell is positioned in the middle of two concentric cylinders, and the heat transfer through a rarefied gas between the shell and the confining inner (or outer) cylinder is investigated. Since the shell has both concave and convex sides with the same surface area and same degree of curvature, any anomalous behaviour in the heat flow over the concave or convex side can be attributed directly to the effects of surface shape. The study initially considers the solution of the first- and second-order temperature-jump models (i.e. the conventional heat equation with temperature-jump boundary conditions) by taking into account the presence of significant temperature gradients. Then, the study examines the numerical solution of the nonlinear Shakhov model kinetic equation subject to the Maxwell boundary condition using the DV method.

The present results reveal the remarkable effects of the surface shape and curvature. The results show that the degree of temperature jump over a convex surface is markedly larger than that over a concave surface. The results clearly demonstrate the difference in the magnitudes of the heat fluxes over the concave and convex surfaces of the shell.

We consider the continuum description of the heat conduction problem around a heated infinitely-thin cylindrical shell positioned in the middle of a gap between two concentric cylinders, in order to compare our DV solution at small Knudsen numbers. The energy equation for the heat transfer through a rarefied gas between the shell and the confining inner (or outer) cylinder can be written in a cylindrical-polar coordinate reference frame as

$$\frac{\partial}{\partial r}\left[k(T)\frac{\partial T}{\partial r} r \right] = 0 \qquad \textbf{(4.4)}$$

where T is the temperature and r is the radial distance. The thermal conductivity $k(T)$ depends on temperature T with a variable hard sphere (VHS) power law $k(T) = k_0 (T/T_0)^{\omega}$, where T_0 is the reference temperature and k_0 is the thermal conductivity at T_0. In the presence of a significant temperature difference between the surface and its environment (i.e. in the presence of significant temperature gradients), the variable hard sphere power law must be taken into account in the modelling. The exponent, ω, typically lies in the range between 0.5 (for hard sphere molecules) and 1 (for Maxwell molecules).

The general solution of equation (4.4) is given by

$$T(r) = (\omega+1)\left[C_1 + C_2 T_0^{\omega} \ln r \right]^{1/(\omega+1)} \qquad \textbf{(4.5)}$$

where C_1 and C_2 are the constants determined by the temperature-jump boundary conditions. The heat flux can then be written as

$$q(r) = -k(T)\frac{dT}{dr} = -\frac{k_0}{r}\left[C_2 \Sigma^{-1+1/(\omega+1)} (1+\omega)^{\omega} \Sigma^{\omega/(\omega+1)} \right] \qquad \textbf{(4.6)}$$

where $\Sigma = C_1 + C_2 T_0^{\omega} \ln r$.

Several first- and second-order temperature-jump boundary conditions are proposed in the literature for modelling the heat transfer over planar surfaces, as reviewed by

Colin (2012). The temperature-jump solutions for the planar geometry are reported to be in good agreement with DSMC data up to a Knudsen number of 0.4 (Wadsworth, 1993). However, relatively little research has been conducted on their accuracy at nonplanar surfaces. The Knudsen number can be defined in terms of the annular gap between the shell and the confining inner (or outer) cylinder, i.e. $Kn = 2\lambda/(R_2 - R_1)$, where R_1 and R_2 are the radii of the inner and outer cylinders, and λ is the mean free path, defined as $\lambda = (\mu/p)(\pi\mathcal{R}T_0/2)^{1/2}$ where p is the pressure, μ is the dynamic viscosity and $\mathcal{R}$ is the specific gas constant. When the mean free path is considered to be globally constant throughout the annular gap, the Knudsen number can be interpreted as a scale parameter which increases monotonically down to the micro/nanoscale.

The second-order temperature-jump boundary condition can be written as

$$T_{jump} = T_{gas} - T_{wall} = \frac{2-\sigma_T}{\sigma_T}\frac{2\gamma}{\gamma+1\ \mathrm{Pr}}\left(\pm\lambda\left.\frac{\partial T}{\partial n}\right|_{wall} - \frac{\lambda^2}{2}\left.\frac{\partial^2 T}{\partial n^2}\right|_{wall}\right) \tag{4.7}$$

where σ_T is the thermal accommodation coefficient, γ is the specific heat ratio, Pr is the Prandtl number and $\partial/\partial n$ is the derivative in the direction normal to the surface. The specific heat ratio, γ, is assumed to be 5/3 and the Prandtl number, Pr, is taken as 2/3 whilst the thermal accommodation coefficient is specified as $\sigma_T = 1.0$ (Sharipov, 2011). We employ a second-order temperature-jump boundary condition with a minus sign in front of the second term of order λ^2 in Eq. (4.7), instead of the positive sign originally proposed by Karniadakis et al. (2005). The first-order temperature jump condition can be obtained by omitting the second term in Eq. (4.7).

The solution of equation (4.4) can be found in the continuum regime for $T(R_1) = T_1$ and $T(R_2) = T_2$ as

$$T_{cont}(r) = (1+\omega)\left[\frac{T_1(T_1/(1+\omega))^{\omega}\ln(r/R_2) - T_2(T_2/(1+\omega))^{\omega}\ln(r/R_1)}{(1+\omega)\ln(R_1/R_2)}\right]^{1/(1+\omega)} \tag{4.8}$$

and the heat flux is given as

$$q_{cont}(r) = -k_0\frac{(1+\omega)^{\omega-1}\left[T_2(T_2/(1+\omega))^{\omega} - T_1(T_1/(1+\omega))^{\omega}\right]}{rT_0^{\omega}\ln(R_2/R_1)} \tag{4.9}$$

When Eq. (4.5) is subjected to temperature-jump conditions, the constants C_1 and C_2 cannot be obtained straightforwardly. These constants are obtained numerically using a technique for the solution of the system of nonlinear equations. The exponent, ω, is set to 0.5 (i.e. hard sphere molecules) unless otherwise stated.

4.2 Discrete Velocity Method with the Nonlinear Shakhov Kinetic Model

For the heat conduction problem through a rarefied gas between the heated shell and confining (cold) cylinder, the nonlinear Shakhov model kinetic equation is solved numerically and compared with first- and second-order temperature-jump models. The nonlinear Shakhov model kinetic equation is obtained by replacing the problematic collision term of the Boltzmann equation by a simpler collision model (Chu, 1965; Shakhov, 1968a). The Shakhov model is generally accepted to be more accurate for flows associated with heat transfer compared to the BGK (Bhatnagar, Gross and Krook) model, since the BGK model gives an incorrect Prandtl number equal to unity (i.e. Pr=1) instead of Pr=2/3 for monatomic gases (Shakhov, 1968b; Graur and Polikarpov, 2009). In the present work, the Maxwell (specular/diffusive) boundary condition has been employed with the nonlinear Shakhov kinetic equation. It is important to note that the Boltzmann equation describes gas behaviour for all flow regimes and it is valid at all Knudsen numbers. The relation between the microscopic and macroscopic descriptions of gas is postulated as follows: all macroscopic quantities such as density, velocity and temperature are described in terms of the microscopic states, which are the solution of the Boltzmann equation. The state of the gas is given by the distribution function $f(\mathbf{x},\mathbf{v},t)$, where $\mathbf{x}\in\mathbb{R}^3$ is the position vector and $\mathbf{v}\in\mathbb{R}^3$ is the velocity vector of a molecule at time *t*. Once the distribution function is known, all the moments, for example gas density, pressure or heat flux can be computed.

The Shakhov model kinetic equation (i.e. the Boltzmann equation with the Shakhov collision model) can be written (at steady-state) in cylindrical coordinates (Graur and Polikarpov, 2009; Sharipov and Bertoldo, 2006; Pantazis and Valougeorgis, 2010) as

$$v_r\frac{\partial f}{\partial r}+\frac{v_\theta}{r}\frac{\partial f}{\partial \theta}+v_z\frac{\partial f}{\partial z}+\frac{v_\theta^2}{r}\frac{\partial f}{\partial v_r}-\frac{v_r v_\theta}{r}\frac{\partial f}{\partial v_\theta}=\frac{f^S-f}{\hat{\tau}} \qquad \textbf{(4.10)}$$

where $\mathbf{v_c} = (v_r, v_\theta, v_z)$ is the molecular velocity vector. By taking into account the axial symmetry of the shell problem in cylindrical coordinates (r, φ, z) in physical space, and considering the cylinders to be long enough to neglect the effects in the *z*-direction, the Shakhov model kinetic equation (i.e. the Boltzmann equation with the Shakhov collision model) in Eq. (4.10) can be written at steady-state as

$$v_p \cos\theta \frac{\partial f}{\partial r} - \frac{v_p \sin\theta}{r} \frac{\partial f}{\partial \theta} = \frac{(f^S - f)}{\bar{\tau}} \tag{4.11}$$

using $v_r = v_p \cos\theta$, $v_\theta = v_p \sin\theta$ with $v_p = \sqrt{v_r^2 + v_\varphi^2}$ and $\theta = \arctan(v_\varphi / v_r)$, where the distribution function does not depend on φ (i.e. $\partial f / \partial \varphi = 0$) due to the axial symmetry. The term on the right-hand side of equation (4.11) is the Shakhov collision model

$$\frac{(f^S - f)}{\bar{\tau}} \tag{4.12}$$

where $\bar{\tau} = \mu / p$ is the relaxation time, μ is the dynamic viscosity and p is the gas pressure, and

$$f^S(r, \mathbf{v_c}) = f^M(r, \mathbf{v_c}) \left[1 + \frac{4m}{15 n(r) (k_B T(r))^2} q(r) v_p \cos\theta \left(\frac{m \mathbf{v_c}^2}{2 k_B T(r)} - \frac{5}{2} \right) \right] \tag{4.13}$$

with

$$f^M(r, \mathbf{v_c}) = n(r) \left(\frac{m}{2\pi k_B T(r)} \right)^{3/2} \exp\left(- \frac{m \mathbf{v_c}^2}{2 k_B T(r)} \right) \tag{4.14}$$

where $\mathbf{v_c}$ is the molecular velocity vector, r is the radial distance, f^M is the local Maxwellian distribution, m is the molecular mass, k_B is the Boltzmann constant, $q(r)$ is the heat flux profile in the radial direction, and $n(r)$ and $T(r)$ are the macroscopic number density and temperature profiles, respectively and ideal gas law $p = n k_B T$ holds.

The unknown distribution function, *f*, in equation (4.11) depends on four variables (three velocity components and the radial distance). Collisions occur in this four dimensional phase space. But, the dependence of the distribution function on the velocity in the *z*-direction can be eliminated using a projection procedure. The reduced distribution functions ϕ and ψ are introduced (Zhuk et al., 1973) as

$$\phi(r, v_p, \theta) = \int f(r, \mathbf{v_c}) dv_z \text{ and } \psi(r, v_p, \theta) = \int f(r, \mathbf{v_c}) v_z^2 dv_z \quad \textbf{(4.15)}$$

The dimensionless variables in the present study are specified as

$$\begin{aligned} &\hat{r} = \frac{r}{R_2}, \quad \hat{T} = \frac{T}{T_2}, \quad \hat{\mathbf{v}} = \frac{\mathbf{v}}{v_0}, \quad \hat{n} = \frac{n}{n_0}, \quad \hat{p} = \frac{p}{p_2}, \\ &\hat{\mu} = \frac{\mu}{\mu_2} = \hat{T}^{\omega}, \quad \hat{f} = \frac{f v_0^2}{n_0}, \quad \hat{q} = \frac{2}{n_0 m v_0^2} q \end{aligned} \quad \textbf{(4.16)}$$

where $v_0 = \sqrt{2k_B T_2 / m}$ is the most probable molecular velocity at T_2 and n_0 is the average numerical density, which is

$$n_0 = \frac{2}{R_2^2 - R_1^2} \int_{R_1}^{R_2} n(r) r dr \quad \textbf{(4.17)}$$

The rarefaction parameter is defined as $\delta = R_2 p_2 / (\mu_2 v_0)$ where μ_0 is the dynamic viscosity at T_2. Using relations in (4.16) and (4.17), the rarefaction parameter can be related to the Knudsen number as $\delta = \sqrt{\pi} R_2 / (2Kn(R_2 - R_1))$, where the rarefaction parameter is inversely proportional to the Knudsen number.

Multiplying equation (4.11) by 1 and v_z^2, and integrating over v_z according to the relations in (4.17), two reduced kinetic equations are obtained in terms of the reduced distribution functions as

$$\hat{v}_p \cos\theta \frac{\partial \phi}{\partial \hat{r}} - \frac{\hat{v}_p \sin\theta}{\hat{r}} \frac{\partial \phi}{\partial \theta} = \delta \hat{n} \hat{T}^{1-\omega} (\phi^S - \phi) \quad \textbf{(4.18)}$$

$$\hat{v}_p \cos\theta \frac{\partial \psi}{\partial \hat{r}} - \frac{\hat{v}_p \sin\theta}{\hat{r}} \frac{\partial \psi}{\partial \theta} = \delta \hat{n} \hat{T}^{1-\omega} (\psi^S - \psi) \quad \textbf{(4.19)}$$

where

$$\phi^S = \phi^M \left[1 + \frac{4}{15} \frac{1}{\hat{n} \hat{T}^2} q(\hat{r}) \hat{v}_p \cos\theta \left(\frac{\hat{v}_p^2}{\hat{T}} - 2 \right) \right] \quad \textbf{(4.20)}$$

$$\psi^S = \psi^M \left[1 + \frac{4}{15} \frac{1}{\hat{n}\hat{T}^2} q(\hat{r}) \hat{v}_p \cos\theta \left(\frac{\hat{v}_p^2}{\hat{T}} - 1 \right) \right] \tag{4.21}$$

with

$$\phi^M = \frac{\hat{n}}{\pi \hat{T}} \exp\left(-\frac{\hat{v}_p^2}{\hat{T}} \right), \quad \psi^M = \frac{\hat{T}}{2} \phi^M, \quad \text{and} \quad \hat{v}_p^2 = \hat{v}_r^2 + \hat{v}_\theta^2 \tag{4.22}$$

The macroscopic quantities can be found in terms of the reduced distribution functions, ϕ and ψ, (Graur and Polikarpov, 2009; Sharipov and Bertoldo, 2006; Pantazis and Valougeorgis, 2010) as

$$\hat{n}(\hat{r}) = \int_0^{2\pi} \int_0^{\infty} \phi \hat{v}_p d\hat{v}_p d\theta \tag{4.23}$$

$$\hat{T}(\hat{r}) = \frac{2}{3\hat{n}(\hat{r})} \int_0^{2\pi} \int_0^{\infty} (\hat{v}_p^2 \phi + \psi) \hat{v}_p d\hat{v}_p d\theta \tag{4.24}$$

$$\hat{q}(\hat{r}) = \frac{2}{3\hat{n}(\hat{r})} \int_0^{2\pi} \int_0^{\infty} (\hat{v}_p^2 \phi + \psi) \hat{v}_r \hat{v}_p d\hat{v}_p d\theta \tag{4.25}$$

with the equation of state $p = nk_B T$.

The present study implements the Maxwell (specular/diffusive) gas-wall interaction model. In the Maxwell model, a proportion of the molecules, α, are reflected diffusively from the surface while the remaining proportion, $1-\alpha$, are reflected specularly from the surface. The specular reflection model is straightforward. When a molecule strikes a wall, the normal velocity component of the molecule is simply reversed and directed back into the flow domain; the other velocity components remain unchanged. In other words, the molecules bounce off the wall with the same velocity distribution except their reversed normal velocity components, while their other velocity components remain unchanged. For the diffuse reflection, the reflected tangential velocity of the molecule is considered to be uncorrelated with its impinging velocity and the molecules bounces off the surface according to the local Maxwell distribution. Therefore, for equation (4.18), the Maxwell boundary conditions at the inner and outer cylinders can be written as

$$\phi(r_1,\hat{v}_p,\theta)=(1-\alpha)\phi(r_1,\hat{v}_p,\pi-\theta)+\alpha\frac{n_1}{\pi\hat{T}_1}\exp\left(-\frac{\hat{v}_p^2}{\hat{T}_1}\right),\qquad -\pi/2\le\theta\le\pi/2 \tag{4.26}$$

$$\phi(1,\hat{v}_p,\theta)=(1-\alpha)\phi(1,\hat{v}_p,\pi-\theta)+\alpha\frac{n_2}{\pi}\exp(-\hat{v}_p^2),\qquad \pi/2\le\theta\le 3\pi/2 \tag{4.27}$$

associated with impermeability assumption (Graur and Polikarpov, 2009):

$$n_1=2\sqrt{\frac{\pi}{\hat{T}_1}}\int_0^{\infty}\hat{v}_p^2 d\hat{v}_p\int_{-\pi/2}^{\pi/2}\phi\cos\theta d\theta\quad\text{and}\quad n_2=-2\sqrt{\pi}\int_0^{\infty}\hat{v}_p^2 d\hat{v}_p\int_{\pi/2}^{3\pi/2}\phi\cos\theta d\theta \tag{4.28}$$

where $0\le\alpha\le 1$ is the accommodation coefficient, $r_1=R_1/R_2$ is the ratio between cylinder radii and $\hat{T}_1=T_1/T_2$ is the ratio between the inner and outer cylinder temperatures. The boundary conditions for equation (4.19) can be written in a very similar manner. The accommodation coefficient, α, is specified as unity (i.e. $\alpha=1.0$), and therefore only fully diffusive reflections are considered.

The heat transfer problem under consideration is solved using a computational scheme that discretizes equation (4.18) (and equation (4.19) in a similar manner) into

$$v_{p_k}\cos\theta_m\frac{\phi^j_{i,k,m}-\phi^j_{i-\beta,k,m}}{\beta\Delta\hat{r}}-v_{p_k}\frac{\sin\theta_m}{\hat{r}_i}\frac{\phi^j_{i,k,m}-\phi^j_{i,k,m-1}}{\Delta\theta}=$$
$$\delta\hat{n}_i^{j-1}(\hat{T}_i^{1-\omega})^{j-1}((\phi^S_{i,k,m})^{j-1}-\phi^j_{i,k,m}) \tag{4.29}$$

where *i* and *m* are the indices in the *r* and θ directions, respectively, *j* is the iteration index, $\beta=sign(\cos\theta_m)$ is the sign of $\cos\theta_m$; and *k* is the index for the Gauss quadrature points. In the present work, the annular clearance between the cylinders $[R_1/R_2,1]$ and the angular period $[0,\pi]$ are divided into 100 equal intervals. For the velocity space, the magnitudes of the molecular velocity, c_{p_k}, are mapped onto 20 Gauss quadrature points with their associated weights. Integrals in (4.23)-(4.25) for calculating the macroscopic quantities are obtained using the Gauss quadrature rule at each iteration. When the difference between macroscopic temperatures of successive iterations is smaller than a certain tolerance value, the convergence criterion is assumed to be fulfilled.

4.2 Results and Discussions

The effect of the Knudsen number on the temperature jumps over the concave and convex surfaces of the heated cylindrical shell are demonstrated in Figure 4.1. The temperature jumps are obtained from first- and second-order jump models and the nonlinear Shakhov model solution. Figure 4.1 presents the results in terms of the Knudsen number where the corresponding rarefaction parameter can be identified using the formula $\delta = \sqrt{\pi} R_2 / (2Kn(R_2 - R_1))$. According to this formulation, the rarefaction parameter is $\delta_{convex} = \sqrt{\pi} R_2 / (2Kn(R_2 - R_S))$ on the convex side, whilst it is $\delta_{concave} = \sqrt{\pi} R_S / (2Kn(R_S - R_1))$ on the concave side of the shell, where R_S the radius of the shell. Therefore, the rarefaction parameter is slightly higher (i.e. Kn is slightly lower) on the convex side of the shell; in fact, this supports our important conclusions about the significant effects of curvature.

In Figure 4.1, the concave and convex sides of the shell have the same surface area and same degree of curvature. The results remarkably show that the degree of temperature jump over a convex surface is markedly larger than that over a concave surface. Moreover, the jump models predict the amount of temperature jump relatively well up to Kn=0.3. However, beyond Kn=0.3, the predictions of the temperature-jump models start to deviate from the nonlinear Shakhov model solution. Figure 4.1 also shows that the second order jump solution is slightly in better agreement with the solution of nonlinear Shakhov model equation compared to the first-order solution in predicting the amount of temperature jump over the shell.

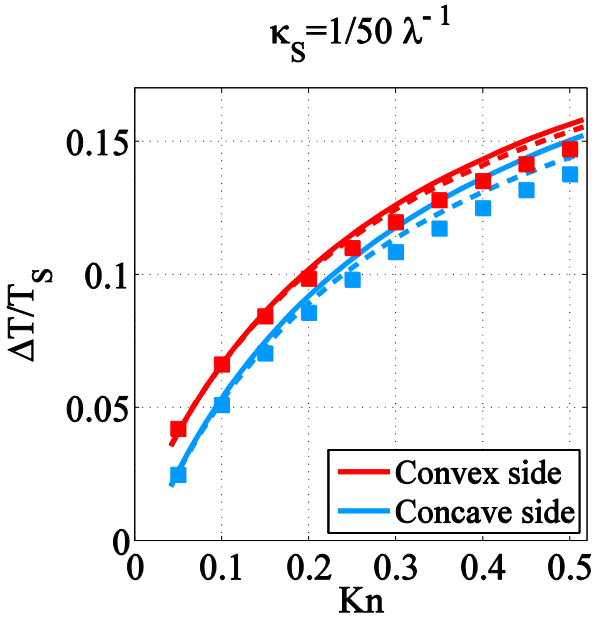

Figure 4.1: Temperature jumps over the concave and convex surfaces of a heated cylindrical shell against the Knudsen number. The red and blue curves illustrate temperature jumps over the convex and concave sides of the shell, respectively. The solid and dashed curves are the first- and second-order temperature-jump solutions, respectively. The square symbols illustrate the temperature jumps obtained from the solution of nonlinear Shakhov model kinetic equation. The shell curvature is $\kappa_S = 1/50\lambda^{-1}$ (i.e. the shell radius is $R_S = 50\lambda$).

Figure 4.2 shows that the DSMC data and the nonlinear Shakhov model solution are in excellent agreement. On the other hand, the accuracy of temperature-jump models deteriorates when the cylinder surface is cooler than the surrounding gas. This has been reported before for the planar heat conduction problem by Pan et al. (2002) when trying to determine the temperature-jump coefficient of a first-order temperature-jump boundary condition. Using the DSMC method, Pan et al. (2002) deduced different coefficients for the heat flow from a hot gas to a colder wall compared to the heat flow from a hot wall to a colder gas.

The magnitudes of the heat fluxes over the concave and convex surfaces of the shell are demonstrated in Figure 4.3. The profiles are obtained from the solution of the nonlinear Shakhov model kinetic equation. The shell curvature is $\kappa_S = 1/6\lambda^{-1}$ (i.e. the shell radius is $R_S = 6\lambda$). The results remarkably show the dramatic effect of the surface shape on the heat flux; the heat flux is significantly higher over the convex surface compared to the concave surface of the shell.

The variation of the normalized heat fluxes over the concave and convex surfaces are shown in Figure 4.4 for increasing values of curvature of the shell. The heat fluxes are obtained from the first-order temperature-jump model and normalized by the heat flux of the continuum regime as obtained in equation (4.9). For Knudsen numbers of 0.05 and 0.1, the first and second-order order jump solutions are expected to be very close to each other. Figure 4.4 shows that, as the curvature of the shell increases, the heat fluxes over the concave and convex surfaces of the shell start to show significant differences. It can be seen that the heat flux over the concave side becomes considerably lower than the heat flux over the convex side of the shell, beyond a certain curvature value depending on the Knudsen number.

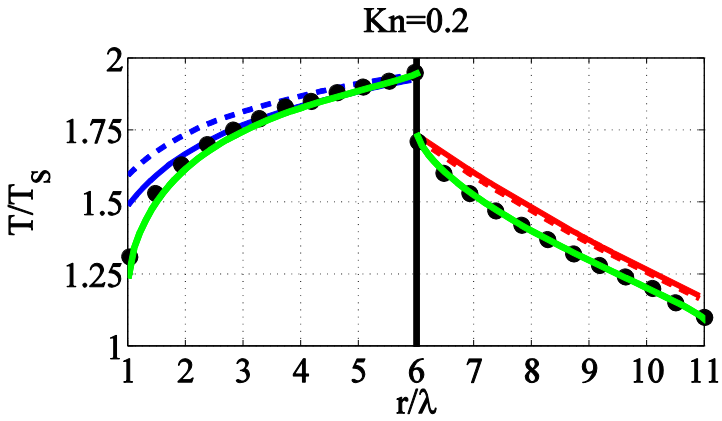

Figure 4.2: Temperature profiles over the concave and convex surfaces of the heated cylindrical shell. The profiles on the left- and right-hand sides of the shell are created by the heated concave and convex shell surfaces, respectively. The red and blue curves illustrate the temperature profiles obtained from the jump models over the convex and concave sides of the shell, respectively. The solid and dashed curves are the first- and second-order temperature-jump solutions, respectively. The green curves illustrate the temperature profiles obtained from the solution of nonlinear Shakhov model kinetic equation. The black dots are the DSMC data.

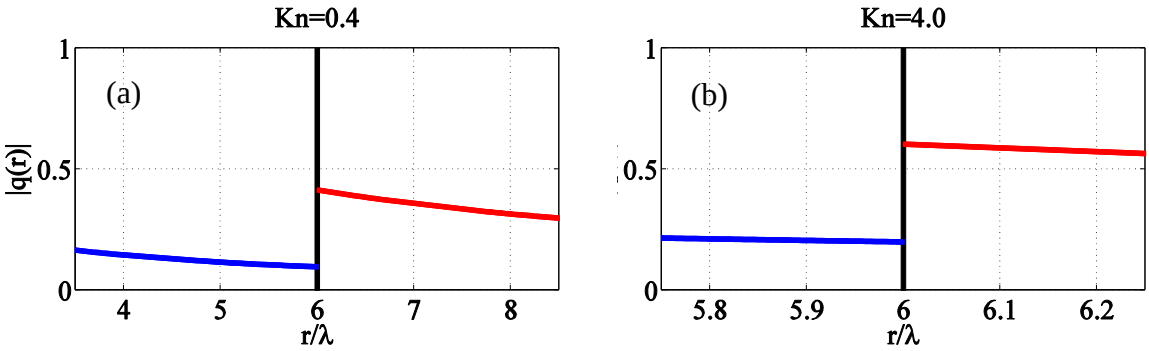

Figure 4.3: Magnitudes of the heat fluxes in the radial direction over the concave and convex surfaces of the shell. The profiles are obtained from the solution of the nonlinear Shakhov model kinetic equation. (a) Kn=0.4, (b) Kn=4.0.

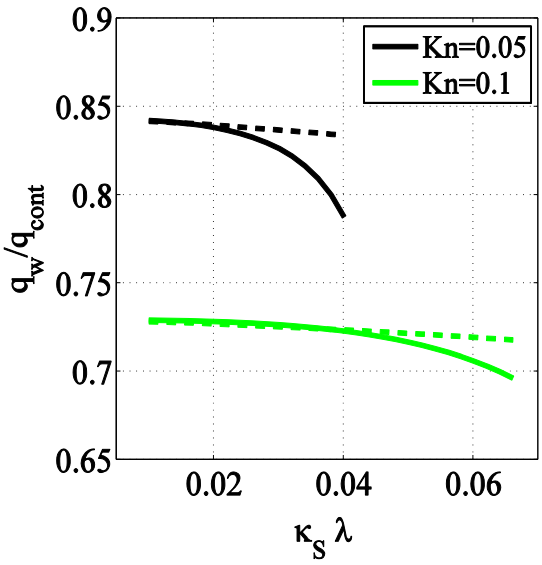

Figure 4.4: Normalized heat fluxes at the shell surface predicted by the first-order temperature-jump model against the curvature of the shell. The dashed and solid curves are the heat fluxes over the convex and concave surfaces of the shell, respectively, and q_{cont} is the heat flux in the continuum regime in the limit of $\mathrm{Kn} \to 0$.

5. THE STOKES EQUATIONS WITH SLIP BOUNDARY CONDITION

Gas microflows involve gas motion over or within microdevices whose characteristic length scale is less than 100 micrometers. The transport properties of microflows depend on the flow regime characterised by the Knudsen number (Kn), which is the ratio of the molecular mean free path to the characteristic length. The Knudsen number typically high (i.e. Kn>0.1) and increases with smaller length scale. The microflow properties are significantly different from macroflows and classical fluid mechanics models are unable to predict real flow behaviour.

Within microdevices, the surface-to-volume ratio is high, and gas-surface interactions and temperature jump conditions at the boundary have to be taken into account. In gas microflows, the characteristic length is very small and therefore rarefaction effects are important due to the high Knudsen number. Even under atmospheric conditions Kn is large with decreasing characteristic length. The Knudsen number is

$$Kn = \frac{\lambda}{L} \tag{5.1}$$

where λ is the mean free path and L is the characteristic length of the fluid domain. By incorporating the hard sphere intermolecular model (described in Chapter 2), the mean free path can be defined through the Chapman-Enskog theory by Chapman and Cowling (1970) as $\lambda = 16/5\,\nu(2\pi\mathcal{R}T)^{-1/2}$ where ν is the kinematic viscosity, ρ is the density, $\mathcal{R}$ is the specific gas constant and T is the temperature. When the factor 16/5(=3.2) is replaced by π, it corresponds to the viscous mean free path definition provided by Maxwell (1879). The Knudsen number is, in fact, can be considered as a scale parameter when the mean free path is kept constant and it monotonically increases with the surface-to-volume ratio. The Knudsen number is used for classifying flow regimes and therefore it is important to develop the appropriate mathematical model.

The classification of the flow regimes based on magnitude of the local Knudsen number was proposed by Schaaf and Chambre (1961). The magnitude of *Kn* not only determines the degree of rarefaction but also determines the degree of validity of the continuum model. These flow regimes are determined empirically and depend on the particular flow geometry (Barber and Emerson, 2006).

- For $\mathrm{Kn} < 10^{-3}$, the continuum assumption is valid and Navier-Stokes equations with no-slip velocity boundary condition model the flow phenomena.
- In the range, $10^{-3} < \mathrm{Kn} < 10^{-1}$, which is called *slip flow regime,* Navier-Stokes equations are still valid but the no-slip boundary condition is no longer valid. Therefore, gas-surface interactions must be taken into account using the slip models.
- In the range, $10^{-1} < \mathrm{Kn} < 10$, which is called *transition flow regime,* the continuum assumption of Navier-Stokes equations start to break down and kinetic models must be used.

Finally, for $\mathrm{Kn} > 10$, which is called *free-molecular flow regime,* mean free path λ is greater than characteristic length enough to neglect intermolecular collisions.

5.1 Derivation of the Navier-Stokes Equations

The Navier-Stokes equations and the assumptions made in their derivation are important to understand the limiting conditions of the Navier-Stokes equations. The Navier-Stokes equations are derived by the conservation laws of mass, momentum and energy under the continuum assumption (White, 1991; Richardson, 1989; Cengel, 2006). The continuum assumption assumes that properties such as density and bulk velocity can be defined uniformly over (fluid) volume elements using differential calculus.

In a control volume V , total mass can be written as

$$\int_V \rho dV \qquad \textbf{(5.2)}$$

Since rate of change of the total mass within a control volume is equal to the mass flow rate in through the surface (of the volume): Eq. (5.2) can be related as

$$\frac{\partial}{\partial t}\int_V \rho dV = -\int_S \rho \mathbf{u}\cdot\mathbf{n} dS \tag{5.3}$$

where $\mathbf{u}\in\mathbb{R}^3$ is the velocity, $\mathbf{n}\in\mathbb{R}^3$ is the outward unit normal vector from the boundary ∂V, $S\in\mathbb{R}^2$ is the surface of the control volume V and $\rho\mathbf{u}$ is the mass flow rate. Thus, the mass flow rate depends on the type of the gas. Using the divergence theorem, Eq. (5.3) becomes

$$\frac{\partial}{\partial t}\int_V \rho dV = -\int_V \nabla\cdot(\rho\mathbf{u}) dV \tag{5.4}$$

From Eq. (5.4), we obtain

$$\int_V \left[\frac{\partial\rho}{\partial t} + \nabla\cdot(\rho\mathbf{u})\right] dV = 0 \tag{5.5}$$

Equation (5.5) is satisfied if the following expression holds:

$$\frac{\partial\rho}{\partial t} + \nabla\cdot(\rho\mathbf{u}) = 0 \tag{5.6}$$

which is called the *continuity equation*.

Using the equality $\nabla\cdot(\rho\mathbf{u}) = \mathbf{u}\cdot\nabla\rho + \rho\nabla\cdot\mathbf{u}$, Eq. (5.6) can be written as

$$\frac{D\rho}{Dt} + \rho\nabla\cdot\mathbf{u} = 0 \tag{5.7}$$

where $D/Dt = \partial/\partial t + \mathbf{u}\cdot\nabla$ is named as the material derivative operator.

On the other hand, the conservation of the (linear) momentum is based on the Newton's second law, which states that net force acting on the control volume is equal to the mass times the acceleration of fluid element within control volume (Cengel, 2006). Therefore conservation of momentum actually is equilibrium of the forces, which can be framed as

$$[\text{Net Force}] = \begin{bmatrix}\text{Net rate of change of}\\ \text{the momentum}\end{bmatrix} = \begin{bmatrix}\text{Net momentum flux}\\ \text{in through the surface}\end{bmatrix}$$

In other words, rate of change of the momentum (time derivative of momentum) within control volume is equal to net force acting on control volume and can be described as follows:

$$\underbrace{\left[\begin{array}{l}\text{Net change of}\\ \text{the momentum}\\ \text{within control}\\ \text{volume}\end{array}\right]}_{F_{Net}} = \underbrace{\left[\begin{array}{l}\text{Momentum flux}\\ \text{in through}\\ \text{the surface}\end{array}\right]}_{F_u} + \underbrace{\left[\begin{array}{l}\text{Surface force}\\ \text{(shear stress)}\end{array}\right]}_{F_S} +$$

$$\underbrace{\left[\begin{array}{l}\text{Body forces}\\ \text{(gravitational}\\ \text{force)}\end{array}\right]}_{F_B} + \underbrace{[\text{External Forces}]}_{F_E}$$

We can calculate each term above separately. Momentum flux into the control volume, which is always normal to the unit surface unit area, can be written as $\rho\mathbf{u}(\mathbf{u}\cdot(-\mathbf{n}))$. Then, the total momentum flux can be written as

$$F_u = -\int_S \rho\mathbf{u}(\mathbf{u}\cdot\mathbf{n})dS \qquad \textbf{(5.8)}$$

Let $\boldsymbol{\zeta}_\mathbf{i}$ is the surface force at each point and the stress force can be written as $\int_S \boldsymbol{\zeta}_\mathbf{i} dS$.

Using Cauchy's stress theorem, which states that there is a tensor field such that $\boldsymbol{\zeta} = \mathbf{n}\cdot\tau$, where τ is the stress tensor (which is independent of orientation) (Richardson, 1989), we can write

$$F_S = \int_S \boldsymbol{\zeta}_\mathbf{i} dS = \int_S \mathbf{n}\cdot\tau dS \qquad \textbf{(5.9)}$$

Using the body force, $\rho\mathbf{g}$, and the external force, **X**, we can write net forces over the whole domain as

$$F_B = \int_V \rho\mathbf{g}dV \qquad \textbf{(5.10)}$$

$$F_E = \int_V \mathbf{X}dV \qquad \textbf{(5.11)}$$

Using equations (5.8)-(5.11), conservation of momentum is written as

$$F_{Net} = \frac{\partial}{\partial t}\int_V \rho\mathbf{u}dV = -\int_S \rho\mathbf{u}(\mathbf{u}\cdot\mathbf{n})dS + \int_S \mathbf{n}\cdot\tau dS + \int_V \rho\mathbf{g}dV + \int_V \mathbf{X}dV = 0 \qquad \textbf{(5.12)}$$

Using the divergence theorem, we obtain from Eq. (5.12)

$$\frac{\partial}{\partial t}\int_V \rho\mathbf{u}dV + \int_V \nabla\cdot(\rho\mathbf{uu})dV - \int_V \nabla\cdot\tau dV - \int_V \rho\mathbf{g}dV = \int_V \mathbf{X}dV \qquad \textbf{(5.13)}$$

In the second integral of Eq. (13), the operator between two $\mathbf{u}$ is the standard multiplication operator (it is "put together operator" for vectors) and accordingly using the relation $\nabla\cdot(\mathbf{v_1}\mathbf{v}_2) = \mathbf{v_1}\cdot\nabla\mathbf{v}_2 + \mathbf{v}_2\nabla\cdot\mathbf{v_1}$, for any two arbitrary vectors $\mathbf{v_1}, \mathbf{v_2} \in \mathbb{R}^3$, we obtain

$$\nabla\cdot(\rho\mathbf{uu}) = \rho\mathbf{u}\cdot\nabla\mathbf{u} + \mathbf{u}\nabla\cdot(\rho\mathbf{u}) \qquad \textbf{(5.14)}$$

From Eqs. (5.13) and (5.14) by neglecting body force, we obtain

$$\int_V \left[\frac{\partial}{\partial t}\rho\mathbf{u} + \rho\mathbf{u}\cdot\nabla\mathbf{u} + \mathbf{u}\nabla\cdot(\rho\mathbf{u}) - \nabla\cdot\tau\right]dV = \int_V \mathbf{X}dV \qquad \textbf{(5.15)}$$

Using the conservation of mass equation (i.e. continuity equation) in Eq. (5.6), Eq. (5.15) is satisfied if the following expression holds:

$$\rho\frac{\partial\mathbf{u}}{\partial t} + \rho\mathbf{u}\cdot\nabla\mathbf{u} - \nabla\cdot\tau = \mathbf{X} \qquad \textbf{(5.16)}$$

which is the *conservation of momentum equation*. In Eq. (5.16), the most ambiguous term is stress term, $\nabla\cdot\tau$. For Newtonian fluids stress tensor τ is assumed to be linearly proportional to rate of strain. Shear stress consisting of the normal components (pressures) and the viscous shear stress tensor τ_v can be written as

$$\tau = -p\mathbf{I} + \tau_v, \quad \tau_v = \mu_1\left[\nabla\mathbf{u} + \nabla\mathbf{u}^T\right] + \mu_2(\nabla\cdot\mathbf{u})\mathbf{I} \qquad \textbf{(5.17)}$$

where *p* is the pressure and **I** is the unit tensor. In 1845, Stokes simply assumed for viscosity coefficients that $2\mu_1 + 3\mu_2 = 0$, which is called *Stokes hypothesis*. After one and a half century, there is still confusion on this assumption and we know that in general Stokes hypothesis is not true (Cengel, 2006).

First law of thermodynamics states the conservation of energy as

$$\begin{bmatrix}\text{Net change in total}\\ \text{energy of the system}\end{bmatrix} = \begin{bmatrix}\text{Heat added to}\\ \text{the system}\end{bmatrix} + \begin{bmatrix}\text{Work done on}\\ \text{the system}\end{bmatrix}$$

The conservation of energy in the absence of heat generation, chemical reactions and nuclear reactions can be written in terms of

$$\underbrace{\left[\begin{array}{l}\text{Rate of change}\\ \text{in total energy}\\ \text{within control}\\ \text{volume}\end{array}\right]}_{E_{Net}} = \underbrace{\left[\begin{array}{l}\text{Heat flux}\\ \text{in through}\\ \text{the surface}\end{array}\right]}_{Q} + \underbrace{\left[\begin{array}{l}\text{Heat flux conducted}\\ \text{by the surface}\end{array}\right]}_{Q_C} +$$

$$\underbrace{\left[\begin{array}{l}\text{Rate of doing work}\\ \text{by surface force}\end{array}\right]}_{E_S} + \underbrace{\left[\begin{array}{l}\text{Rate of doing work}\\ \text{by body forces}\end{array}\right]}_{E_B} +$$

$$\underbrace{\left[\begin{array}{l}\text{Rate of doing work}\\ \text{by external Forces}\end{array}\right]}_{E_E}$$

The total energy E on a fluid element can be written by calculating density times the internal specific energy *e* and the kinetic energy $1/2\rho\mathbf{u}\cdot\mathbf{u} = 1/2\rho|\mathbf{u}|^2$ as

$$E = \rho e + 1/2\rho|\mathbf{u}|^2 \qquad \textbf{(5.18)}$$

The rate of change in total energy within a control volume is equal to

$$E_{Net} = \frac{\partial}{\partial t}\int_V E\,dV \qquad \textbf{(5.19)}$$

The heat flux into the control volume across the unit surface area is written as

$$Q = -\int_S E(\mathbf{u}\cdot\mathbf{n})dS \qquad \textbf{(5.20)}$$

Using the Fourier's Law,

$$\mathbf{q} = -k\nabla T \qquad \textbf{(5.21)}$$

where *k* is the thermal conductivity and ∇T is the temperature gradient, the rate of heat flow (heat flux) into the control volume across the unit surface area, which is caused by the heat conduction between the fluid and surface, can be written as

$$Q_C = -\int_S \mathbf{q}\cdot\mathbf{n}dS \qquad \textbf{(5.22)}$$

The works done by the body forces (such as gravitational, electrical and electromagnetic forces) are neglected here due to the assumption of the small gravitational, electric, or magnetic effects.

The rate of doing work is simply inner product of the bulk velocity and the force acting on the fluid element, therefore the rate of doing work by the surface and external forces can be given, respectively, as

$$E_s = \int_V \mathbf{u} \cdot \nabla \cdot \tau \, dV \tag{5.23}$$

$$E_E = \int_V \mathbf{u} \cdot \mathbf{X} dV \tag{5.24}$$

Hence, the conservation of energy is obtained as

$$\frac{\partial}{\partial t} \int_V E dV = -\int_S E(\mathbf{u} \cdot \mathbf{n}) dS - \int_S \mathbf{q} \cdot \mathbf{n} dS + \int_V \mathbf{u} \cdot \nabla \cdot \tau \, dV + \int_V \mathbf{u} \cdot \mathbf{X} dV \tag{5.25}$$

Using the divergence theorem, we obtain the *conservation of energy equation* as

$$\frac{\partial E}{\partial t} + \nabla \cdot (E\mathbf{u} - \mathbf{u} \cdot \tau + \mathbf{q}) = \mathbf{u} \cdot \mathbf{X} \tag{5.26}$$

The heat flux in Eq. (5.26) varies with the temperature gradient according to the Fourier's law (5.21), where the thermal conductivity is a function of temperature. It is important to note that, the Fourier's law starts to break down as the characteristic length shrinks down to the micro/nanoscale.

Using the equations of conservation of mass and momentum in Eqs. (5.6) and (5.16) and using Eq. (5.18), under the assumption of a constant density ρ, the energy equation (5.26) can be written as

$$\rho \frac{\partial e}{\partial t} + \rho \mathbf{u} \cdot \nabla e = -p \nabla \cdot \mathbf{u} - \nabla \cdot \mathbf{q} + \mu \Phi \tag{5.27}$$

where $\mu\Phi = \tau \cdot \nabla \mathbf{u}$ is the dissipation function. Here, the constant density assumption is consistent with the low-speed microflows. The dissipation function, Φ, and can be written in Cartesian coordinates (Schlichting, 1979) as

$$\begin{aligned} \Phi = 2\left[\left(\frac{\partial u}{\partial x}\right)^2 + \left(\frac{\partial v}{\partial y}\right)^2 + \left(\frac{\partial w}{\partial z}\right)^2\right] + \left(\frac{\partial v}{\partial x} + \frac{\partial u}{\partial y}\right)^2 + \\ \left(\frac{\partial w}{\partial y} + \frac{\partial v}{\partial z}\right)^2 + \left(\frac{\partial u}{\partial z} + \frac{\partial w}{\partial x}\right)^2 - \frac{2}{3}\left(\frac{\partial u}{\partial x} + \frac{\partial v}{\partial y} + \frac{\partial w}{\partial z}\right)^2 \end{aligned} \tag{5.28}$$

where *u*, *v* and *w* are the velocities in *x*-, *y*- and *z*-direction, respectively. Employing the ideal gas assumption, the variation in the internal energy can be given (White, 1991) as

$$de = C_v dT \tag{5.29}$$

where C_v is the specific heat. Then substituting Eqns. (5.29) and (5.21) into Eq. (5.26), it can be obtained

$$\rho C_v \left(\frac{\partial T}{\partial t} + \mathbf{u} \cdot \nabla T \right) = -p \nabla \cdot \mathbf{u} - \nabla \cdot \left(k \nabla T \right) + \mu \Phi \tag{5.30}$$

The equations (5.6), (5.16) and (5.30) construct the Navier-Stokes equations (under assumptions specified above), which is a system of nonlinear partial differential equations (PDEs) and its general solution is not available.

5.2 The Stokes Equations

The Stokes equations are the linearization of the Navier-Stokes equations for low-speed small scale flows. In microfluidic applications, fluid is generally desired to flow slowly in order to gain time, for example, used for efficient sensing. In low-speed gas flows, compressibility effects can be considered to be negligible, and then the Navier-Stokes equations (5.6) and (5.16) for incompressible (associated with constant density) and viscous flows are written respectively as

$$\nabla \cdot \mathbf{u} = 0 \tag{5.31}$$

$$\frac{\partial \mathbf{u}}{\partial t} + \mathbf{u} \cdot \nabla \mathbf{u} = -\frac{1}{\rho} \nabla p + \nu \nabla^2 \mathbf{u} \tag{5.32}$$

Using a reference velocity U_0 and a reference pressure p_0, flow variables can be nondimnesionalized as

$$\mathbf{x}^* = \frac{\mathbf{x}}{L}, \quad t^* = \frac{tU_0}{L}, \quad \mathbf{u}^* = \frac{\mathbf{u}}{U_0}, \quad p^* = \frac{(p - p_0)L}{\rho \nu U_0} \tag{5.33}$$

where $\mathbf{x}$ is the spatial vector, L is the characteristic length and ν is the kinematic viscosity. Then, equations (5.31) and (5.32) become

$$\nabla \cdot \mathbf{u}^* = 0 \tag{5.34}$$

$$\mathbf{u}^* \cdot \nabla^* \mathbf{u}^* = \frac{1}{\mathrm{Re}} \left[-\frac{\partial \mathbf{u}^*}{\partial t^*} - \nabla^* p^* + \nu \nabla^{*2} \mathbf{u}^* \right] \tag{5.35}$$

where Re is the Reynolds number

$$\mathrm{Re} = \frac{U_0 L}{\nu} \tag{5.36}$$

In micro gas flows, the Reynolds number is typically small (i.e. $\mathrm{Re} << 1$); and the nonlinear convective term in Eq. (5.35) can be eliminated. Therefore, we obtain the Stokes equations as

$$\nabla \cdot \mathbf{u}^* = 0 \tag{5.37}$$

$$\frac{\partial \mathbf{u}^*}{\partial t^*} + \nabla^* p^* = \nu \nabla^{*2} \mathbf{u}^* \tag{5.38}$$

The Stokes equations in (5.37) and (5.38) are linear approximation of the Navier-Stokes equations. These equations, which are defined in domain Ω of $\mathbb{R}^3$ and over an interval $t \in I$, must be accompanied by initial and boundary conditions. Typical boundary conditions are; the impermeability condition

$$\mathbf{u} \cdot \mathbf{n} = 0 \quad \text{on } \partial\Omega \tag{5.39}$$

where $\mathbf{n}$ stands for the outer normal vector; the no-slip boundary condition

$$\mathbf{u}_T = \mathbf{u} - (\mathbf{u} \cdot \mathbf{n})\mathbf{n} = 0 \quad \text{on } \partial\Omega \tag{5.40}$$

where $\mathbf{u}_T$ is the velocity in tangential plane; and the slip boundary condition, which assumes a non-zero relative tangential velocity respect to the contact surface,

$$\left|\mathbf{u}_T\right| = \left|\mathbf{u} - (\mathbf{u} \cdot \mathbf{n})\mathbf{n}\right| > 0 \quad \text{on } \partial\Omega \tag{5.41}$$

where $\left| \, . \, \right|$ is the Euclidean norm.

5.3 Slip Boundary Conditions

The transport properties of microflows depend on the flow regime characterised by the Knudsen number (Kn), which is the ratio of the molecular mean free path to the characteristic length. Even under atmospheric conditions, the Knudsen number can be large due to the small characteristic length. When the Knudsen number is in the

range between 0.01 and 0.1, which is referred as the *slip-flow regime*, the momentum and heat transfer properties of microflows differ from that of macroflows; the gas effectively slides over the surface and a temperature-jump exists between the surface and the gas. Moreover, the gas layer adjacent to the surface does not reach thermal equilibrium. In the slip-flow regime, the Navier-Stokes equations can capture the flow characteristics by means of the velocity-slip and temperature-jump boundary conditions. The Navier-Stokes equations with slip boundary conditions are called *slip models*. When the Knudsen number increases beyond 0.1, the Navier-Stokes equations start to break down and alternative models such as DSMC simulation must be used. Therefore, the Navier-Stokes equations and the assumptions made in their derivation are important to understand the limiting conditions of the Navier-Stokes equations.

In microflows, the roughness of the surface (asperities on the interaction surface) and the chemical attraction between gas and the surface molecules can have an important effect on the flow. Due to the high surface-to-volume ratio, employing the correct form of the velocity and the temperature boundary conditions is crucial.

In 1879 Maxwell, using conservation laws of mass and momentum over the surface, proposed a slip velocity boundary condition (Maxwell, 1879) as

$$u_{\text{slip}} = u_{\text{gas}} - u_{\text{wall}} = \pm \frac{(2-\sigma)}{\sigma} \frac{\lambda}{\mu} \tau \Big|_{\partial\Omega} + \frac{3}{4} \frac{(\gamma-1)}{\gamma} \frac{\text{Pr}}{p} \mathbf{q} \Big|_{\partial\Omega} \qquad \textbf{(5.42)}$$

where σ is the (tangential momentum) accommodation coefficient, $\partial\Omega$ is the boundary of the control volume, γ is the specific heat ratio, τ is the shear stress, Pr is the Prandtl number and q is the heat flux vector. The second term in Maxwell's slip condition (5.42) models an unusual phenomenon, *the thermal transpiration (or thermal creep)*, which is a movement of the gas molecules from cold to hot at the surface. In the isothermal case, Maxwell's slip velocity boundary condition becomes

$$u_{\text{slip}} = u_{\text{gas}} - u_{\text{wall}} = \pm \frac{(2-\sigma)}{\sigma} \frac{\lambda}{\mu} \tau \Big|_{\partial\Omega} \qquad \textbf{(5.43)}$$

Equation (5.43) states that the slip velocity is proportional to the shear stress and the slip length $(2-\sigma)/\sigma\lambda$ where λ is the mean free path; but inversely proportional to the viscosity, μ. The slip boundary condition (5.43) is characterized by the

accommodation coefficient, σ, which lies in the range $0 < \sigma \leq 1$. When $\sigma \to 0$, all incident molecules undergo a mirror-like reflection from the surface and this kind of reflection is called *specular reflection*. On the other hand, when $\sigma = 1$, the reflection is called *diffusive reflection*. The accommodation coefficient is never zero ($\sigma \neq 0$), where Equation (5.43) is not defined; because all surfaces, in reality, have some degree of surface roughness in small scale. It should be noted that complete specification of the accommodation coefficient σ is difficult since the accommodation coefficient is a function of molecular weight of the gas, energy of incoming molecules, the surface material, temperature of the gas, and condition of the surface (Barber and Emerson, 2006).

Myong (2004) proposed an interesting slip velocity condition based on Langmuir isotherm adsorption model, which models attachment of particles to a surface at constant temperature.

Various forms of second-order velocity-slip boundary condition have been proposed in the literature as shown in Tables 5.1. and 5.2. The use of higher-order slip boundary conditions is particularly important so as to extend the validity of first-order slip models beyond the conventionally-accepted upper limit, Kn=0.1. Slip models are particularly important due to their ease of implementation and the significantly reduced computational cost in comparison to kinetic-based approaches. For these reasons, second-order velocity-slip boundary conditions continue to attract significant attention due to their practical importance. Although higher-order boundary conditions can often extend the validity of slip models beyond Kn=0.1, most of the boundary conditions discussed in the literature can only be applied to planar surfaces.

The second-order slip boundary condition for planar surfaces that have met considerable success is in the form of

$$u_{slip} = \pm A_1 \lambda \left.\frac{\partial u}{\partial y}\right|_{wall} - A_2 \lambda^2 \left.\frac{\partial^2 u}{\partial y^2}\right|_{wall} \qquad \textbf{(5.44)}$$

where A_1 and A_2 are first- and second-order slip coefficients. Table 5.1 lists the values of the first- and second-order slip coefficients proposed in the literature.

Table 5.1: Theoretically proposed values of first and second-order slip coefficients (Barber and Emerson, 2006; Cao et al., 2009)

Author	A_1	A_2
Maxwell (1879)	1	0
Schamberg (1947)	1	1.309
Albertoni et al. (1963)	1.1466	0
Cercignani and Daneri (1963)	1.1466	0.9756
Deissler (1964)	1	1.125
Sreekanth (1969)	1.1466	0.14
Chapman and Cowling (1970)	1	0.5
Loyalka (1971)	0.7252	0
Loyalka et al. (1975)	1.0299	0
Hsia and Domoto (1983)	1	0.5
Mitsuya (1993)	1	0.2222
Pan et al. (1999)	1.125	0
Karniadakis et al. (2005)	1	-0.5
Hadjiconstantinou (2003)	1.11	0.61
Lockerby et al. (2004)	1	0.145-0.19
Wu (2008)	1.3333	0.25

Table 5.2: Expressions in front of first and second-order coefficients [Adopted from (Cao et al. 2009)].

Reference	A_1	A_2
Maxwell (1879)	$\frac{2-\sigma}{\sigma}$	0
Cercignani and Daneri (1963)	$\frac{2}{\sqrt{\pi}}\frac{2-\sigma}{\sigma}(1+0.1621\sigma)$	$\frac{2}{\pi}\left(\frac{1}{2}+C_1^2\right)$
Loyalka (1971)	$\frac{2-\sigma}{\sigma}\frac{\sqrt{\pi}}{2}(1-0.1871\sigma)$	0
Loyalka et al. (1975)	$\frac{2-\sigma}{\sigma}\frac{\sqrt{\pi}}{2}(1+0.1621\sigma)$	0
Lockerby et al. (2004)	$\frac{2-\sigma}{\sigma}$	$\frac{9}{4\pi}\frac{\mathrm{Pr}(\gamma-1)}{\gamma}$
Karniadakis et al. (2005)	$\frac{2-\sigma}{\sigma}$	$-\frac{2-\sigma}{2\sigma}$
Wu (2008) ($f=\min[1/Kn,1]$)	$\frac{2}{3}\left[\frac{3-\sigma f^3}{\sigma}-\frac{3}{2}\frac{(1-f^2)}{Kn}\right]$	$\frac{1}{4}\left[f^4+\frac{2}{Kn^2}(1-f^2)\right]$

Effective mean free path has been defined and used in some studies to improve the accuracy of the slip boundary conditions (Veijola et al., 1995; Schrag and Wachutka, 2002). However their reliability is questionable and their capability in nonplanar is unclear.

To analyze the flow over cylindrical surfaces, we use a generic second-order slip boundary condition and we express it by incorporating the Maxwell first-order slip boundary condition (Maxwell, 1879) as follows:

$$u_{slip}=u_{\mathrm{gas}}-u_{\mathrm{wall}}=\pm A_1\left(\frac{2-\sigma}{\sigma}\right)\frac{\lambda}{\mu}\tau\Big|_{\partial\Omega}-A_2\frac{\lambda^2}{\mu}\frac{\partial\tau}{\partial n}\Big|_{\partial\Omega} \qquad \textbf{(5.45)}$$

where $\lambda=(\mu/p)(\pi\bar{R}T/2)^{1/2}$ is the (viscous) mean free path, where p is the pressure, $\bar{R}$ is the specific gas constant and T is the temperature.

The first-order term of the slip boundary condition in Eq. (5.45) was originally derived by Maxwell (1879). Subsequently, a second-order slip boundary condition

for an arbitrary surface geometry was established by Sone (1969), Sone (2002 and Sone (2007) through a systematic asymptotic analysis of the Boltzmann equation and its boundary condition in half space for small Knudsen numbers. In the case of isothermal flow between two concentric cylinders, Sone's second-order slip boundary condition can be cast in the form of Eq. (5.45) but differs by the values of the first and second-order coefficients. The ± sign in front of the first-order term in Eq. (5.45) is determined by the direction of the normal vector pointing into the gas. In this particular confined geometry, the direction of the normal vector at the inner cylinder is positive (r-direction) while it is negative at the outer cylinder. The curvatures of the cylindrical surfaces also have opposite signs depending on whether the normal vector points towards the centre of curvature or not; the curvatures of the convex and concave surfaces are positive and negative, respectively. This makes the magnitude of the second-order slip coefficient, A_2, in Eq. (5.45) identical at both the convex and concave surfaces with a minus (-) sign in front. In addition, it should be noted that the generic second-order boundary condition shown in Eq. (5.45) reduces to a form of second-order slip boundary condition for planar surfaces which has met with considerable success up to a Knudsen number as high as 0.4 (Colin et al., 2004; Hadjiconstantinou, 2005a; Graur et al., 2009; Cercignani and Lorenzani, 2010; Perrier et al., 2011).

The Sone's second-order boundary condition, which was derived for an arbitrary surface geometry, can be recast, for the case of isothermal flow over cylindrical surfaces, in the form of Eq. (5.45). In the original form of Sone's second-order slip boundary condition, the curvature of the surface explicitly appears in the equation but when it is cast in the form of Eq. (5.45), the curvature effects in this confined cylindrical geometry are accounted for in the shear stress terms. This is not unexpected because in the leading order, Sone's boundary condition includes a shear stress term multiplied by a constant. Consequently, curvature effects are still implicitly present in Eq. (5.45), even though the first- and second-order coefficients do not explicitly depend on local curvatures.

The first-order slip coefficient has been the subject of numerous investigations (Kogan, 1969; Cercignani, 2000; Sone, 2002) and rigorous kinetic analyses have

suggested that the slip coefficient can be written as $A_1 = (2/\sqrt{\pi})\sigma_P$, where, for planar flows, σ_P can be written (Sharipov and Seleznev, 1998) as

$$\sigma_P \ \sigma = \left(\frac{2-\sigma}{\sigma} \right) \sigma_P(1) - 0.1211(1-\sigma) \ , \qquad \textbf{(5.46)}$$

where σ is the tangential momentum accommodation coefficient which varies from zero (for specular reflection) to unity (for fully diffuse molecular reflection). The value for $\sigma_P(1)$ (*i.e.* fully diffuse conditions) was initially obtained by Albertoni et al. (1963) using a BGK kinetic model, and was found to have a value of 1.01619. Subsequently, Loyalka et al. (1975) confirmed this value using "numerically exact" solutions of the BGK model. In practice, $\sigma_P(1)$ has been shown by Sharipov (2011) to lie in the range $0.9624 \le \sigma_P(1) \le 1.0185$. For perfect accommodation, Ohwada et al. (1989) have shown that the solution of the linearized Boltzmann equation for hard-sphere molecules leads to a value for $\sigma_P(1)$ of 0.9849.

In hydrodynamic approaches, the first-order slip coefficient is generally expressed in the form $A_1 = \alpha(2-\sigma)/\sigma$, where α plays a role that is analogous, but slightly different, to σ_P. In practice, α may depend on the accommodation coefficient, σ, but this relationship is not known for nonplanar flows. In the present paper, we have adopted the kinetic approach, given by Eq. (5.46), using the value of $\sigma_P(1)$ obtained by Ohwada et al. (1989). For fully-diffuse conditions, this leads to a value for the first-order slip coefficient of $A_1 = (2/\sqrt{\pi})0.9849 = 1.1113$.

The second-order slip coefficient has also been the subject of numerous investigations (Hadjiconstantinou, 2003; Colin et al., 2004; Hadjiconstantinou, 2005a; Graur et al., 2009; Cercignani and Lorenzani, 2010; Perrier et al., 2011). Unfortunately, a consensus has not been reached on the correct formulation of the second-order slip coefficient. Recently, Cercignani and Lorenzani (2010) conducted research on the analytical form of the second-order slip coefficient in the case of planar Poiseuille flow using an integro-differential form of the Boltzmann equation based on the true linearized collision operator. They reported that the second-order slip coefficient might depend on the accommodation coefficient. In addition, their

study pointed out that, by using appropriate slip coefficients, mass flow rates could be accurately predicted beyond Kn=0.4 (Cercignani and Lorenzani, 2010).

An alternative nonplanar second-order slip boundary condition for cylindrical surfaces has recently been developed by Taheri and Struchtrup (2009) using the regularized 13-moment (R13) equations. Their boundary condition for isothermal flow is written using the viscous mean free path definition as

$$u_{slip} = u_{\text{gas}} - u_{\text{wall}} = \pm \left(\frac{2-\sigma}{\sigma} \right) \lambda \left(\frac{\partial u}{\partial r} - \frac{u}{r} \right)\Bigg|_{wall} - \frac{2}{\pi} \lambda^2 \left(\frac{5}{6} \frac{\partial^2 u}{\partial r^2} - \frac{7}{6} \frac{1}{r} \frac{\partial u}{\partial r} + \frac{7}{6} \frac{u}{r^2} \right)\Bigg|_{wall} . \quad \textbf{(5.47)}$$

Taheri and Struchtrup (2009) have demonstrated that the slip solution of the Navier-Stokes equations using boundary condition (5.47) gives good agreement in the slip-flow regime with both DSMC data and the solution of the R13 equations for the case of rotating cylindrical Couette flow.

It is important to note that the Chapter 9 introduces corrections to the tangential velocities at both the concave and convex surfaces in order to accurately predict the degree of slip in the Navier-Stokes continuum formulation. These corrections have been developed through an extensive research on the relationship between the velocity defect (which is a deviation between the actual velocity profile and that predicted by the Navier-Stokes equations) and the shear stresses at the walls for wide range of Knudsen number, curvature and accommodation coefficient values. The boundary slips using these corrections are found to be in very good agreement with DSMC data for a range of accommodation coefficients and boundary curvatures.

6. THE EFFECTS OF CURVATURE ON THE ACCURACY OF SLIP MODELS

Slip boundary conditions that are higher-order in Knudsen number are crucially important to extend the validity of the Navier-Stokes equations into the early transition regime. While second-order slip boundary conditions have been extensively studied for planar geometries, relatively little research has been carried out into the accuracy of second-order slip boundary conditions for nonplanar flows. In the case of shear-driven rarefied gas flow between two oscillatory parallel plates, Hadjiconstantinou (2005b) has reported that the Navier-Stokes equations with second-order slip boundary conditions are in very good agreement with direct simulation Monte Carlo (DSMC) data up to a Knudsen number of 0.4. However, Emerson et al. (2007) have shown that first-order slip models for the flow between two concentric oscillating cylinders perform poorly compared to the equivalent planar case and have demonstrated that there are large discrepancies between the Navier-Stokes and DSMC solutions at Knudsen numbers beyond 0.1. In the present chapter, we investigate rarefied flows over nonplanar geometries using second-order slip models, and study the effects of curvature over both convex and concave surfaces. The investigation first considers an oscillating cylinder in an unbounded medium (i.e. the cylindrical equivalent of Stokes' second problem). We then consider confined flow within an annular gap between two concentric oscillating cylinders. The study demonstrates that the effects of the Knudsen layer cannot explain why slip models perform poorly for nonplanar flow cases in comparison to the equivalent planar case; nor can the presence of Knudsen layers explain why slip models show larger discrepancies over convex surfaces. We finally investigate the flow driven by an oscillating thin cylindrical shell positioned between two concentric cylinders and demonstrate the important role of the surface shape (i.e. concave/convex) by eliminating the influence of the surface area and curvature. The results provide evidence for the existence of the *S-layer* over a convex surface. The

S-layer is a thin sub-layer within the Knudsen layer and it significantly reduces the accuracy of slip models.

Micro-electro-mechanical systems (MEMS) sensors involving oscillatory components are commonly used as accelerometers and gyroscopes. These devices typically operate in a rarefied medium where the dynamic response of the gas plays an important role in damping the oscillations. Although many MEMS devices contain curved boundaries, surprisingly little research has been conducted on the flow behaviour associated with nonplanar surfaces. To understand the flow within oscillatory micro-devices, planar oscillatory Couette (i.e. shear-driven) flows have been extensively studied from the continuum to the free-molecular flow regime (Park et al., 2004; Hadjiconstantinou, 2005b; Haddad et al., 2005; Sharipov and Kalempa, 2007; Tang et al., 2008; Frangi et al., 2009; Doi, 2010; Gu and Emerson, 2011). Hadjiconstantinou (2005b) has reported that the Navier-Stokes equations with second-order slip boundary conditions are in very good agreement with direct simulation Monte Carlo data up to a Knudsen number, $Kn \approx 0.4$. However, in the case of nonplanar Couette flow between concentric cylinders, Emerson et al. (2007) have reported that the first-order slip solution starts to show significant discrepancies against the DSMC data above $Kn \approx 0.1$.

The transport properties of gas microflows depend on the flow regime as characterized by the Knudsen number, Kn, which is the ratio of the molecular mean free path to the characteristic length scale. When the Knudsen number increases beyond 0.1, the growing influence of the Knudsen layer is expected to have a critical influence on the flow behaviour. The Knudsen layer manifests itself as a significant velocity defect close to the wall, i.e. a deviation between the actual velocity profile and that predicted using the Navier-Stokes equations (Loyalka, 1975). The present study shows that particularly large velocity defects appear over convex surfaces in comparison to concave surfaces.

Two fundamental isothermal oscillatory Couette flows have been examined; namely (a) unconfined flow over an oscillating circular cylinder (i.e. the cylindrical equivalent to Stokes' second problem) and (b) confined flow between two concentric oscillating cylinders. The study demonstrates that curvature effects are more prominent at high Knudsen number. In addition, the study considers a flow driven by a thin oscillatory cylindrical shell in order to highlight the effects of different surface

shapes (i.e. concave/convex). The results reveal that the S-layer, which is a layer over a convex surface and whose thickness is proportional to the curvature of the surface, plays a significant role on the flow behaviour.

6.1 Problem Description

Oscillatory Couette flows are characterized by the Knudsen number, Kn, and the Stokes number, β. The Knudsen number is defined as $\mathrm{Kn} = \lambda / L$ and the Stokes number is defined as $\beta = \sqrt{\omega L^2 / \nu}$ where λ is the mean free path, ω is the oscillatory frequency, ν is the kinematic viscosity and L is the characteristic length scale. Using a hard-sphere model for the intermolecular potential, the mean free path can be defined according to Chapman and Cowling (1970) as $\lambda = (\mu / p)\sqrt{\pi \mathcal{R} T / 2}$ where p is the pressure, $\mathcal{R}$ is the specific gas constant and T is the temperature. In the case of flow between two concentric cylinders, the characteristic length, L, can most conveniently be defined in terms of the annular clearance between the cylinders, i.e. $L = R_2 - R_1$. However, for the case of *unconfined* flow around an oscillating cylinder, it is more appropriate to define the characteristic length scale as $L = \sqrt{\nu / \omega}$. The curvature, κ, is defined as the inverse of the oscillating cylinder radius.

The incompressible Navier-Stokes equations for an oscillatory cylindrical Couette flow can be written in cylindrical-polar coordinates as

$$\frac{\partial u_\theta}{\partial t} = \nu \left[\frac{\partial^2 u_\theta}{\partial r^2} + \frac{\partial}{\partial r}\left(\frac{u_\theta}{r} \right) \right], \qquad \textbf{(6.1)}$$

where u_θ is the tangential velocity component, t is the time, and r is the radial distance. The oscillating cylinder is assumed to have a tangential velocity of $U \sin(\omega t)$, where U is the velocity amplitude of the oscillating cylinder. The inner and outer cylinders have radii, R_1 and R_2, respectively. Using the separation of variables technique, the general solution of Eq. (6.1) can be obtained as

$$u_\theta(r,t) = \mathrm{Im}\left\{ e^{i\omega t} \left[C I_1(z) + D K_1(z) \right] \right\}, \qquad \textbf{(6.2)}$$

where Im is the imaginary part, C and D are constants determined by the boundary conditions, I_1 and K_1 are the first-order modified Bessel functions of the first and second kind, respectively, and $z=(i+1)\sqrt{\omega/(2\nu)}\,r=\sqrt{i}\beta r/L$, where $i=\sqrt{-1}$.

6.1.1 Slip boundary conditions

Various forms of second-order velocity-slip boundary condition have been proposed in the literature as reviewed in Chapter 5. The use of higher-order slip boundary conditions is particularly important so as to extend the validity of first-order slip models beyond the conventionally-accepted upper limit, Kn=0.1. Slip models are particularly important due to their ease of implementation and the significantly reduced computational cost in comparison to kinetic-based approaches.

For nonplanar surfaces, we use a generic second-order velocity-slip boundary condition, which is introduced in Chapter 5, as

$$u_{slip}=u_{\text{gas}}-u_{\text{wall}}=\pm A_1\frac{\lambda}{\mu}\tau\bigg|_{wall}-A_2\frac{\lambda^2}{\mu}\frac{\partial\tau}{\partial n}\bigg|_{wall}, \tag{6.3}$$

where the subscripts "gas" and "wall" refer to the velocity of the gas and wall, respectively, A_1 and A_2 are the first and second-order slip coefficients, u is the tangential velocity component, μ is the dynamic viscosity, τ is the shear stress and $\partial/\partial n$ is the derivative in the direction normal to the surface.

The accuracy of the boundary condition in Eq. (6.3) has been investigated through comparing with the DSMC data; and also comparing with an alternative nonplanar second-order velocity-slip boundary condition which has recently been developed by Taheri and Struchtrup (2009) using the regularized 13-moment (R13) equations. Their boundary condition for isothermal flow is written using the viscous mean free path definition a

$$\begin{aligned}u_{slip}=u_{\text{gas}}-u_{\text{wall}}=&\pm\left(\frac{2-\sigma}{\sigma}\right)\lambda\left(\frac{\partial u_\theta}{\partial r}-\frac{u_\theta}{r}\right)\bigg|_{wall}\\&-\frac{2}{\pi}\lambda^2\left(\frac{5}{6}\frac{\partial^2 u_\theta}{\partial r^2}-\frac{7}{6}\frac{1}{r}\frac{\partial u_\theta}{\partial r}+\frac{7}{6}\frac{u_\theta}{r^2}\right)\bigg|_{wall}\end{aligned} \tag{6.4}$$

Taheri and Struchtrup (2009) have demonstrated that the slip solution of the Navier-Stokes equations using boundary condition (6.4) gives good agreement in the slip-flow regime with both DSMC data and the solution of the R13 equations for the case of rotating cylindrical Couette flow.

In the present study, the flow profiles have been obtained using both second-order boundary conditions, (6.3) and (6.4), for the fully-diffusive case (i.e. $\sigma = 1$). The first-order flow profiles can be obtained simply by defining the second-order slip coefficient in Eq. (6.3) to be zero, i.e. $A_2 = 0$. Following Hadjiconstantinou (2005b), the slip coefficients are specified as $A_1 = 1.11$ and $A_2 = 0.61$.

6.1.2 Direct simulation Monte Carlo simulations

The analytical slip solution for the flow between oscillating cylinders has been compared against DSMC results. The present study adopts the standard DSMC algorithm proposed by Bird (1994) with the exception of a small modification in the calculation of the maximum collision number in a cell, as described by Stefanov et al. (1998). Weighting factors for improving the particle number balance in the radial direction were not included in the present algorithm since the simulations did not consider large ratios of cylinder radii.

The simulations considered a hard-sphere model for argon and implemented isothermal fully diffusive reflections at the surfaces of both cylinders. The one-dimensional flow domain was discretized using 200 cells in the radial direction with each cell containing approximately 1000 simulation particles on average. The oscillating cylinder was assumed to have a velocity amplitude of 101 m/s, corresponding to an approximate Mach number of 0.3. The results from the DSMC simulations showed that, in all the cases considered, there was less than a 2% variation in density and temperature throughout the flow domain, suggesting that compressibility and thermal effects are not particularly important in this problem. In addition, the density and temperature variations were found to be less significant near an oscillatory convex surface compared with the variations near an oscillatory concave surface.

As discussed by Park et al. (2004), the choice of time step, Δt, has to take into account four different constraints. Firstly, the time step has to be significantly

smaller than the mean time between molecular collisions in order to ensure accurate simulations. Secondly, the simulation particles must not be allowed to move across more than one computational cell between consecutive time steps. Thirdly, the time step needs to be significantly smaller than the period of the oscillations i.e. $\Delta t \ll 2\pi/\omega$. Finally, as indicated by Park et al. (2004), the time step has to be smaller than the viscous diffusion time which implies that $\Delta t \ll L^2/\nu$. The time step has been chosen to satisfy all four constraints. The simulated time interval was selected so as to cover a sufficient number of oscillations in order to approach the limit-cycle oscillatory regime. In the present study, the simulations required a total time interval ranging from three to eight complete oscillation periods.

6.2. Results and Discussion

6.2.1 Stokes' second problem for nonplanar slip flow

The solution of the cylindrical form of Stokes' second problem, i.e. an oscillating cylinder in an unbounded medium is obtained using a velocity-slip boundary condition at the cylinder and a free boundary condition in the far-field (i.e. $u_\theta(t, r\to\infty)=0$). The solution must remain finite in the far-field and therefore the general solution shown in Eq. (6.2) needs to be rewritten as

$$u_\theta(r,t) = \mathrm{Im}\left\{e^{i\omega t} D K_1(z)\right\}. \qquad \textbf{(6.5)}$$

The constant, *D*, is obtained using both the generic second-order slip boundary condition (6.3) and Taheri and Struchtrup's second-order boundary condition (6.4), giving

$$D_{generic} = \frac{r_1^2}{\left(r_1^2 + A_2 \mathrm{Kn}^2 z_1^2\right) K_1(z_1) + \mathrm{Kn}\left(2A_2\mathrm{Kn} + A_1 r_1\right) z_1 K_2(z_1)}, \qquad \textbf{(6.6)}$$

and

$$D_{Tah\&Str} = \frac{3\pi r_1^2}{\left(3\pi r_1^2 + 5\mathrm{Kn}^2 z_1^2\right) K_1(z_1) + 3\mathrm{Kn}\left(4\mathrm{Kn} + \pi r_1\right) z_1 K_2(z_1)}, \qquad \textbf{(6.7)}$$

where $r_1 = R_1 / L = R_1\sqrt{\omega/\nu}$, A_1 and A_2 are the first and second-order slip coefficients, $K_1(\cdot)$ and $K_2(\cdot)$ are the first and second-order modified Bessel functions of the second kind, respectively, and $z_1 = \sqrt{i}r_1$.

One of the most important parameters in quantifying oscillatory shear driven flows is the rate at which the amplitude of the fluid oscillation decays with distance from the moving surface. This is normally expressed in terms of the thickness of the *Stokes' layer* which is the region where most of the oscillatory flow occurs. The thickness of the Stokes' layer, which is often referred to as the *penetration depth*, δ, is defined as the distance from the moving surface to the location where the amplitude of the fluid oscillations decays to 1% of the surface velocity. Before discussing the effects of curvature, it is informative to analyse the penetration depth for planar surfaces (i.e. in the limit of $R_1 \to \infty$).

Using the generic second-order boundary condition (6.3), the penetration depth for planar surfaces is obtained as

$$\delta = 6.5127\sqrt{\frac{\nu}{\omega}} - \frac{\sqrt{2}}{2}\sqrt{\frac{\nu}{\omega}}\ln\left(1+\sqrt{2}A_1\mathrm{Kn}+A_1^2\mathrm{Kn}^2+\sqrt{2}A_1A_2\mathrm{Kn}^3+A_2^2\mathrm{Kn}^4\right). \qquad \textbf{(6.8)}$$

Conversely, using Taheri and Struchtrup's second-order boundary condition (6.4) leads to

$$\begin{aligned}\delta = {} & 6.5127\sqrt{\frac{\nu}{\omega}} \\ & -\frac{\sqrt{2}}{2}\sqrt{\frac{\nu}{\omega}}\ln\left(1+\sqrt{2}\mathrm{Kn}+\mathrm{Kn}^2+1.1785\frac{2}{\pi}\mathrm{Kn}^3+0.6944\frac{4}{\pi^2}\mathrm{Kn}^4\right).\end{aligned} \qquad \textbf{(6.9)}$$

Equations (6.8) and (6.9) indicate that the second-order slip boundary conditions predict slightly smaller penetration depths compared to the first-order solution obtained with $A_2 = 0$.

The effects of curvature on the penetration depth are examined in Fig. 6.1 which shows the nondimensionalized velocity amplitude as a function of distance from the oscillating cylinder for different values of curvature (i.e. different values of the oscillating cylinder radius). The results show that changes in the velocity profile due to curvature effects are more prominent at higher Knudsen numbers. Moreover, the

velocity amplitudes in Fig. 6.1 show that the penetration depth decreases as the Knudsen number and the curvature (i.e. $\kappa = 1/R_1$) increase.

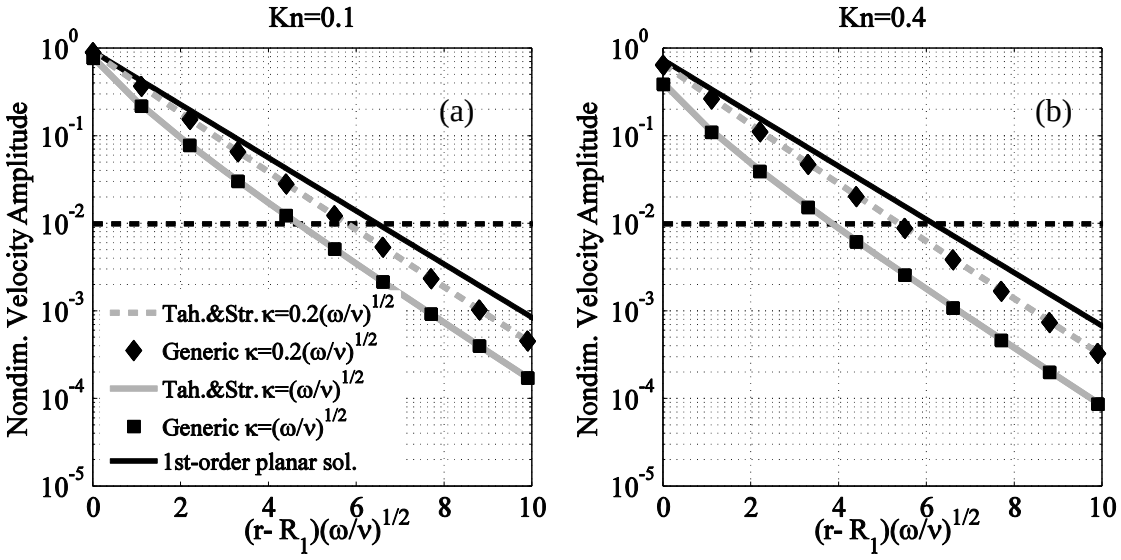

Figure 6.1: Comparison of nondimensionalized velocity amplitudes for an unconfined oscillating cylinder showing the effect of surface curvature. The Taheri and Struchtrup (Tah.&Str.), Eq. (6.4), and the generic boundary condition, Eq. (6.3), are employed. The radius of the inner cylinder is specified as $R_1 = \sqrt{\nu/\omega}$ (solid lines) and $R_1 = 5\sqrt{\nu/\omega}$ (dotted lines). The curvature (κ) is defined as the inverse of the radius of the oscillating cylinder, i.e. $\kappa = 1/R_1$. The solid black line depicts the first-order slip solution for the planar flow problem and the horizontal dashed lines indicate the 1% cut-off defining the penetration depth. (a) Kn=0.1 and (b) Kn=0.4.

6.2.2 Oscillatory rarefied cylindrical Couette flow

The effects of curvature have also been investigated for oscillatory Couette flow within an annular gap between two concentric cylinders. In the present study, two separate flow cases have been investigated, namely: (a) an oscillating inner cylinder and a stationary outer cylinder, and (b) an oscillating outer cylinder and a stationary inner cylinder. The slip-flow solutions for oscillatory cylindrical Couette flow have been obtained using the second-order boundary conditions in equations (6.3) and (6.4). Since the second-order analytical solutions are too lengthy to be presented here, we present the constants *C* and *D* of the general solution, Eq. (6.2), obtained using the first-order slip boundary condition (i.e. $A_2 = 0$). The general solution can be written as

$$C = \frac{r_1 U_1 Q_2 + r_2 U_2 Q_1}{P_1 Q_2 + P_2 Q_1} \quad \text{and} \quad D = \frac{r_1 U_1 P_2 - r_2 U_2 P_1}{P_1 Q_2 + P_2 Q_1}, \tag{6.10}$$

where $r_1 = R_1 / L$, $r_2 = R_2 / L$, U_1 and U_2 are the velocity amplitudes of the inner and outer cylinders, respectively, and

$$P_1 = r_1 I_1(z_1) - A_1 \mathrm{Kn}\, z_1 I_2(z_1), Q_1 = r_1 K_1(z_1) + A_1 \mathrm{Kn}\, z_1 K_2(z_1),$$

$$P_2 = r_2 I_1(z_2) + A_1 \mathrm{Kn}\, z_2 I_2(z_2),\ Q_2 = -r_2 K_1(z_2) + A_1 \mathrm{Kn}\, z_2 K_2(z_2);$$

$z_1 = \sqrt{i\beta} r_1$, $z_2 = \sqrt{i\beta} r_2$, and $I_2(\cdot)$ and $K_2(\cdot)$ are the second-order modified Bessel functions of the first and second kind, respectively.

In the case of nonplanar oscillatory Couette flow, Fig. 6.2 shows the significance of surface shape (i.e. convex/concave) on the inner and outer cylinders since the velocity profiles appear to be clearly different. It can be seen that the amount of slip over an oscillating inner cylinder (i.e. over an oscillating convex surface) is larger than that over an oscillating outer cylinder (i.e. a concave surface). Furthermore, in this flow case, Emerson et al. (2007) have shown that the first-order slip solution shows large discrepancies against DSMC data at Kn=0.5 and concluded that first-order models must be used with caution in the early transition regime (i.e. $0.1 \le \mathrm{Kn} \le 0.5$). As shown in Fig. 6.2, the present results indicate that there are still large discrepancies between the second-order slip solution and the DSMC data at Kn=0.4 for the case where the inner (convex) cylinder is oscillating. This contrasts with the planar oscillatory flow problem considered by Hadjiconstantinou (2005b) where the Navier-Stokes equations with second-order slip boundary conditions give very good agreement with direct simulation Monte Carlo data up to Kn≈0.4.

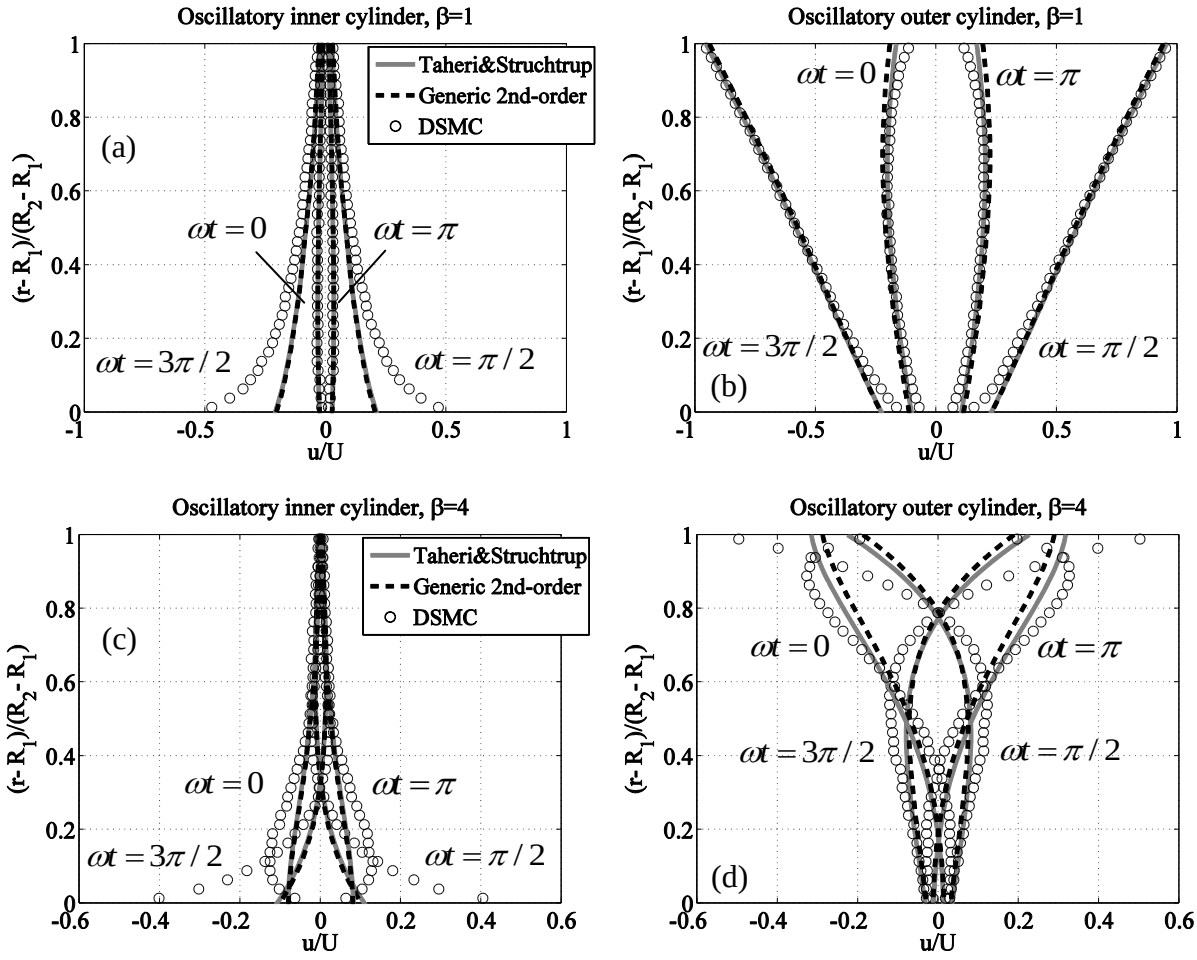

Figure 6.2: Comparison of dynamic velocity profiles for confined nonplanar oscillatory Couette flow at a Knudsen number of 0.4 for values of Stokes number (β) of 1 and 4. The ratio of the outer cylinder radius to the inner cylinder radius is specified as $R_2 / R_1 = 3$.

The flow rate discrepancies between the analytical slip solution and the DSMC data are presented in Fig. 6.3 for the case where the outer cylinder is oscillating and the inner cylinder is stationary, whilst Fig. 6.4 shows the flow rate discrepancies when the inner cylinder is oscillating and the outer cylinder is stationary. The velocity profiles are obtained using the second-order boundary conditions in equations (6.3) and (6.4), and the flow rates are calculated at the instant of maximum wall velocity (i.e. $\omega t = \pi / 2$) by integrating the velocity profiles across the annular clearance between the cylinders. The mass flow rate discrepancies (ε) are obtained as a percentage using the formula:

$$\varepsilon = \left(\left| \frac{\text{Mass flow rate predicted by the slip model}}{\text{Mass flow rate predicted by the DSMC data}} \right| - 1 \right) \times 100 . \qquad \textbf{(6.11)}$$

For a fixed Knudsen number, $\mathrm{Kn} = \lambda / (R_2 - R_1)$, the curvatures of both the inner and outer cylinders increase as the ratio between the cylinder radii (i.e. R_2 / R_1) increases. The velocity profiles obtained from both the DSMC and slip solutions show that the amount of slip over the oscillating convex surface increases with curvature. Conversely, the slip-velocity over the oscillating concave surface decreases as the curvature increases. This suggests that surface curvature has the opposite effect on the slip-velocity over concave and convex surfaces. A similar opposing effect on the slip lengths was predicted by Einzel et al. (1990) who developed a generalized slip-boundary condition for fluid flows over curved surfaces.

The results in Fig. 6.3 demonstrate that curvature does not have a significant effect on the flow rate discrepancies when the oscillatory flow is driven by the concave (outer) surface and show that second-order slip solutions are able to capture the flow rates within the annular clearance with reasonable accuracy (i.e. < 2.5% error) for Knudsen numbers up to 0.4. In contrast, Fig. 6.4 shows that the curvature of the convex surface has an important effect on the accuracy of slip models, with the flow rate discrepancies increasing significantly with curvature. Moreover, the flow rate discrepancies over a convex surface are considerably larger than the equivalent planar case. The results clearly illustrate the profound effect of the S-layer over a convex surface. The presence of the S-layer was first predicted by Sone (1973) and its thickness was estimated to be of the order of $\lambda^2\kappa$, where κ is the curvature of the convex surface. Although this implies that the S-layer is a thin sub-layer within the Knudsen layer when Kn<1, the results in Fig. 6.4 show that its influence on the flow behaviour can be very significant.

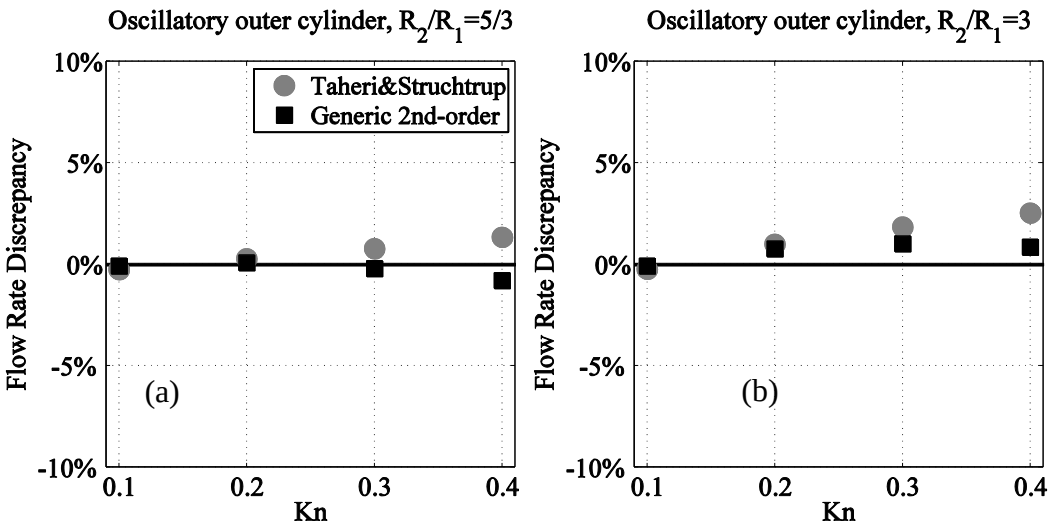

Figure 6.3: Flow rate discrepancies (ε) against Knudsen number at a Stokes number of $\beta = 1$ for the case when the outer cylinder is oscillating and the inner cylinder is stationary. The ratio of the outer cylinder radius to the inner cylinder radius is specified as: (a) $R_2 / R_1 = 5/3$ and (b) $R_2 / R_1 = 3$. The curvature increases with the ratio, R_2 / R_1. A negative discrepancy indicates that the slip model predicts a lower flow rate compared to the DSMC solution.

The presence of the S-layer was first predicted by Sone (1973) for the case of thermal creep flow around a circular cylinder using asymptotic analysis of the Boltzmann-Krook-Walender equation. Sone found that the nondimensional tangential velocity is affected by a term of the order of Kn^2 at the bottom of the Knudsen layer, and pointed out that the existence of the S-layer may well be a general feature of any flow over a convex surface. However, the effects of the S-layer were only analysed within this thin sub-layer and were assumed to vanish outside the S-layer. Later on, the presence of the S-layer was attributed to the discontinuity of the solution of the Boltzmann equation (i.e. discontinuity in the distribution function) over the convex surface (Sone and Takata, 1992). The discontinuity of the distribution function within the S-layer attracted further attention due to the possible error introduced by the accuracy of the numerical method near the discontinuity (Sugimoto and Sone, 1992; Sone and Sugimoto, 1993). The present study reveals that the S-layer can sometimes have a profound effect on the fluid behaviour that extends into the bulk of the fluid flow, well beyond the S-layer itself.

To further demonstrate the effect of the S-layer, Fig. 6.5 shows the velocity profiles when an infinitely thin cylindrical shell oscillates between two stationary cylinders. The oscillatory cylindrical shell is positioned in the middle of the annular gap and is

assumed to have a radius of 3.75λ, where λ is the mean free path. To achieve a Knudsen number of Kn=0.4, the annular clearances on both sides of the shell are specified as 2.5λ. This particular geometry ensures that the ratio of the outer and inner cylinder radii are $R_2 / R_1 = 3$ and $R_2 / R_1 = 5/3$ on either side of the shell, as considered in the previous example. The flows on the left- and right-hand side of the shell are driven by concave and convex surfaces, respectively. Both sides of the shell obviously have identical surface curvature and surface area, and any differences in the flow behaviour can be directly attributed to the surface shape.

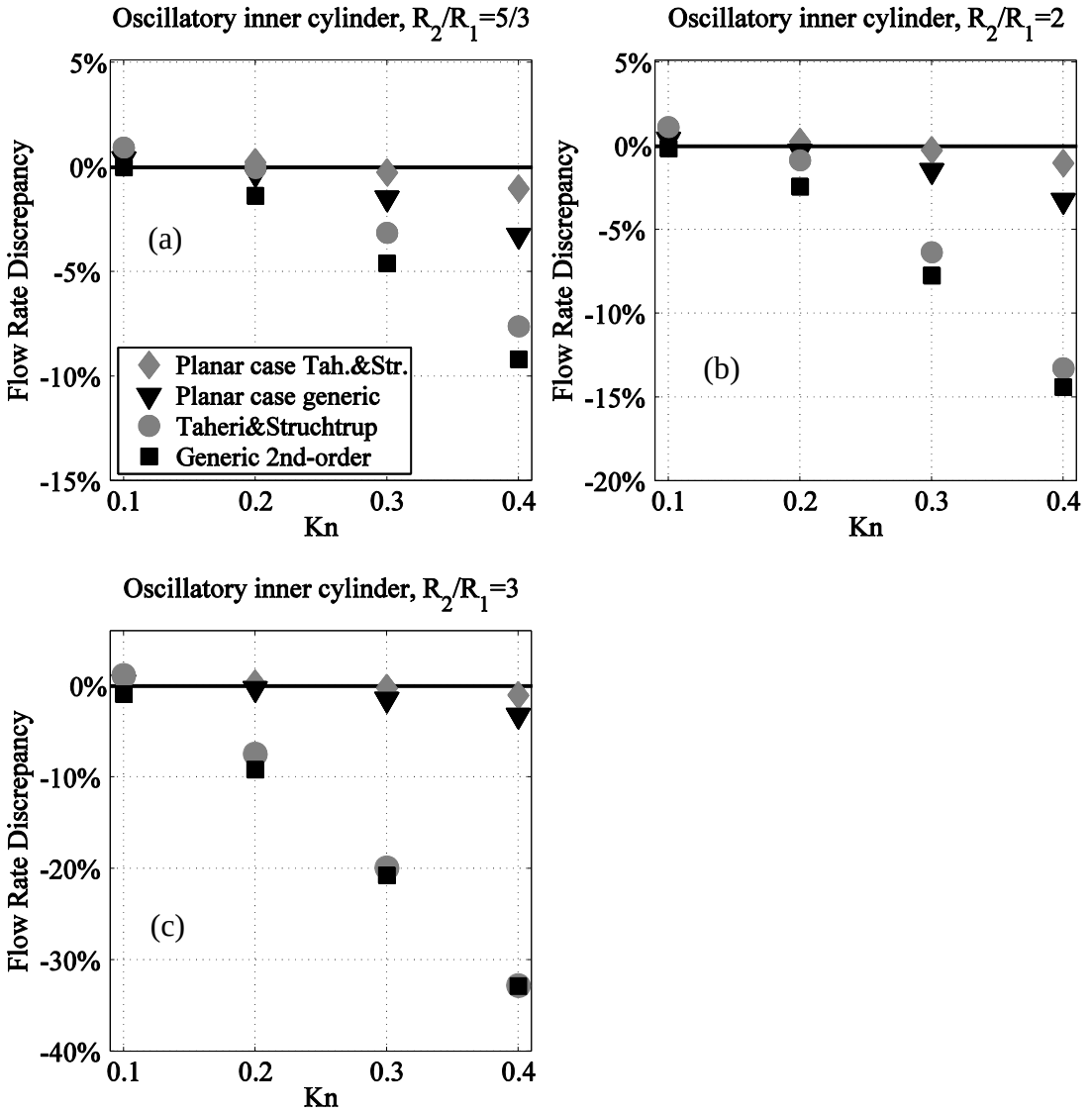

Figure 6.4: Flow rate discrepancies (ε) against Knudsen number at a Stokes number of $\beta = 1$ for the case when the inner cylinder is oscillating and the outer cylinder is stationary. The ratio of the outer cylinder radius to the inner cylinder radius is specified as: (a) $R_2 / R_1 = 5/3$, (b) $R_2 / R_1 = 2$ and (c) $R_2 / R_1 = 3$. The diamond and triangular symbols represent the flow rate discrepancies for the equivalent planar case obtained in the planar limit, $R_2 / R_1 \to 1$, using the Taheri and Struchtrup and the generic boundary conditions, respectively. A negative discrepancy indicates that the slip model predicts a lower flow rate compared to the DSMC solution. As the ratio of R_2 / R_1 increases, the curvature increases. The figures show that the flow rate discrepancies significantly increase with curvature and Knudsen number.

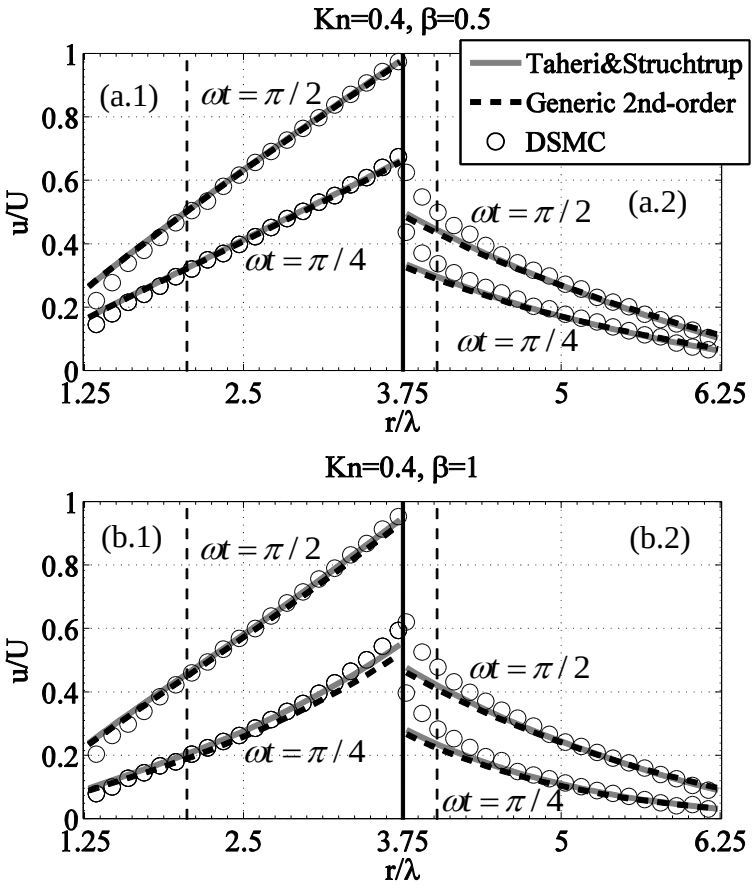

Figure 6.5: Comparison of velocity profiles over the concave and convex surfaces of an oscillatory cylindrical shell at a Knudsen number of 0.4. The oscillating shell is positioned between two stationary cylinders and has a radius of 3.75λ, where λ is the mean free path. The bold vertical lines in the figures represent the location of the shell. The left- and right-hand sides of the shell have concave and convex surfaces, respectively. Figs. (a.1) and (b.1) show the velocity profiles over the concave side, while Figs. (a.2) and (b.2) show the velocity profiles over the convex side of the shell. The dashed lines indicate the approximate spatial extent of the S-layers which are assumed to have a thickness of $\sim \lambda^2 / R$ where *R* is the radius of the convex cylinder. The Stokes number is specified as (a) $\beta = 0.5$ and (b) $\beta = 1$.

Figure 6.5 shows that the amount of slip over the convex side of the cylindrical shell is much larger than that over the concave side. It is interesting to note that in the equivalent planar flow case, the amount of slip would be equal on both sides of the oscillating surface. In addition, the discrepancies between the velocity profiles from the slip and DSMC solutions are also larger over the convex side compared to the concave side. Figure 6.5 therefore clearly shows the dramatic effect of surface shape on the flow behaviour and highlights the importance of the S-layer over convex surfaces.

The mass flow rate discrepancies in Fig. 6.3 and the velocity profiles in Fig. 6.5 show that the predictive capability of slip models is significantly reduced over convex surfaces. The figures also show that the boundary condition proposed by Taheri and Struchtrup (2009) is slightly more accurate than the generic boundary condition, in most of the cases considered. However, the Taheri and Struchtrup boundary condition is only valid for cylindrical geometries and therefore the generic second-order slip-velocity boundary condition is likely to be applicable to a wider range of flow geometries.

6.3 Conclusions

This chapter has presented the results of oscillatory rarefied flow over nonplanar surfaces in the early transition regime and highlights the important role of the curvature and the S-layer on the flow behaviour. The results clearly show the significant effects of surface shape (i.e. concave/convex) and reveal the presence of the S-layer over convex surfaces. In the case of the cylindrical form of Stokes' second problem, the results demonstrate that changes in the velocity profile due to curvature effects are more prominent at higher Knudsen numbers. In addition, it has been shown that the penetration depth decreases as the Knudsen number and the curvature increase due to the high amount of slip over the convex oscillating surface. In the case of nonplanar oscillatory Couette flow, it has been found that the amount of slip over the oscillating inner cylinder (i.e. over an oscillating convex surface) is larger than that over the oscillating outer cylinder (i.e. a concave surface). Moreover, the amount of slip over an oscillating convex surface increases with curvature whereas the slip-velocity over an oscillating concave surface decreases as the curvature increases. A similar opposing effect between concave and convex surfaces was originally predicted by Einzel et al. (1990). In addition, the study has proposed a generic second-order velocity-slip boundary condition for flow over non-planar surfaces. This boundary condition has been validated by comparing the results against both DSMC data and the second-order boundary condition developed by Taheri and Struchtrup (2009).

In the case of oscillatory Couette flow between two *parallel* plates, Hadjiconstantinou[2] has reported that the second-order slip solution is in very good agreement with DSMC data up to Kn≈0.4. On the other hand, Emerson et al. (2007),

using a first-order slip model, have shown that there are large discrepancies between the Navier-Stokes and DSMC solutions at Knudsen numbers beyond 0.1 in the case of an equivalent flow between two *concentric* cylinders. The present study has extended the analysis of nonplanar rarefied oscillatory flows using two different second-order slip formulations. To demonstrate the important role of the surface shape by eliminating the influence of the curvature and the surface area of the oscillating surface, the present study also considers a rarefied flow driven by a thin oscillatory cylindrical shell positioned in the middle of the gap between two concentric cylinders. The flow rate discrepancies between the DSMC data and the slip solutions demonstrate that curvature does not have a significant effect when the oscillatory flow is driven by a concave surface and the results show that second-order slip solutions are able to capture the flow rates with reasonable accuracy (i.e. < 2.5% error) for Knudsen numbers up to ~0.4. However, the results show that the predictive capability of second-order slip models is significantly reduced when the oscillatory flow is driven by a convex surface.

The growing influence of the Knudsen layer is expected to reduce the predictive capability of slip models in the early transition regime. However, this does not explain why slip models are significantly less accurate for nonplanar oscillatory flows compared to the equivalent planar case; nor does it explain why slip models show larger discrepancies against the DSMC results over an oscillating convex surface. These effects can be explained by the existence of the S-layer over the convex cylinder. The study highlights the potentially important effect of the S-layer and indicates that, under certain situations, the S-layer can affect the flow behaviour well away from a convex surface.

7. INVESTIGATION OF THE IMPULSIVELY-STARTED MICROFLOWS USING HEAVISIDE OPERATIONAL METHOD

The pioneering studies on the development of the operational methods were carried out by Oliver Heaviside (1850-1915). Heaviside reported that operational methods can be very practical in solving ordinary differential equations, but he did not propose a rigorous mathematical theory. Using and showing the significance of the operational approach, he obtained solutions straightforwardly for some differential equations of his interest, which were difficult to tackle otherwise. Later on, this approach led to the Fourier and Laplace transform methods in solution of differential equations and flourished.

The idea behind the operational method is treating and manipulating the differential operator as if it were a constant number. In this study, we are interested in solution of Stokes-type (linear) partial differential equations in order to understand the unsteady motion of gas in micro-scale, subject to the complicated slip boundary conditions. In the present chapter, we employ the operational method in order to investigate the impulsively-started cylindrical microflows associated with slip boundary conditions. Important to note that separation of variables technique cannot be applied straightforwardly here due to the complex form of the boundary condition of our interest, nor can the Laplace and Fourier transform methods be used easily. An integral transform method would require transformation of the boundary condition into the integral domain where equations could be treated, and the transform method eventually would give an expression requiring an inverse transformation which would be difficult to handle.

The Chapter 7 initially presents some useful theorems based on Goldstein (1932), Carslaw and Jaeger (1963), Jeffreys and Jeffreys (1999), and Glaeske et al. (2006) and gives the Heaviside expansion theorem, which will be used in Section 7.2 for the solution of the impulsively-started gas microflows with the nonplanar slip boundary conditions.

7.1 The Heaviside Expansion Theorem

Lemma 7.1: *Q is the integral operator acting on a function $f(t)$ as $Qf(t)=\int_0^t f(\xi)d\xi$. If $\int_0^t f(\xi)d\xi$ exits, any positive integer power of the integration operator Q can be expressed by a single integral as*

$$Q^n f(t)=\int_0^t \frac{(t-\xi)^{n-1}}{(n-1)!}f(\xi)d\xi, \qquad n\in\mathbb{N}^+.$$

(Convergence Theorem) Theorem 7.1: *If the series $\sum_{n=0}^{\infty}a_n z^n$ converges for some values of z other than zero, then the series $\left(\sum_{n=0}^{\infty}a_n Q^n\right)f(t)$ is uniformly and absolutely convergent for all values of t such that $\int_0^t f(\tau)d\tau$ exits, and is equal to*

$$a_0 f(t)+\sum_{n=1}^{\infty}\int_0^t a_n\frac{(t-\tau)^{n-1}}{(n-1)!}f(\tau)d\tau.$$

A direct result of the convergence Theorem 7.1 is Corollary 7.1.

Corollary 7.1: *If $F(z)$ is any function expansible to a power series near $z=0$ such that the power series is convergent for some values of z other than zero, then $F(Q)$ operating on a function $f(t)$, where $\int_0^t f(\tau)d\tau$ exits, is reducible to a function.*

Let us consider $F(z)=1/(1-az)$ where a is a constant. Power series of $F(z)$ near $z=0$ is convergent for $|z|<1/a$. Then $F(Q)$ can be expanded into series as $F(Q)=1+aQ+a^2Q^2+\ldots$. In case, $F(Q)$ is operating on function $f(t)=1$, we can write directly and *reduce* the operator function to

$$F(Q)\{1\}=(1+aQ+a^2Q^2+\ldots)1=\sum_{n=0}^{\infty}\frac{a^n t^n}{n!}=e^{at}, \qquad \textbf{(7.1)}$$

since positive integer powers of Q can be evaluated as

$$Q1=t,\ Q^2 1=\frac{t^2}{2!},\ Q^3 1=\frac{t^3}{3!}, \quad \ldots \quad ,Q^n 1=\frac{t^n}{n!},$$

where 1 is the unit function.

In fact, it can be easily shown that, by definition, $Q^2 f(t) = \int_0^t \int_0^\xi f(\tau) d\tau d\xi$ and it is over a triangular domain $\{(\tau, \xi) \mid 0 \le \tau \le \xi, 0 \le \xi \le t\}$. We can change the order of integration by describing the domain as $\{(\tau, \xi) \mid 0 \le \tau \le t, \tau \le \xi \le t\}$, and then can write that

$$\int_0^t \int_0^\xi f(\tau) d\tau d\xi = \int_0^t \int_\tau^t f(\tau) d\xi d\tau = \int_0^t (t-\tau) f(\tau) d\tau \qquad \textbf{(7.2)}$$

When $Q^2 f(t) = \int_0^t Q f(\tau) d\tau$ is integrated by parts, Eq. (7.2) can also be obtained. Similarly, by definition, $Q^3 f(t) = Q \int_0^t (t-\tau) f(\tau) d\tau = \int_0^t \int_0^\xi (\xi - \tau) f(\tau) d\tau d\xi$ and by re-describing the integral domain and then by changing the order of integration, we can obtain

$$\int_0^t \int_0^\xi (\xi - \tau) f(\tau) d\tau d\xi = \int_0^t \int_\tau^t (\xi - \tau) f(\tau) d\xi d\tau = \int_0^t \frac{(t-\tau)^2}{2} f(\tau) d\tau \qquad \textbf{(7.3)}$$

By induction, therefore it can be generalized to

$$Q^n f(t) = \int_0^t \frac{(t-\tau)^n}{(n-1)!} f(\tau) d\tau .$$

In the present chapter, while solving unsteady flow equations in Section 7.2, we will define $p := d/dt$ and obtain an expression in terms of *p*. Then we will replace *p* by Q^{-1} (inverse operator according to multiplication) and make use of the convergence Theorem 7.1. Moreover it is important to note that multiplication by the unit function on the right side of the operator will not sometimes be denoted for simplicity.

(Heaviside Expansion Theorem) Theorem 7.2: *Let F(z) and G(z) be polynomials such that the degree of F(z) is m and the degree of G(z) is n, with* $m \le n$. *If G(z) has n simple roots such that* $\alpha_1, \alpha_2, \ldots, \alpha_n$ *and* $G(0) \ne 0$ *then the operational function* $F(p)/G(p)$ *can be expressed as*

$$\frac{F(p)}{G(p)} = \frac{F(0)}{G(0)} + \sum_{i=1}^{n} \frac{F(\alpha_i)}{\alpha_i G'(\alpha_i)} \exp(\alpha_i t)$$

where $G'(z) = dG(z)/dz$.

Proof: Since $G(z)$ has n simple zeros $\alpha_1, \alpha_2, \ldots, \alpha_n$ and the degree of $G(z)$ is greater than or equal to the degree of $F(z)$, the rational function $F(z)/G(z)$ can be split into partial fractions as

$$\frac{F(z)}{G(z)} = \frac{c_1}{(z-\alpha_1)} + \frac{c_2}{(z-\alpha_2)} + \ldots + \frac{c_n}{(z-\alpha_n)}. \tag{7.4}$$

This can be written as $\frac{F(p)}{pG(p)} = \frac{F(0)}{pG(0)} + \sum_{i=1}^{n} \frac{c_i}{p-\alpha_i}$

if the coefficients c_n are chosen as

$$\begin{aligned} c_i &= \lim_{p\to\alpha_i}(p-\alpha_i)\frac{F(p)}{pG(p)} = \lim_{p\to\alpha_i}(p-\alpha_i)\frac{F(p)}{p(G(p)-G(\alpha_i))} \\ &= \lim_{p\to\alpha_i}\frac{F(p)}{p\dfrac{G(p)-G(\alpha_i)}{(p-\alpha_i)}} = \frac{F(\alpha_i)}{\alpha_i G'(\alpha_i)} \end{aligned} \tag{7.5}$$

Then we can write

$$\begin{aligned} \frac{F(p)}{G(p)} &= \frac{F(0)}{G(0)} + \sum_{i=1}^{n}\frac{F(\alpha_i)}{\alpha_i G'(\alpha_i)}\frac{p}{(p-\alpha_i)} \\ &= \frac{F(0)}{G(0)} + \sum_{i=1}^{n}\frac{F(\alpha_i)}{\alpha_i G'(\alpha_i)}\frac{1}{(1-\alpha_i Q)} \end{aligned} \tag{7.6}$$

Since $1/(1-\alpha_i Q)1 = \exp(\alpha_i t)$, we obtain

$$\frac{F(p)}{G(p)} = \frac{F(0)}{G(0)} + \sum_{i=1}^{n}\frac{F(\alpha_i)}{\alpha_i G'(\alpha_i)}\exp(\alpha_i t). \blacksquare$$

The Heaviside expansion theorem also called the *partial fractional rule*. The Heaviside expansion theorem is also true when $G(z)$ has multiple zeros. In the presence of multiple roots of any order $r \geq 1$, the coefficients c_n in Eq. (7.5) can be found using

$$c_i = \frac{1}{(r-1)!}\lim_{z\to\alpha_i}\frac{d^{r-1}}{dz^{r-1}}((\alpha_i - z)^r \frac{F(z)}{G(z)}) \tag{7.7}$$

In this case, we need operator rules other than $1/(1-aQ)1 = p/(p-a)1 = e^{at}$, such as

$$p/(p-a)^r 1 = \frac{t^{r-1}}{(r-1)!}e^{at} \tag{7.8}$$

where *a* is a constant and 1 is the unit function.

Corollary 7.2 (Glaeske et al., 2006): *A rational operator* $F(p)/G(p)$ *is reducible to a function if and only if the degree of the polynomial F(p) is less than or equal to the degree of the polynomial G(p).*

Corollary 7.3 (Pennel, 1929): *Let q(p) an analytical function of p and* $F(p)/G(p) = R(q)/S(q)$*, the Heaviside expansion theorem can be written as*

$$\frac{R(q)}{S(q)} = \frac{R(0)}{S(0)} + \sum_{i=1}^{n} \frac{R(\beta_i)}{\beta_i S'(\beta_i)} \phi(t, \beta_i)$$

where S(q) has simple roots such that $\beta_1, \beta_2, \ldots, \beta_n$*, and* $\phi(t, \beta_i)$ *is the function of t and* β_i *corresponding to the operational expression* $q/(q - \beta_i)$.

7.2 Impulsively-Started Cylindrical Microflows

Three fundamental time-dependent nonplanar microflows, namely, (a) flow inside an impulsively–started rotating micro-cylinder, (b) flow between impulsively–started rotating concentric micro-cylinders, and (c) flow over an impulsively–started rotating micro-cylinder (i.e. the cylindrical form of Stokes' first problem) have been investigated using the operational method. The Knudsen number is specified in the early transition regime (i.e. 0.1<Kn<1.0). The motion of the gas is assumed to be incompressible and two-dimensional.

The first- and second-order velocity-slip boundary conditions are employed. The velocity profiles are examined in order to highlight the significance of the effects of curvature and the surface shape. Results predict the existence of the S-layer over a convex surface. Although the S-layer was discovered by Sone (1973) as a thin sub-layer under the Knudsen layer, results show that its influence on the flow behaviour is rather significant. A detailed analysis has been conducted to distinguish the effects of the Knudsen layer and S-layer. In addition, vorticity (it is a measure of the rate of rotation) and shear stress (it is a tangential force exerted by fluid to the surface) near both surfaces have been examined.

7.2.1 Motion of gas inside a rotating micro-cylinder

Gas inside a circular cylinder impulsively starts rotating with an angular velocity Ω. The radius of the cylinder is *R* shown in Figure 7.1. Then the velocity is only a function of time *t* and radial distance *r*. The Navier-Stokes equation can be written as (White, 1991)

$$\frac{\partial u}{\partial t} = \left[\frac{\partial^2 u}{\partial r^2} + \frac{1}{r}\frac{\partial u}{\partial r} - \frac{u}{r^2} \right] \tag{7.9}$$

where ν is the kinematic viscosity and $u(r,t)$ is the velocity in the radial direction. At time t=0, velocity is zero. After an amount of time, velocity at the cylinder surface develops to ΩR (i.e. $u(r, t \to \infty) = \Omega R$).

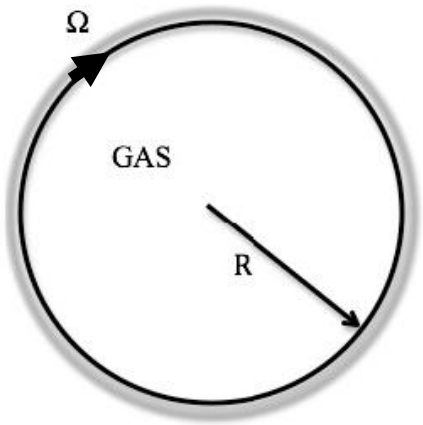

Figure 7.1: Flow inside an impulsively–started rotating micro-cylinder.

The momentum equation (i.e. Eq. (7.9)) is a linear partial differential equation and here it can be solved using the separation of variables technique. However, here it will be solved using the Heaviside's operational method (Goldstein, 1932). The equation (7.9) can be transformed into the Bessel equation by replacing the time operator $\partial/\partial t$ with p, where $p = \nu q^2$ (Goldstein, 1932). Here it is important to remember that when $q(p)$ is an analytic function of p, we can employ Corollary 7.3 and then use the Heaviside expansion theorem (Theorem 7.2). Thus Equation (7.9) can be written as

$$\frac{\partial^2 u}{\partial r^2} + \frac{1}{r}\frac{\partial u}{\partial r} - \frac{u}{r^2} - q^2 u = 0 \tag{7.10}$$

The general solution of Eq. (7.10) can be found in terms of modified Bessel functions applying by the Frobenius method. The solution must remain finite at $r = 0$ and then the general solution is written as

$$u(r,t) = CI_1(qr) \tag{7.11}$$

where $I_1(\cdot)$ is the first-order modified Bessel function of the first kind and C is a constant that is determined using boundary conditions.

The second-order velocity-slip boundary condition is

$$u(R,t) = \Omega R - A_1 \frac{2-\sigma}{\sigma} \frac{\lambda}{\mu} \frac{\partial \tau}{\partial r}\bigg|_{r=R} - A_2 \frac{\lambda^2}{\mu} \frac{\partial^2 \tau}{\partial r^2}\bigg|_{r=R} \tag{7.12}$$

where R is the radius of the cylinder, Ω is the angular velocity of the cylinder, σ is the tangential momentum accommodation coefficient, λ is the mean free path, μ is the dynamic viscosity, τ is the shear stress, A_1 and A_2 are the first- and second-order slip coefficients, respectively. The first- and second-order slip coefficients are specified as $A_1 = 1.11$ and $A_2 = 0.61$ (following (Hadjiconstantinou, 2005)). The mean free path definition is $\lambda = (\mu/\phi)\sqrt{\pi \Re T}$, where ϕ is the pressure, $\Re$ is the specific gas constant and T is the temperature. The Knudsen number is $Kn = \lambda / R$.

The general solution in Eq. (7.11) can be rearranged by using boundary condition in Eq. (7.12) as follows

$$\frac{u(r,t)}{\Omega R} = \frac{I_1(qr)}{Kn(A_1 - 2A_2 Kn)qRI_2(qR) + (1 + A_2 Kn^2 q^2 R^2) I_1(qR)} \tag{7.13}$$

The Eq. (7.13) is an even function of q and the denominator has zeros. The partial fraction rule (according to the Heaviside expansion theorem 7.2) is

$$\frac{f(p)}{F(p)} = \frac{f(0)}{F(0)} + \sum_{\alpha_n} \frac{f(\alpha_n)}{\alpha_n F'(\alpha_n)} \exp(\alpha_n t) \tag{7.14}$$

where $f(p)$ and $F(p)$ are the nominator and denominator of Eq. (7.14), respectively, α are the zeros of $F(p)$, the function $F(\cdot)$ represents the derivative of $F'(\cdot)$ with respect to p and the summation is over all the zeros. Since p is equal to νq^2, a derivation rule can be written as

$$p\frac{dF}{dp}=\frac{1}{2}q\frac{dF}{dq} \tag{7.15}$$

Applying the partial fraction rule, the general solution can be written in terms of Bessel functions as

$$\frac{u(\hat{r},t)}{\Omega R}=\hat{r}+2\sum_{\alpha_n}\frac{J_1(\alpha_n)}{\Gamma_1\alpha_n J_0(\alpha_n\hat{r})-\Gamma_2 J_1(\alpha_n)}\exp(\alpha_n^2\, \nu t/R^2) \tag{7.16}$$

$$\Gamma_2=1-Kn(A_1+A_2Kn(\alpha_n^2-2)) \tag{7.17}$$

$$\Gamma_2=1+A_1Kn(\alpha_n^2-2)-A_2Kn^2(\alpha_n^2-4) \tag{7.18}$$

where $\hat{r}=r/R$ is the nondimensional radial distance and $J_0(\cdot)$ and $J_1(\cdot)$ are the first-order Bessel functions of the first and second kind, Kn is the Knudsen number. First term in Eq. (7.16) represents the steady-state solution, and at steady-state slip solution in Eq. (7.16) predicts no slip at the cylinder surface (i.e. rigid body rotation). The rarefaction plays a role only in the time taken to reach steady-state.

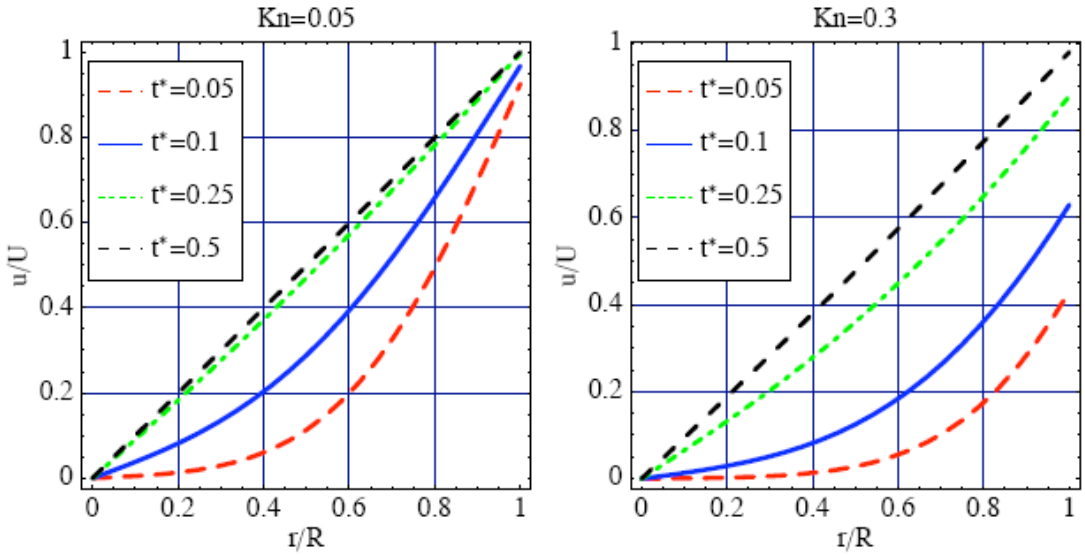

Figure 7.2: Nondimensional velocity profiles at Kn=0.05 and Kn=0.3. Velocities are nondimensionalized using $U=\Omega R$, where R is the radius of the cylinder. The nondimensional time is $t^*=\nu t/R^2$.

The shear stress is a measure of momentum transfer to the surface. The amount of slip on the surface and the formation of Knudsen layer can be expected to be related to the shear stress. The shear stress τ can be found using this formula (White, 1991)

$$\tau(r)=\mu\left(\frac{\partial u}{\partial r}-\frac{u}{r}\right) \tag{7.19}$$

where μ is the dynamical viscosity.

Microflows generally move very slowly and therefore mixing fluids efficiently is a problem. Curved surfaces generate vorticities (Sudarsan and Ugaz, 2005) and can have a role on designing efficient micro-mixers. The vorticity can be found (White, 1991)

$$V(r) = \frac{\partial u}{\partial r} + \frac{u}{r}. \qquad \textbf{(7.20)}$$

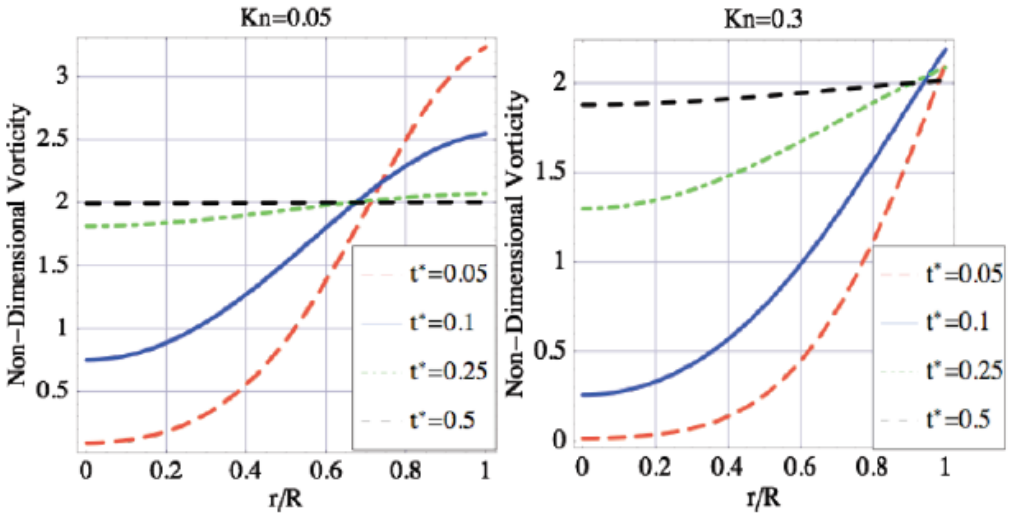

Figure 7.3: Nondimensional shear stresses at Kn=0.05 and Kn=0.3. Figures show that shear stress is larger at higher Knudsen numbers at mean times; however at steady state shear stress is zero at any Knudsen number. The nondimensional time is $t^* = \nu t / R^2$. For $t^* = 0.05$, $t^* = 0.1$, $t^* = 0.25$ and $t^* = 0.5$, colours are red, blue, green and black, respectively.

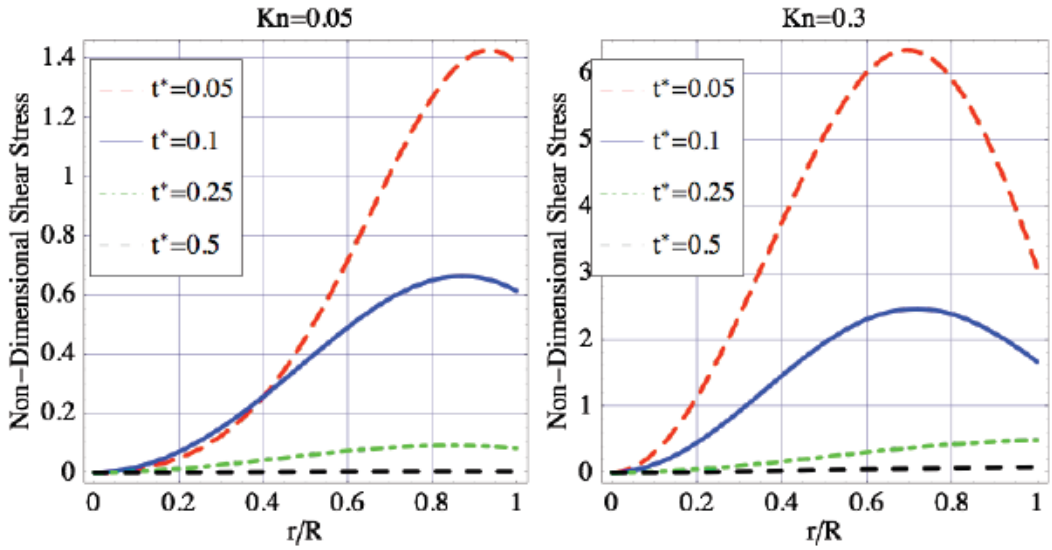

Figure 7.4: Nondimensional vorticities at Kn=0.05 and Kn=0.3. At steady-state the value of vorticity is 2 at any Knudsen number. The non-dimensional time is $t^* = \nu t / R^2$.

7.2.2 Motion of gas between two rotating concentric micro-cylinders

Gas between two circular cylinders impulsively starts rotating with angular velocities ω at the inner cylinder and Ω at the outer cylinder. The radii of the inner and outer cylinders are R_1 and R_2, respectively as shown in Figure 7.5.

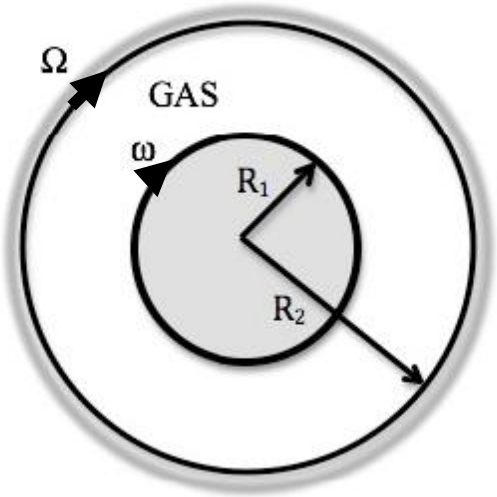

Figure 7.5: Flow between impulsively–started rotating concentric micro-cylinders.

The motion of gas obeys the momentum equation in Eq. (7.10). Then the general solution can be written as

$$u(r,t) = C_1 I_1(qr) + C_2 K_1(qr) \qquad \textbf{(7.21)}$$

where $I_1(\cdot)$ and $K_1(\cdot)$ are the first-order modified Bessel functions of the first and second kind, r is the redial distance, q is equal to $\sqrt{p/\nu}$, where $p = \partial/\partial t$ is the time derivative, and C_1 and C_2 are constants that are determined using boundary conditions.

The second-order velocity-slip boundary conditions at both surfaces are written as

$$u(R_1,t) = \omega R_1 + A_1 \frac{2-\sigma}{\sigma}\frac{\lambda}{\mu}\frac{\partial \tau}{\partial r}\bigg|_{r=R_1} - A_2 \frac{\lambda^2}{\mu}\frac{\partial^2 \tau}{\partial r^2}\bigg|_{r=R_1} \tag{7.22}$$

$$u(R_2,t) = \Omega R_1 - A_1 \frac{2-\sigma}{\sigma}\frac{\lambda}{\mu}\frac{\partial \tau}{\partial r}\bigg|_{r=R_2} - A_2 \frac{\lambda^2}{\mu}\frac{\partial^2 \tau}{\partial r^2}\bigg|_{r=R_2} \tag{7.23}$$

where A_1 is the first-order slip coefficient, σ is the tangential momentum accommodation coefficient, λ is the mean free path, ν is the dynamic viscosity, τ is the shear stress and A_2 is the second-order slip coefficient. The Knudsen number is $Kn = \lambda/(R_2 - R_1)$.

The partial fraction rule in Eq. (7.14) and the derivative rule in Eq. (7.15) are used for obtaining the general solution. For simplicity, the general solution is obtained either when the inner cylinder rotates whereas the outer cylinder at rest (i.e. $\Omega = 0$) or when the outer cylinder rotates whereas the inner cylinder at rest (i.e. $\omega = 0$). The solution represented here is obtained using first-order velocity-slip boundary condition (i.e. $A_1 = 1.11$ and $A_2 = 0$).

The general solution when the inner cylinder is rotating is

$$u(r^*,t) = \frac{1}{(1+r^*(\chi-1))}\left(\frac{\chi^2 - \Gamma_1(1+r^*(\chi-1))^2}{\Gamma_2\chi^2 - \Gamma_1}\right) + \pi\sum_{\alpha_n}\frac{\mathrm{H}_1(\alpha_n)+\mathrm{H}_2(\alpha_n)}{\mathrm{M}(\alpha_n)}\exp(-\alpha_n^2 t^*) \tag{7.24}$$

$$\mathrm{H}_1(\alpha_n) = \Gamma_1\left[Y_1(\alpha_n r^*)J_1(\chi\alpha_n) - Y_1(\chi\alpha_n)J_1(\alpha_n r^*)\right] \tag{7.25}$$

$$\mathrm{H}_2(\alpha_n) = A_1 Kn(1-1/\chi)\chi\alpha_n\left[Y_1(\alpha_n r^*)J_0(\chi\alpha_n) - Y_0(\chi\alpha_n)J_1(\alpha_n r^*)\right] \tag{7.26}$$

$$\mathrm{M}(\alpha_n)=\left(\begin{array}{l}(-\Gamma_1^2-2\Gamma_1\mathrm{H}_2(\alpha_n)-\chi^2\mathrm{H}_2^2(\alpha_n)\alpha_n^2)(\Gamma_2 J_1(\alpha_n)-\mathrm{H}_1(\alpha_n)\alpha_n J_0(\alpha_n))^2+\\(\Gamma_2^2-2\Gamma_2\mathrm{H}_1(\alpha_n)+\mathrm{H}_1^2(\alpha_n)\alpha_n^2)(\Gamma_1 J_1(\chi\alpha_n)+\mathrm{H}_2(\alpha_n)\alpha_n\chi J_0(\chi\alpha_n))^2\end{array}\right)\Big/ ((\Gamma_2 J_1(\alpha_n)-\mathrm{H}_1(\alpha_n)\alpha_n J_0(\alpha_n))(\Gamma_1 J_1(\chi\alpha_n)+\mathrm{H}_2(\alpha_n)\alpha_n\chi J_0(\chi\alpha_n)))$$

(7.27)

$$\Gamma_1=1-2A_1Kn(1-1/\chi) \quad \textbf{(7.28)}$$

$$\Gamma_1=1+2A_1Kn(1-\chi) \quad \textbf{(7.29)}$$

where $\chi=R_2/R_1$ is the ratio between cylinder radii, $r^*=(r-R_1)/(R_2-R_1)$ is the nondimensional radial distance, $t^*=\nu t/R^2$ is the nondimensional time, A_1 is the first-order slip coefficient, Kn is the Knudsen number and α are the zeros of equation (7.30) below.

$$\begin{array}{l}(-\mathrm{H}_1(\alpha_n)\alpha_n J_0(\alpha_n)+\Gamma_2 J_1(\alpha_n))(\mathrm{H}_2(\alpha_n)\chi\alpha_n Y_0(\chi\alpha_n)+\Gamma_1 Y_1(\chi\alpha_n))-\\(-\mathrm{H}_1(\alpha_n)\alpha_n Y_0(\alpha_n)+\Gamma_2 Y_1(\alpha_n))(\mathrm{H}_2(\alpha_n)\chi\alpha_n J_0(\chi\alpha_n)+\Gamma_1 J_1(\chi\alpha_n))=0.\end{array} \quad \textbf{(7.30)}$$

The general solution when the outer cylinder is rotating is

$$u(r^*,t)=\frac{\chi}{(1+r^*(\chi-1))}\left(\frac{\chi^4-\Gamma_1(1+r^*(\chi-1))^2}{\chi^2(\Gamma_2\chi^2-\Gamma_1)}\right)+ \pi\sum_{\alpha_n}\frac{\mathrm{H}_3(\alpha_n)+\mathrm{H}_4(\alpha_n)}{\mathrm{M}(\alpha_n)}\exp(-\alpha_n^2 t^*) \quad \textbf{(7.31)}$$

$$\mathrm{H}_3(\alpha_n)=\Gamma_2(Y_1(\alpha_n r^*)J_1(\alpha_n)-Y_1(\alpha_n)J_1(\alpha_n r^*)) \quad \textbf{(7.32)}$$

$$\mathrm{H}_4(\alpha_n)=A_1Kn(\chi-1)\alpha_n(Y_1(\alpha_n r^*)J_0(\alpha_n)-Y_0(\alpha_n)J_1(\alpha_n r^*)) \quad \textbf{(7.33)}$$

where $\chi=R_2/R_1$ is the ratio between cylinder radii, $r^*=(r-R_1)/(R_2-R_1)$ is the nondimensional radial distance, $t^*=\nu t/R^2$ is the nondimensional time, A_1 is the first-order slip coefficient, Kn is the Knudsen number, α are the zeros of equation (7.30) and $\mathrm{M}(\alpha_n)$, Γ_1 and Γ_2 are defined in Eqs. (7.27), (7.28) and (7.29), respectively.

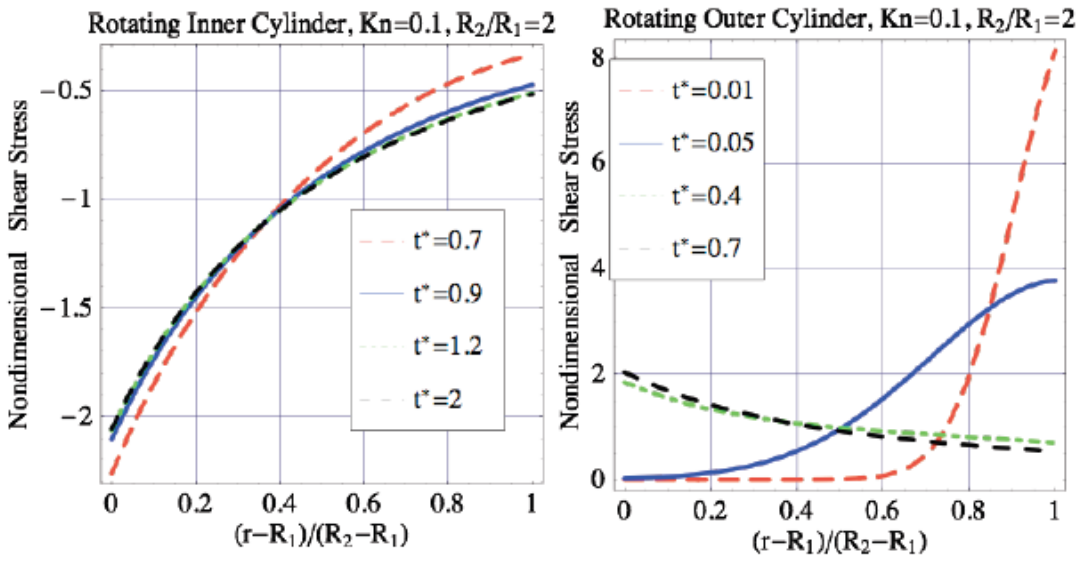

Figure 7.6: Nondimensional shear stresses at Kn=0.1. The inner and outer cylinders start rotating suddenly. The nondimensional time is $t^* = vt/R_1^2$, R_1 and R_2 are the inner and outer cylinder radius, respectively.

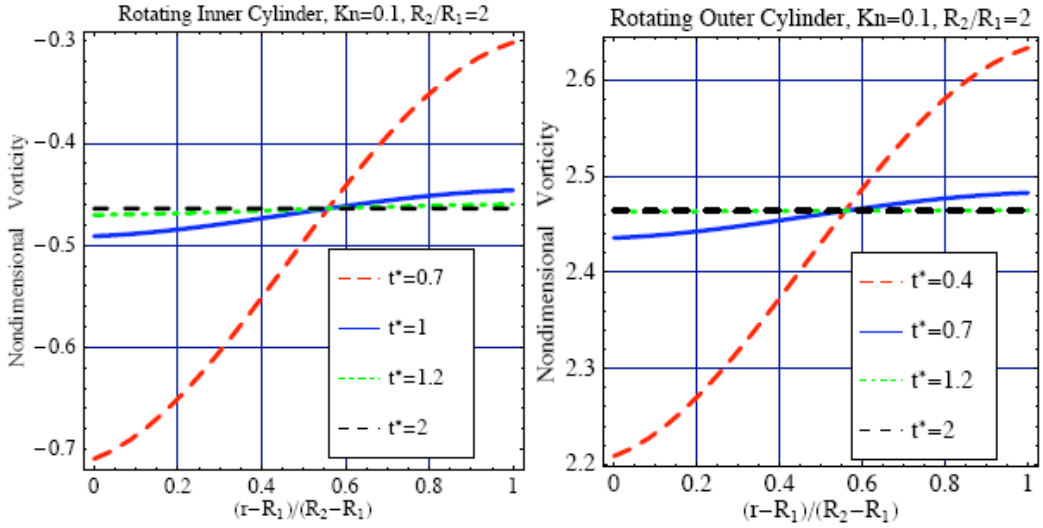

Figure 7.7: Nondimensional vorticities at Kn=0.1. The inner and outer cylinders start rotating suddenly. The nondimensional time is $t^* = vt/R_1^2$, R_1 and R_2 are the inner and outer cylinder radius, respectively.

7.2.3 Motion of gas over a rotating micro-cylinder

Gas over a circular cylinder impulsively starts rotating with an angular velocity ω. The radius of the cylinder is *R* as shown in Figure 7.8.

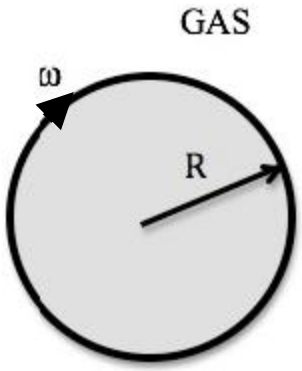

Figure 7.8: Flow over an impulsively–started rotating micro-cylinder.

The motion of gas obeys the momentum equation in Eq. (7.2). The general solution must remain finite at the far-field away from the cylinder and thus the solution can be written as

$$u(r,t) = CK_1(qr) \tag{7.34}$$

where $K_1(\cdot)$ is the first-order modified Bessel function of the second kind, r is the redial distance, q is equal to $\sqrt{p/\nu}$, where $p = \partial/\partial t$ is the time derivative, and C_1 is a constant that is determined using boundary conditions.

The partial fraction rule is not suitable here. The general solution is obtained using Bromwich's integral based on (Goldstein, 1932). Bromwich used the theory of complex functions in order to explain and extend the Heaviside's operational method (Carslaw and Jaeger, 1963). Thus using Bromwich's approach (Goldstein, 1932), the general solution can be found as

$$\frac{u(\hat{r},t)}{\omega R} = \frac{1}{\hat{r}}\frac{1}{1+2A_1Kn+4A_2Kn^2} - \frac{2}{\pi}\int_0^\infty \frac{\Gamma_1 Y_0(\xi)J_1(\xi\hat{r}) - \Gamma_2 Y_1(\xi) + (\Gamma_3 J_1(\xi) + \Gamma_1 J_2(\xi))Y_1(\xi\hat{r})}{\xi(\Gamma_3^2 J_1^2(\xi) + 2\Gamma_1\Gamma_3 J_1(\xi)J_2(\xi) + \Gamma_1^2 J_2^2(\xi) + (\Gamma_1 Y_0(\xi) - \Gamma_2 Y_0^2(\xi)))} d\xi \tag{7.35}$$

$$\Gamma_1 = \xi(A_1 + 2A_2Kn)Kn \tag{7.36}$$

$$\Gamma_2 = 1 + 2A_1 + A_2Kn(\xi - 4) \tag{7.37}$$

$$\Gamma_3 = 1 - 2A_2Kn^2\xi^2 \tag{7.38}$$

where $\hat{r} = r/R$ is the nondimensional radial distance, $J_0(\cdot)$ and $J_1(\cdot)$ are the zeroth and first-order Bessel functions of the first kind, $Y_0(\cdot)$ and $Y_1(\cdot)$ are the zeroth and first-order Bessel functions of the second kind, respectively, A_1 and A_2 are the first- and second-order slip coefficients, respectively. The Knudsen number is $Kn = \lambda/R$, where λ is the mean free path and R is the cylinder radius. First term in Eq. (7.35) is steady-state solution and predicts more slip while the Knudsen number increases.

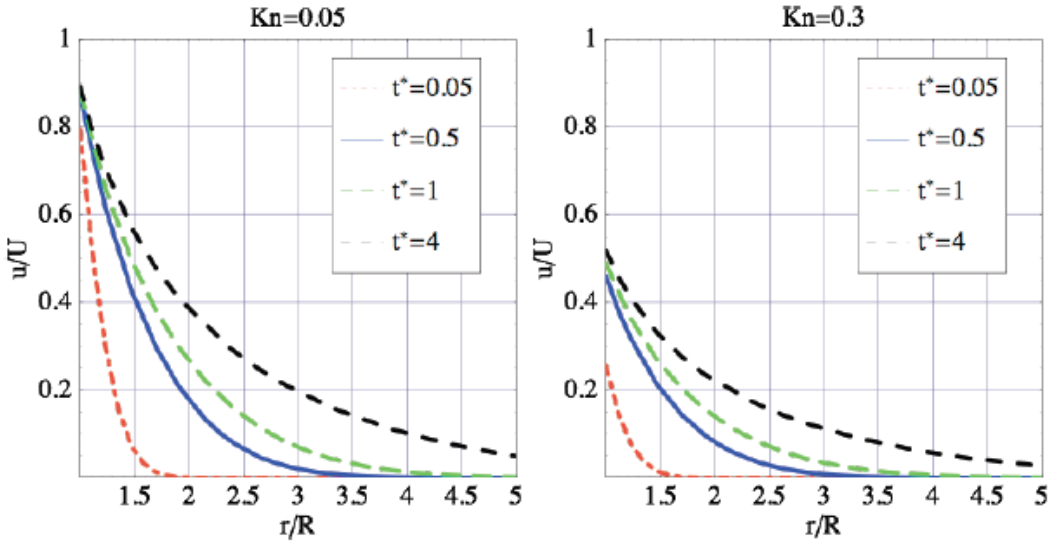

Figure 7.9: Nondimensional velocity profiles at Kn=0.05 and Kn=0.3. Velocities are nondimensionalized using $U = \omega R$, where R is the radius of the cylinder. The nondimensional time is $t^* = \nu t/R^2$. For $t^* = 0.05$, $t^* = 0.5$, $t^* = 1$ and $t^* = 4$, colours are red, blue, green and black, respectively.

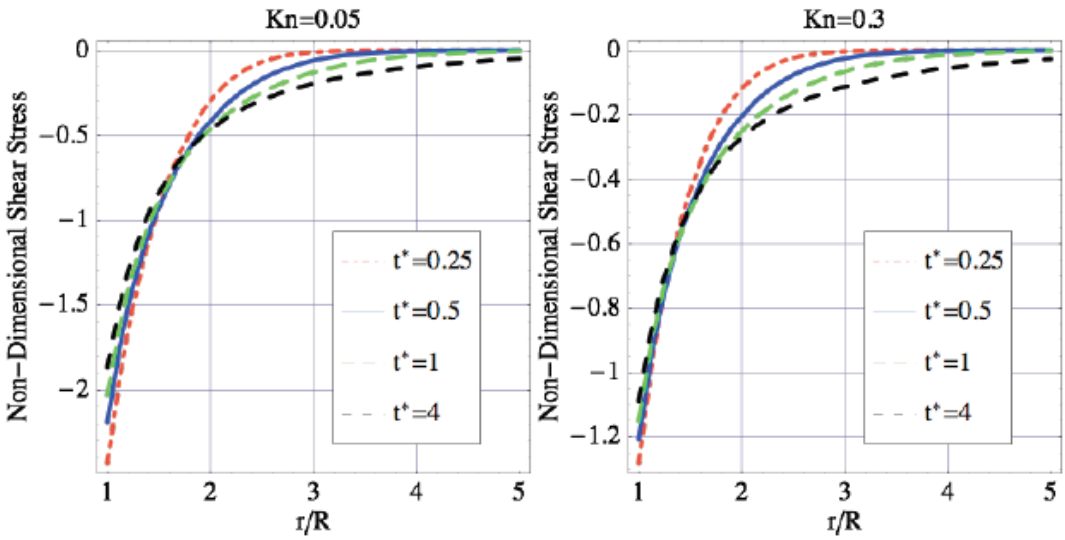

Figure 7.10: Nondimensional shear stresses at Kn=0.05 and Kn=0.3. The non-dimensional time is $t^* = \nu t / R^2$.

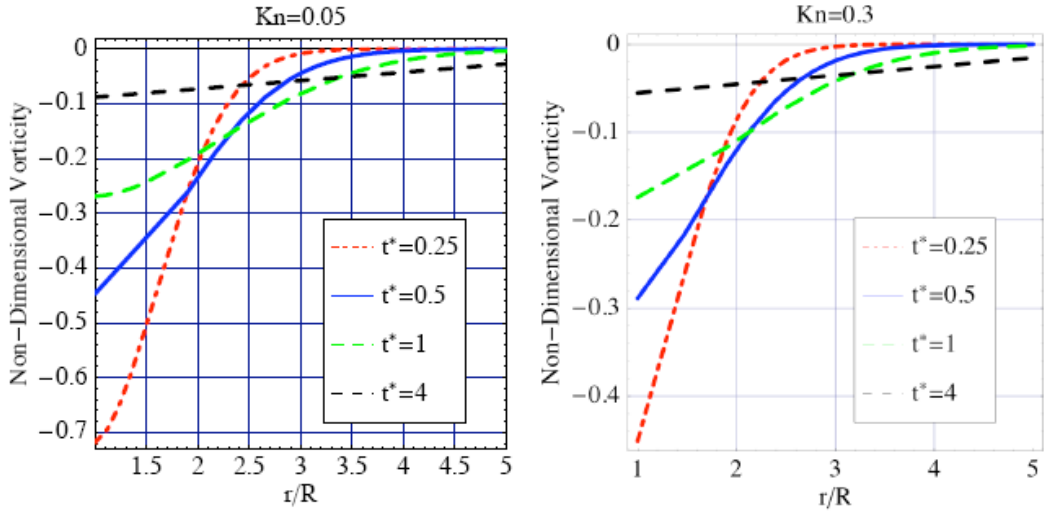

Figure 7.11: Nondimensional vorticities at Kn=0.05 and Kn=0.3. At steady-state the value of vorticity is zero at any Knudsen number.

7.3 Results and Discussions

Three fundamental time-dependent nonplanar microflows, namely, (a) flow inside an impulsively–started rotating micro-cylinder, (b) flow between impulsively–started rotating concentric micro-cylinders, and (c) flow over an impulsively–started rotating micro-cylinder (i.e. the cylindrical form of Stokes' first problem) have been investigated.

The steady-state vorticities of all three flow cases are independent of radial distance. Moreover, in flow cases (a) and (c), the magnitudes of the steady-state vorticity are

independent of Knudsen number. On the other hand, in flow case (b), the magnitude of the vorticity decreases as the Knudsen number increases.

The magnitudes of the steady-state shear stresses in flow cases (b) and (c) decrease with Knudsen number. However the magnitude of the shear stress is zero in flow case (a). As a result, in flow case (a), the steady-state motion of the gas is equivalent to a solid body rotation.

In flow cases (b) and (c), as the Knudsen number increases, the gas slides more effectively over the cylinder walls. However, in flow case (a), the Knudsen number is only influential in the time taken to reach steady-state, and the slip model predicts zero slip-velocity at all Knudsen numbers. This may be the result of the concave shape of the rotating surface.

As the Knudsen number increases, the time taken to reach steady-state increases in all flow cases. Moreover, in flow case (c), the time taken to reach steady-state increases away from the cylinder.

Curvature is defined as the inverse of the rotating cylinder radius. In flow case (b), the slip-velocity on the rotating inner cylinder increases with curvature. Conversely, the slip-velocity on the rotating outer cylinder decreases with curvature. This shows that there is an opposing effect of curvature on the slip at the inner and outer cylinder surfaces. Interestingly, this contrary curvature effect may explain why velocity inversion occurs in a flow between rotating concentric cylinders while it does not occur in the equivalent flow case between two parallel plates. Moreover, a velocity inversion analysis has shown that as curvature increases, velocity inversion can occur more easily.

In flow cases (a) and (c) when curvature increases, the flow reaches steady-state more quickly. Conversely, in flow case (b) the time taken to reach steady-state increases with curvature. In flow case (b), the flow induced by the rotating outer cylinder reaches steady-state more quickly compared to the flow with the rotating inner cylinder

8. ROLE OF SURFACE IN BOUNDARY SLIP AND VELOCITY DEFECT

8.1 Introduction

The Knudsen layer is crucially important when modelling the flow behaviour in gas-phase microdevices. The Knudsen layer manifests itself as a significant velocity defect close to the wall, which is a deviation between the actual velocity profile and that predicted by the Navier-Stokes equations. Although many microfluidic devices contain curved surfaces, relatively little research has been conducted on the formation of the Knudsen layer over curved surfaces. The present chapter demonstrates the influence of the surface (convex/concave) shape on the formation of the Knudsen layer. In addition, the study presented in this chapter reveals a relation between the shear stress exerted on the surface and the formation of the Knudsen layer.

The Knudsen layer (KL) extends just over one mean free path from a surface, and within this layer the momentum and heat transfer properties of the gas deviate considerably from the conventional continuum description of the fluid (Cercignani, 2000; Zhang et al., 2006). The formation of the KL and the transport properties within the KL have been extensively studied for flows associated with planar surfaces (Zhang et al., 2006; Reese and Zhang, 2009; Gu et al., 2010). The KL manifests itself as a significant velocity defect close to the surface. As the Knudsen number increases, the KL becomes increasingly influential on the flow behaviour, and the predictive capabilities of the Navier-Stokes equations are significantly reduced. The Knudsen number is defined as $Kn = \lambda / L$, where λ is the mean free path of the gas molecules and L is the characteristic length scale of the device. The Knudsen number in fact relates thickness of the KL ($\sim \lambda$) to the length scale of the flow domain. Therefore, when the Knudsen number increases beyond 0.1, the growing influence of the Knudsen layer is expected to cause a considerable velocity defect at the surface.

The present study considers a gas microflow driven by a thin rotating cylindrical shell positioned in the middle of gap between two concentric micro-cylinders. A generic second-order slip model (the Navier-Stokes equations with slip boundary

conditions) is employed for cylindrical surfaces. The velocity defect is calculated as the difference between the normalised velocities from the slip and DSMC solutions. DSMC method is used with a modification in the calculation of the maximum collision number in a cell (Stefanov et al., 1998). The simulations consider a hard-sphere model for argon at STP conditions, and the flow domain is divided into 200 cells with each cell containing 1000 simulation particles on average. The present study shows the profound role of the surface shape in the flow behaviour by eliminating the effects of curvature and surface area. The study also demonstrates anomalous velocity and temperature profiles that appear in nonplanar micro-geometries due to the curved surface shape.

8.2 Shell Problem and Formation of the Knudsen Layer

In a cylindrical-polar coordinate (r,θ) reference frame, the circumferential momentum expression of the incompressible Navier-Stokes equations is written as

$$\frac{d^2u}{dr^2}+\frac{d}{dr}\left(\frac{u}{r}\right)=0 \qquad \textbf{(8.1)}$$

where u is the velocity in the tangential direction and r is the radial distance. The general solution of Eq. (8.1) is written as

$$u(r)=C_1r+\frac{C_2}{r} \qquad \textbf{(8.2)}$$

where C_1 and C_2 are constants which are determined using the slip boundary condition.

Higher-order velocity-slip boundary conditions have great practical importance since they improve the accuracy of first-order slip models and extend the validity of the Navier-Stokes equations into the higher Knudsen numbers. Therefore several second-order slip models are proposed in the literature as reviewed by Barber and Emerson (2006) and Cao et al. (2009). Most of these boundary conditions can only be applied to planar surfaces; nevertheless novel slip boundary conditions and their predictive capabilities are subject of recent studies (Graur et al., 2009; Cercignani and Lorenzani, 2010; Perrier et al., 2011). To analyze the flow over cylindrical surfaces, we adopt a generic second-order slip boundary condition, formerly

developed by Sone (1969) for an arbitrary surface shape, and we express it by incorporating the Maxwell first-order slip boundary condition (Maxwell, 1879) as follows:

$$u_{slip} = u_{\text{gas}} - u_{\text{wall}} = \pm A_1 \left(\frac{2-\sigma}{\sigma} \right) \frac{\lambda}{\mu} \tau \bigg|_{wall} - A_2 \frac{\lambda^2}{\mu} \frac{\partial \tau}{\partial n} \bigg|_{wall} \qquad \textbf{(8.3)}$$

where the subscripts "gas" and "wall" refer to the velocity of the gas and wall, respectively, σ is the tangential momentum accommodation coefficient, λ is the mean free path, μ is the dynamic viscosity, τ is the shear stress, $\partial / \partial n$ is the derivative in the direction normal to the surface, and A_1 and A_2 are the first- and second-order slip coefficients, respectively. The (viscous) mean free path is defined as $\lambda = (\mu / p)(\pi \mathcal{R} T/2)^{1/2}$, where *p* is the pressure, $\mathcal{R}$ is the specific gas constant and *T* is the temperature. In the present study, the Knudsen number is defined in terms of the annular clearance between the shell and the confining inner (or outer) cylinder, i.e. $\text{Kn} = 2\lambda / (R_2 - R_1)$, where R_1 and R_2 are the radii of the stationary inner and outer cylinders, respectively.

The first-order term of the slip boundary condition in Eq. (8.3) was originally derived by Maxwell (1879). Subsequently, a second-order slip boundary condition for an arbitrary surface geometry was established by Sone (1969), Sone (2002) and Sone (2007) through a systematic asymptotic analysis of the Boltzmann equation and its boundary condition in half space for small Knudsen numbers. In the case of isothermal flow between two concentric cylinders, Sone's second-order slip boundary condition can be cast in the form of Eq. (8.3) but differs by the values of the first and second-order coefficients. The ± sign in front of the first-order term in Eq. (8.3) is determined by the direction of the normal vector pointing into the gas. In this particular confined geometry, the direction of the normal vector at the inner cylinder is positive (*r*-direction) while it is negative at the outer cylinder. The curvatures of the cylindrical surfaces also have opposite signs depending on whether the normal vector points towards the centre of curvature or not; the curvatures of the convex and concave surfaces are positive and negative, respectively. This makes the magnitude of the second-order slip coefficient, A_2, in Eq. (8.3) identical at both the convex and concave surfaces with a minus (-) sign in front. In addition, it should be

noted that the generic second-order boundary condition shown in Eq. (8.3) reduces to a form of second-order slip boundary condition for planar surfaces which has met with considerable success up to a Knudsen number as high as 0.4 (Colin et al., 2004; Hadjiconstantinou, 2003; Hadjiconstantinou, 2005a; Hadjiconstantinou, 2005b; Graur et al., 2009; Cercignani and Lorenzani, 2010; Perrier et al., 2011).

In the present study, the flow profiles are obtained for the fully diffusive case (i.e. $\sigma = 1$). The surface temperatures are assumed to be identical and specified as 273 ^{o}K. The first-order boundary condition could also be obtained by specifying the second-order slip coefficient in Eq. (8.3) to be zero (i.e. $A_2 = 0$).

The general solution of Eq. (8.1) for concave and convex side of the shell is obtained using generic nonplanar boundary condition as

$$\frac{u_{concave}(\bar{r})}{\Omega R_s} = \frac{\Gamma_1(r_1) r_s^3 \left(\bar{r}(r_s - r_1) + r_1\right)}{\Gamma_1(r_1) r_s^4 + \Gamma_2(r_s) r_1^4} - \frac{r_1^4 r_s^3}{\left(\bar{r}(r_s - r_1) + r_1\right)\left(\Gamma_1(r_1) r_s^4 + \Gamma_2(r_s) r_1^4\right)} \tag{8.4}$$

$$\frac{u_{convex}(\hat{r})}{\Omega R_s} = \frac{\Gamma_2(r_2) r_s^3 \left(\hat{r}(r_2 - r_s) + r_s\right)}{\Gamma_1(r_s) r_2^4 + \Gamma_2(r_2) r_s^4} + \frac{r_s^3 r_2^4}{\left(\hat{r}(r_2 - r_s) + r_s\right)\left(\Gamma_1(r_s) r_2^4 + \Gamma_2(r_2) r_s^4\right)} \tag{8.5}$$

$$\Gamma_1(x) = 4A_2 + 2A_1 x + x^2 \text{ and } \Gamma_2(x) = -4A_2 + 2A_1 x - x^2 \tag{8.6}$$

where $r_1 = R_1/\lambda$, $r_s = R_s/\lambda$ and $r_2 = R_2/\lambda$ are the non-dimensional radii; $\bar{r} = \left(r - R_1\right)/\left(R_s - R_1\right)$ and $\hat{r} = \left(r - R_s\right)/\left(R_2 - R_s\right)$ are the normalised radial distances. The slip coefficients in the present study are specified as $A_1 = 1.11$ and $A_2 = 0.61$ (Hadjiconstantinou, 2003; Hadjiconstantinou, 2005a).

8.3 Results and Discussions

The present study demonstrates the influence of the surface shape (i.e. convex/concave) on the velocity slip and formation of the Knudsen layer. In addition, the study reveals that there is a simple relationship between the shear stress exerted on the surface and the velocity defect in the Knudsen layer.

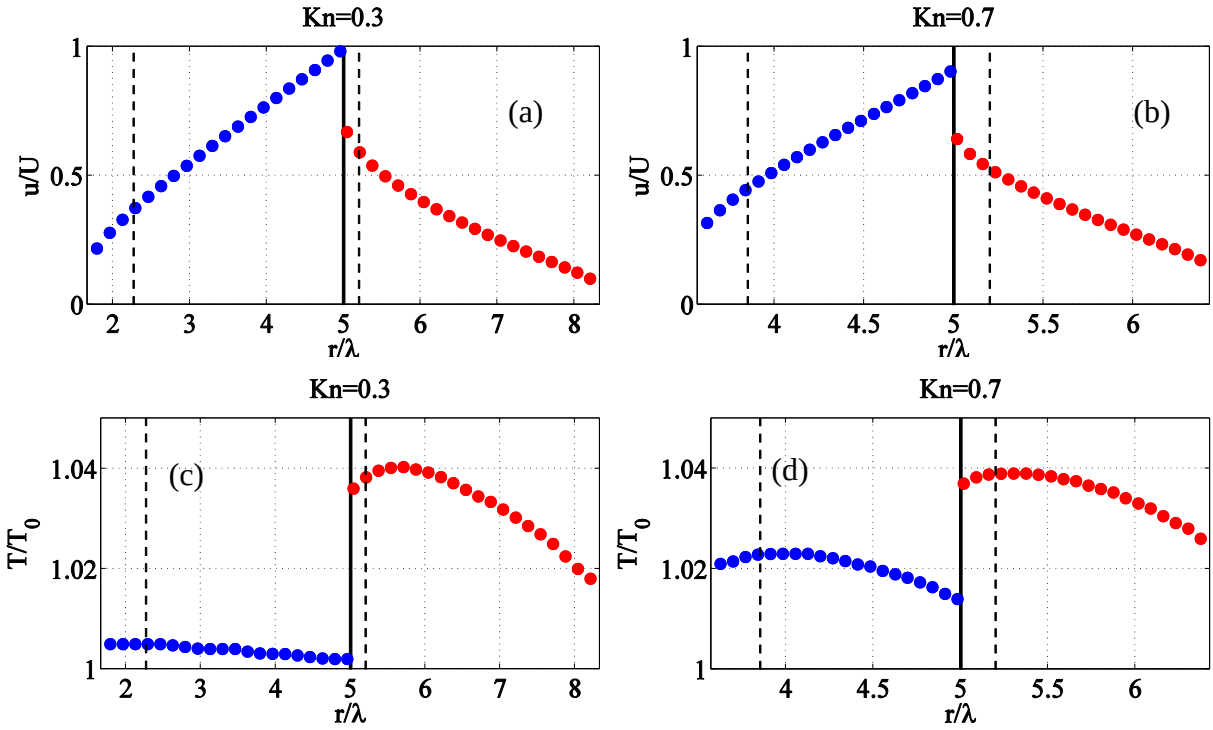

Figure 8.1: Comparison of velocity and temperature profiles over the concave and convex surfaces of a rotating cylindrical shell. Profiles obtained from the DSMC simulations. The shell is positioned between two stationary cylinders and has a radius of 5λ, where λ is the mean free path. The bold vertical lines in the middle of the figures represent the shell. The left- and right-hand side of the shell have concave and convex surfaces, respectively. The dashed lines demonstrate the approximate thickness of the S-layers; the thickness is specified as λ^2/R, where *R* is the radius of the convex cylinder.

The velocity and temperature profiles of rotating shell problem are shown in Figure 8.1. Profiles are obtained using DSMC simulations at a Mach number 0.5. The cylindrical shell is positioned in the middle of the annular gap and has a radius of 5λ, where λ is the mean free path. The bold vertical lines in the middle of figures represent the shell. The flows on the left- and right-hand side of the shell are driven by the concave and convex surfaces, respectively. The surfaces obviously have identical surface curvature and surface area. Therefore, Figure 8.1 clearly shows the role of surface shape (i.e. convex/concave) and profound effects of the S-layer over the convex surface. The S-layer is first described by Sone (1973) with a thickness proportional to the curvature of the surface. In the equivalent planar flow case or in the case of macroscopic flow with identical geometry, the amounts of slip and temperature jump would be equal on both surfaces.

Figures 8.1(a) and 8.1(b) show that the amounts of slip and temperature jump over the convex surface are larger than those over the concave surface. Although the S-layer is described originally as a thin sub-layer within the KL, the results show that the influence of the S-layer is rather significant. Furthermore, on the left hand-sides of the Figures 8.1(c) and 8.1(d), temperature increases from rotating concave surface to stationary convex surface. These temperature profiles demonstrate a behaviour as analogous to the velocity inversion phenomenon (Tibbs et al., 1997; Aoki et al., 2003, Yuhong et al., 2005).

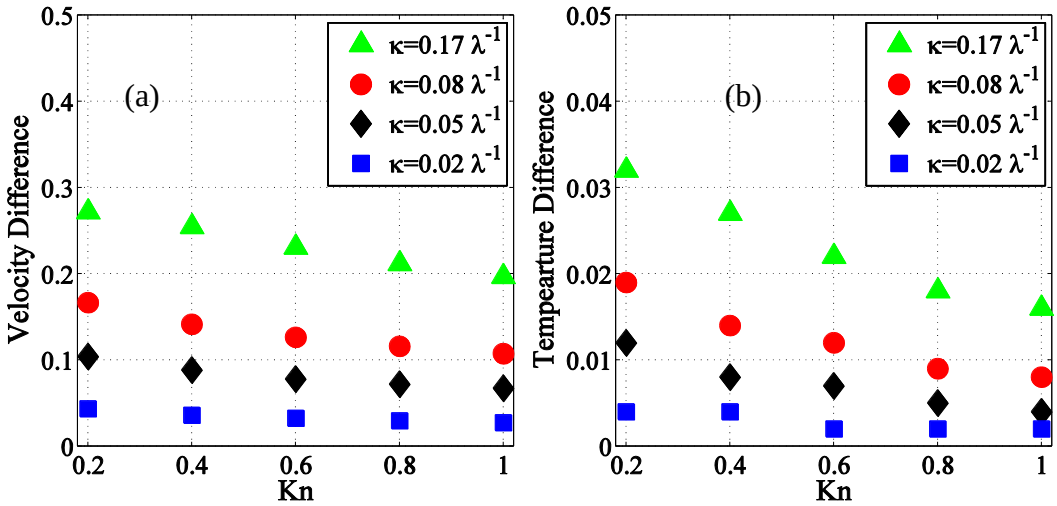

Figure 8.2: (a) Difference between (a) slip velocities, (b) temperature jumps over convex and concave surfaces of the shell. Radius of the shell is specified as 6λ, 12λ, 20λ and 50λ. The curvature, κ, is defined as the inverse of the shell radius. Slip velocities and temperature jumps are normalised by velocity and the temperature of the shell, respectively.

The variation of the slip velocity and temperature jumps differences are shown in Figure 8.2 for different values of the Knudsen number and shell curvature. The radius of the shell is specified as 6λ, 12λ, 20λ and 50λ. The curvature is defined as the inverse of the shell radius. Figure 8.2 shows that both slip velocity and temperature jump differences increase with curvature but interestingly decrease with the Knudsen number.

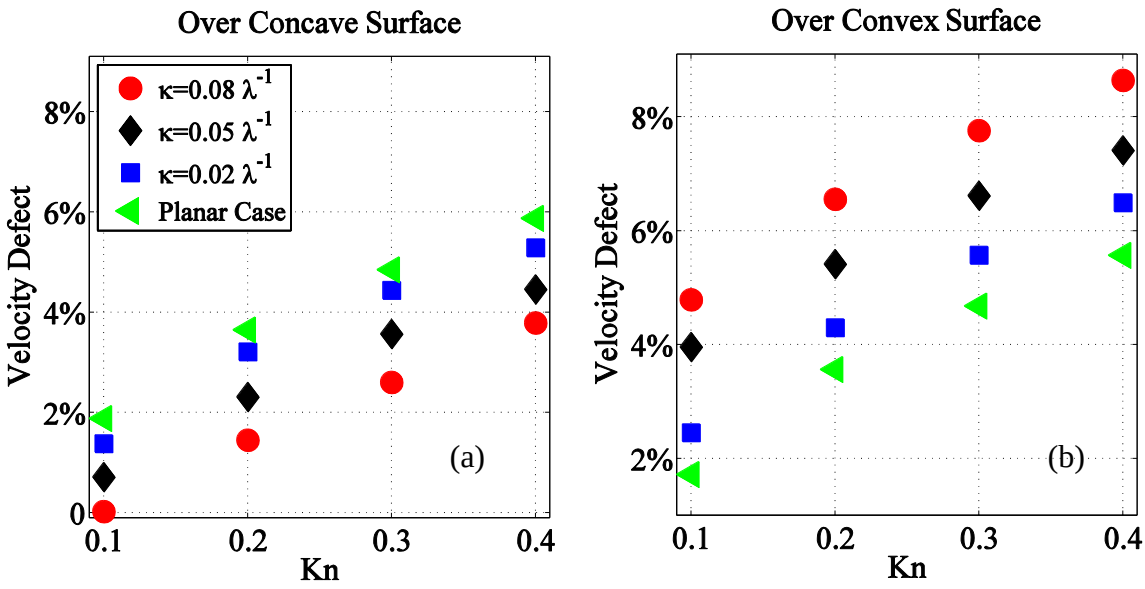

Figure 8.3: Effects of curvature on the velocity defect. The velocity defect is calculated as the difference between the normalised velocities obtained from the slip and DSMC solutions. (a) Velocity defect on the concave side, (b) Velocity defect on the convex side of the shell.

The KL manifests itself as velocity defect i.e. the difference between actual velocity and that predicted by slip models. Figure 8.3 shows the effects of curvature on the velocity defect at a Mach number of 0.12 (at 40 m/s wall velocity). Figure 8.3(a) and 3(b) demonstrate that velocity defect over concave surface decreases with curvature, while over concave surface it increases with curvature. This can be interpreted as an opposing effect of curvature over convex and concave surfaces. Velocity defect over convex side of the shell is also larger compared to that over concave side. Moreover, the velocity defect in the equivalent planar flow case defines a lower and an upper limit for the velocity defect over convex and concave surfaces, respectively.

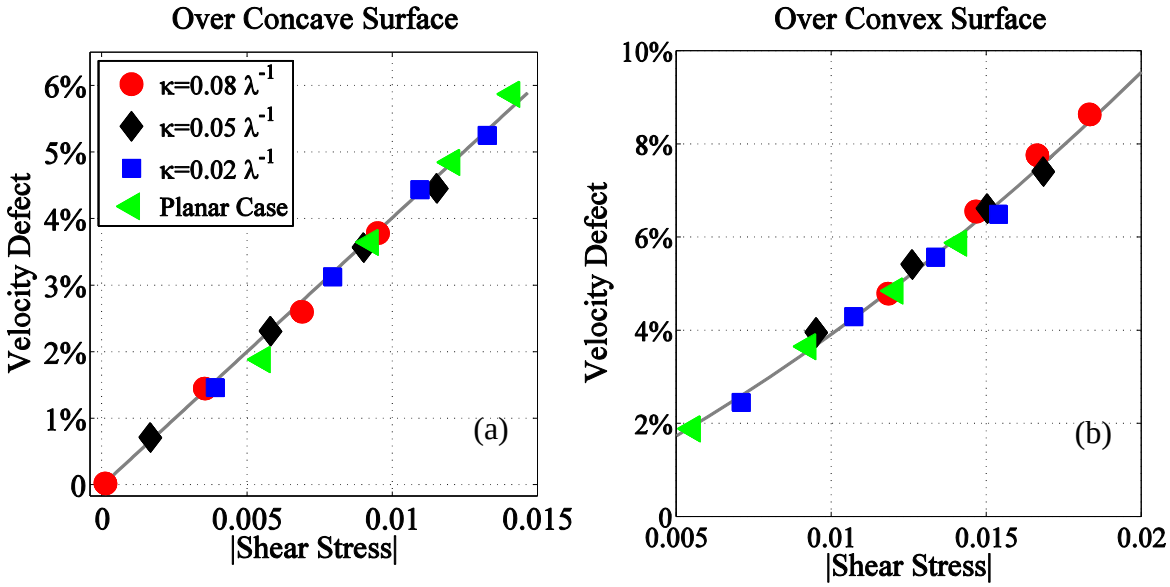

Figure 8.4: The velocity defect against the magnitude of the shear stress (a) at the concave and (b) at convex surface. The shear stress exerted on the cylinder surface is obtained by DSMC method. Identically shaped symbols from left to right represent the velocity defect at Knudsen numbers of 0.1, 0.2, 0.3, and 0.4, respectively.

Figure 8.4 demonstrates the important relations between shear stress and the velocity defect. The relation over concave surface is linear; however it is slightly nonlinear over convex surface. A linear function of shear stress has been fitted to the velocity defect with a slope of 0.472 in Figure 8.4(a). In this fit, the root mean square error (RMSE) is 0.00025 and the coefficient of determination is 99.72%. Identically shaped symbols from left to right correspond to the Knudsen numbers of 0.1, 0.2, 0.3 and 0.4, respectively. On the other hand, over convex surface, the relation is found as

$$\text{Velocity defect} = 0.365 \times |\text{Shear Stress}| + 1.2 \times |\text{Shear Stress}|^2 \qquad \textbf{(8.7)}$$

where the coefficient of determination is 99.18%.

8.4 Conclusions

This study has highlighted the profound effect of the surface shape (i.e. whether the surface is convex/concave) on the velocity and temperature profiles in rarefied cylindrical Couette flow and has illustrated that the temperature profiles can exhibit anomalous behaviour with the temperature increasing from a rotating concave surface to a stationary convex surface. This anomalous behaviour can be been explained by the role of the surface shape on the formation of the Knudsen layer. In

addition, the study shows that the S-layer, which is normally considered to be a thin sub-layer within the Knudsen layer, can have a profound effect on the flow over convex surfaces.

The study has revealed that there is a remarkable relationship between the velocity defect within the Knudsen layer and the shear stress exerted on the flow surface. The results demonstrate that the formation of the Knudsen layer is markedly different over concave and convex walls. It is shown that the relationship between the shear stress and the velocity defect is linear over a concave surface but slightly nonlinear in the presence of the S-layer over a convex surface.

Finally, the study has highlighted an important opposing effect of curvature on the velocity defect over concave and convex walls. A similar opposing effect on the velocity slip in liquid ^{3}He was proposed by Einzel et al. (1990) who predicted a monotonic increase in the degree of slip at a convex surface, and conversely, a monotonic decrease in the degree of slip at a concave surface, as the magnitude of the surface curvature increases. The direct simulation Monte Carlo results in the present study provide clear evidence that this opposing curvature effect on the velocity slip also occurs in rarefied gas flows over rotating cylindrical surfaces.

9. THE EFFECTS OF CURVATURE ON THE DEGREE OF BOUNDARY SLIP

The breakdown of the no-slip boundary condition at a fluid-solid interface and the importance of accounting for velocity slip have been recognized in micro/nanofluidics for many years. However, relatively few studies have investigated the phenomenon of slip flow over nonplanar surfaces, and consequently, the relationship between the curvature of the surface and the degree of boundary slip has not been understood sufficiently well. In the present chapter, a direct simulation Monte Carlo (DSMC) approach and a second-order velocity-slip Navier-Stokes continuum description have been used to address important issues related to the degree of boundary slip for gas-phase flow over curved surfaces. The chapter considers cylindrical Couette flow between two concentric cylinders and examines the curvature effects over the convex and concave surfaces. The results reveal that the degree of slip depends effectively on the surface shape (i.e. convex/concave), with the surface curvature having an opposing effect on the boundary slip over rotating concave and convex surfaces. The results also show that as surface curvature increases, the boundary slip becomes negligible over a concave surface while it becomes increasingly important over a convex surface. In addition, novel boundary slip formulae are proposed that can accurately predict the tangential velocities (and boundary slips) over convex and concave surfaces. These formulae are found to be in very good agreement with DSMC data for a range of accommodation coefficients and boundary curvatures. Using the corrected slip velocities at the inner and outer cylinders, the present chapter then reassesses the mechanism of the intriguing phenomenon of velocity inversion which has, until the present chapter, often been mistakenly attributed solely to the effects of boundary curvature.

9.1 Introduction

The breakdown of the no-slip boundary condition at a solid-fluid interface has been reported in many studies (Vinogradova, 1999; Zhu and Granick, 2002; Majumder et al., 2005; Holt et al., 2006; Whitby and Quirke, 2007) with the phenomenon being observed in micro-scale flows in both Newtonian and non-Newtonian liquids, and in gaseous flows. A theoretical understanding of boundary slip is clearly of great importance in the design of microfluidic devices. However, accounting for the complex interactions between the factors that affect the boundary slip (such as surface roughness, the wettability of the surface, the presence of nanobubbles/gaseous layers and the surface curvature) remains a formidable challenge, as reviewed by Neto et al. (2005) and Lauga et al. (2007).

The phenomenon of boundary slip is frequently encountered in microfluidic gas-phase flows. As the length scales of microfluidic devices are decreased towards the micro/nanoscale, the degree of slip can substantially alter the flow behaviour, highlighting the need for better descriptive models for quantifying the boundary slip. In addition, the presence of boundary slip can significantly influence the operating performance of a gas-phase micro-system and can have profound effects on convective heat transfer (Colin, 2012). In reality, most micro-devices contain nonplanar surfaces. Surprisingly, however, relatively little research has been conducted on slip effects over nonplanar walls. Understanding the slip behaviour and controlling the degree of slip in the presence of surface curvature is also essential for improving the reliability of gas-phase micro-systems.

The present chapter considers Couette flow between two concentric circular cylinders and examines two fundamental flow cases, namely: (a) a stationary outer (concave) cylinder and a rotating inner (convex) cylinder; and (b) a stationary inner cylinder and a rotating outer cylinder. The chapter demonstrates that there is a distinct “opposing” curvature effect between concave and convex surfaces. For example, the degree of slip over a convex surface is shown to increase as the curvature increases whilst the degree of slip over a concave surface decreases as the curvature is increased. Initially, the chapter utilizes a direct simulation Monte Carlo (DSMC) approach to investigate the velocity profiles within the annular clearance

between the cylinders. The chapter then proposes novel boundary slip formulae in order to predict the tangential velocities at the confining boundaries. A further analysis of the boundary slip over both convex and concave surfaces is then made using a Navier-Stokes continuum description with a generic second-order slip boundary condition. By using the corrected tangential velocities at the inner and outer cylinders, the present chapter reassesses the intriguing and highly non-intuitive phenomenon of *velocity inversion* which can sometimes occur when the outer cylinder is stationary and the inner cylinder is rotating. Under certain conditions, it is possible to obtain an inverted velocity profile where the velocity increases from the rotating inner cylinder to the stationary outer cylinder. This unusual phenomenon has often been attributed to the effects of curvature since it does not occur in the equivalent planar case of Couette flow between two parallel plates. The present chapter demonstrates that the phenomenon of velocity inversion cannot be explained solely by the effects of curvature, and instead, the results show that velocity inversion occurs due to an anomalous acceleration of the gas molecules near the concave surface of the outer cylinder as well as the presence of the S-layer which lowers the gas velocity at convex surface of the inner cylinder.

9.2 Navier-Stokes Description of the Problem

The present chapter considers Couette (shear-driven) flow between two concentric circular cylinders. The inner and outer cylinders have radii, R_1 and R_2, and rotate at angular velocities, Ω_1 and Ω_2, respectively. In a cylindrical-polar (r,θ) coordinate reference frame, the circumferential momentum expression of the incompressible Navier-Stokes equations can be written as

$$\frac{d^2u}{dr^2}+\frac{d}{dr}\left(\frac{u}{r}\right)=0 \qquad \textbf{(9.1)}$$

where u is the velocity in the tangential direction and r is the radial distance. The general solution of Eq. (9.1) can be written as

$$u(r)=C_1r+\frac{C_2}{r} \qquad \textbf{(9.2)}$$

where C_1 and C_2 are constants which are obtained using appropriate slip boundary conditions.

In the present chapter, we adopt a generic second-order slip boundary condition, formerly developed by Sone (1969) for an arbitrary surface shape, and we recast it for the case of isothermal flow over cylindrical surfaces. By incorporating Maxwell's first-order slip expression (Maxwell, 1879) into Sone's generalized second-order slip boundary condition, the velocity slip can be written in terms of the tangential shear stress as follows:

$$u_{slip} = u_{\text{gas}} - u_{\text{wall}} = \pm A_1 \frac{2-\sigma}{\sigma} \frac{\lambda}{\mu} \tau \bigg|_{wall} - A_2 \frac{\lambda^2}{\mu} \frac{\partial \tau}{\partial n} \bigg|_{wall} \quad \textbf{(9.3)}$$

where the subscripts "gas" and "wall" refer to the velocity of the gas and wall, respectively, A_1 and A_2 are the first- and second-order slip coefficients, σ is the (tangential momentum) accommodation coefficient, *u* is the tangential velocity, μ is the dynamic viscosity, τ is the tangential shear stress and $\partial/\partial n$ is the derivative in the normal direction to the surface. The ± sign in front of the first-order term in Eq. (9.3) is determined by the direction of the normal vector pointing into the gas. In this particular confined geometry, the direction of the normal vector at the inner cylinder is positive while it is negative at the outer cylinder. By incorporating the hard sphere intermolecular model, the mean free path can be defined according to Chapman-Enskog theory as $\lambda = 16/5\,\mu(2\pi\mathcal{R}T)^{-1/2}/\rho$ (Chapman and Cowling, 1970) where $\mathcal{R}$ the specific gas constant, ρ is the gas density and *T* is the temperature. In this chapter, we use the viscous mean free path definition provided by Maxwell (Maxwell, 1879), where the factor 16/5 is replaced by π. In the present chapter, the Knudsen number is defined in terms of the annular clearance between the cylinders, i.e. $\text{Kn} = \lambda/(R_2 - R_1)$. The generic second-order boundary condition in Eq. (9.3) can be shown to reduce to the conventionally-accepted second-order boundary condition at planar surfaces where it has been used with considerable success as reviewed in previous chapters.

The generic slip boundary condition in Eq. (9.3) can be written for the inner and outer cylinders as

$$u(R_1) = \Omega_1 R_1 + A_1 \frac{2-\sigma_1}{\sigma_1} \frac{\lambda}{\mu} \tau \Big|_{r=R_1} - A_2 \frac{\lambda^2}{\mu} \frac{\partial \tau}{\partial r} \Big|_{r=R_1} \tag{9.4}$$

$$u(R_2) = \Omega_2 R_2 - A_1 \frac{2-\sigma_2}{\sigma_2} \frac{\lambda}{\mu} \tau \Big|_{r=R_2} - A_2 \frac{\lambda^2}{\mu} \frac{\partial \tau}{\partial r} \Big|_{r=R_2} \tag{9.5}$$

where the shear stress, τ , is given by

$$\tau = \mu \left(\frac{\partial u}{\partial r} - \frac{u}{r} \right) \tag{9.6}$$

and σ_1 and σ_2 are the tangential momentum accommodation coefficients at the inner and outer cylinders, respectively.

The general solution of Eq. (9.1) using the generic second-order boundary conditions (9.4) and (9.5) can be obtained as

$$\begin{aligned} u(r^*) = & \frac{(\Gamma_1 (r^*(r_2 - r_1) + r_1)^2 - r_2^4 \sigma_1 \sigma_2) r_1^3}{(r^*(r_2 - r_1) + r_1)(\Gamma_1 r_1^4 + \Gamma_2 r_2^4)} \Omega_1 R_1 \\ & + \frac{(\Gamma_2 (r^*(r_2 - r_1) + r_1)^2 + r_1^4 \sigma_1 \sigma_2) r_2^3}{(r^*(r_2 - r_1) + r_1)(\Gamma_1 r_1^4 + \Gamma_2 r_2^4)} \Omega_2 R_2 \end{aligned} \tag{9.7}$$

with

$$\Gamma_1 = (2A_1 r_2 (\sigma_2 - 2) + (4A_2 + r_2^2)\sigma_2)\sigma_1 \tag{9.8}$$

$$\Gamma_2 = (2A_1 r_1 (\sigma_1 - 2) - (4A_2 + r_1^2)\sigma_1)\sigma_2 \tag{9.9}$$

and $r_1 = R_1/\lambda$ and $r_2 = R_2/\lambda$ are the nondimensional radii and $r^* = (r - R_1)/(R_2 - R_1)$ is the normalized radial distance, which lies between 0 and The first- and second-order slip coefficients in the present chapter are specified as $A_1 = 1.11$ and $A_2 = 0.61$. The boundary slip is defined as the difference between the gas velocity and the velocity of the surface.

9.3 Direct Simulation Monte Carlo (DSMC) Solution

The present chapter adopts the standard DSMC algorithm originally proposed by Bird (1994) except for a small modification in the calculation of the maximum collision number in a cell (see (Stefanov et al., 1998)) and implements the algorithm in a cylindrical geometry. The flow domain is divided into 100 uniformly-spaced cells with each cell containing approximately 100 simulation particles. The near wall velocities are obtained at a position extending 1/200 of the annular clearance from the cylinder surfaces, and the Navier-Stokes predictions are calculated and compared at the same locations. The DSMC simulations employ a hard sphere model for argon at STP conditions. For the initial part of the chapter (Figures 9.1 and 9.2), the circumferential velocity of the rotating cylinder was set to 95 m/s (corresponding to a Mach number of approximately 0.3). At this velocity, the DSMC simulations show less than a 2% variation in density and temperature throughout the flow domain for all the flow cases considered. This suggests that compressibility and thermal effects are not important for this particular problem, and this indicates that the incompressible Navier-Stokes description in Eq. (9.1) is valid. Subsequently, in the analysis of the phenomenon of velocity inversion (Figures 9.3 and 9.4), the circumferential velocity of the inner cylinder was set to $\Omega_1 R_1 = 40\,\mathrm{m/s}$ (corresponding to a Mach number of approximately 0.12). In this case, the DSMC simulations show less than a 1% variation in density and temperature throughout the flow domain.

The DSMC method numerically solves the full Boltzmann equation which describes rarefied gas behaviour at all Knudsen numbers. The idea behind the DSMC approach is the separation of the transport and collision parts of the Boltzmann equation, which are then solved sequentially each time interval. Each simulated particle represents a large number of molecules and therefore the DSMC method does not have to track a very large number of particles each time step. This is an important advantage of the DSMC method compared to molecular dynamics approaches. Another important feature of the DSMC method is that it is unconditionally stable.

The collision part of the Boltzmann equation is simulated stochastically using random numbers based on the molecular chaos assumption of the collision process.

The collision procedure introduces statistical noise which is of the order of $1/\sqrt{N}$, where *N* is the sample size (i.e. total number of particles in the simulation). In DSMC simulations, the flow domain needs to be divided into cells where typically each cell dimension is set to be less than one mean free path. The cell dimension is often specified as $\lambda/3$, since the flow properties should not vary inside a cell. However, in the present chapter, the cell size has been specified to be much smaller than the mean free path in order to obtain an accurate estimate of the gas velocity adjacent to the wall.

The present chapter implements the Maxwell (specular-diffusive) gas-wall interaction model in the DSMC simulations. In the Maxwell model, a proportional of the molecules, σ, are reflected diffusively from the surface while the remaining proportion, $1-\sigma$, are reflected specularly. Implementation of the specular reflection model in the DSMC method is straightforward. When a particle strikes a wall, the normal velocity component of the particle is simply reversed and the particle is directed back into the flow domain. The other velocity components remain unchanged. In the case of diffuse reflection, the reflected tangential velocity of the particle is considered to be uncorrelated with its impinging velocity and the particle bounces off the surface according to a Maxwellian velocity distribution.

9.4 Boundary Slip Corrections

The present chapter introduces corrections to the tangential velocities at both the concave and convex surfaces in order to accurately predict the degree of slip in the Navier-Stokes continuum formulation. These corrections have been developed through extensive research on the relationship between the velocity defect (which is the deviation between the actual velocity and that predicted by the Navier-Stokes equations) and the shear stresses at the walls. The boundary slips using these corrections are found to be in very good agreement with the DSMC data for a wide range of Knudsen numbers, accommodation coefficients and boundary curvatures.

When the inner cylinder is rotating and the outer cylinder is stationary (i.e. $\Omega_2 = 0$), the corrected tangential velocities at the inner and outer cylinders are

$$\frac{U_{in}}{\Omega_1 R_1} = \frac{u(0)}{\Omega_1 R_1} + (1+\kappa_1)^2(-0.211 + 0.12\,\tau_1^*)\tau_1^* \tag{9.10}$$

$$\frac{U_{out}}{\Omega_1 R_1} = \frac{u(1)}{\Omega_1 R_1} + 0.115\left(\frac{3\sigma_2 + 1}{\sigma_2(\sigma_2+1)}\right)\left(1 + \frac{(\chi-1)}{\chi^2}\right)\tau_2^* \tag{9.11}$$

where U_{in} and U_{out} are the corrected tangential velocities at the inner (convex) and outer (concave) cylinders, respectively, $u(0)$ and $u(1)$ are the Navier-Stokes velocities at the inner and outer cylinders obtained from Eq. (9.7), respectively, $\kappa_1 = 1/r_1 = \mathrm{Kn}(\chi - 1)$ is the nondimensional inner cylinder curvature, $\chi = R_2/R_1$ is the ratio between cylinder radii, and τ_1^* and τ_2^* are the nondimensional shear stresses calculated using Eqs. (9.6) and (9.7) at the inner and outer cylinders, respectively. The shear stresses are nondimensionalized as $\tau^* = \tau\lambda/(\mu U)$ where U is the tangential velocity of the moving surface.

Similarly, when the outer cylinder is rotating and the inner cylinder is stationary (i.e. $\Omega_1 = 0$), the corrected tangential velocities are

$$\frac{U_{out}}{\Omega_2 R_2} = \frac{u(1)}{\Omega_2 R_2} + 0.115\left(\frac{3\sigma_2 + 1}{\sigma_2(\sigma_2+1)}\right)\tau_2^* \tag{9.12}$$

$$\frac{U_{in}}{\Omega_2 R_2} = \frac{u(0)}{\Omega_2 R_2} + (1+\kappa_1)^2\left(1 + \frac{(\chi-1)}{\chi^2}\right)(-0.211 + 0.12\,\tau_1^*)\tau_1^* \tag{9.13}$$

The nondimensional boundary slips at the inner and outer cylinders are $1 - U_{in}/(\Omega_1 R_1)$ and $U_{out}/(\Omega_1 R_1)$, respectively, when the flow is driven by the inner cylinder, while the nondimensional boundary slips are $U_{in}/(\Omega_2 R_2)$ and $1 - U_{out}/(\Omega_2 R_2)$ when the flow is driven by the outer cylinder.

9.5 Results and Discussion

9.5.1 Boundary slip over curved surfaces

The chapter considers cylindrical Couette flow between two concentric circular cylinders and examines two fundamental flow cases, namely: (a) a stationary outer (concave) cylinder and a rotating inner (convex) cylinder; and (b) a stationary inner cylinder and a rotating outer cylinder. Figures 9.1 and 9.2 show the nondimensional gas velocities at the inner and outer cylinder surfaces as a function of the ratio between the cylinder radii, $\chi = R_2/R_1$, for each of the flow cases. The curvature is defined as the inverse of the cylinder radius and it can easily be shown that the curvatures of both cylinders increase with χ when the Knudsen number is kept constant. According to this curvature definition, the curvatures of the convex and concave surfaces are always positive, and curvature values, in fact, represent the *magnitude* of the curvature. In Figures 9.1 and 9.2, the black, blue and green colours denote the results for Knudsen numbers of 0.1, 0.3 and 0.5, respectively. The square-shaped symbols show the DSMC solution, the solid curves show the gas velocities calculated using the boundary slip corrections (Eqs. (9.10)-(9.13)), and the dashed curves show the predicted velocity without any corrections, as obtained from Eq. (9.7). The inner and outer cylinders are assumed to be fully diffusive (i.e. $\sigma_1 = \sigma_2 = 1$).

Figures 9.1 and 9.2 show that the corrected tangential velocities obtained using Eqs. (9.10)-(9.13) are in very good agreement with the DSMC data. The results demonstrate that the velocity predictions obtained using the corrected tangential velocities are significantly more accurate than the predictions without corrections. The results also indicate that the accuracy of the slip solution in Eq. (9.7) deteriorates as the curvature of the inner cylinder increases. It can therefore be concluded that conventional slip models should be used with caution when analyzing flows that involve convex surfaces due to the presence of the S-layer. The existence of the S-layer was first predicted for the case of thermal creep flow around a circular cylinder using asymptotic analysis of the Boltzmann-Krook-Welander (also called the BGK (Bhatnagar-Gross-Krook) model) equation. Sone (1973) found that the nondimensional tangential velocity is affected by a term of the order of Kn^2 at the

bottom of the Knudsen layer, and estimated the thickness of the S-layer to be of the order of $\lambda^2\kappa_1$, where κ_1 is the curvature of the convex surface. This implies that the S-layer is a thin sub-layer within the Knudsen layer, and suggests that the effects of the S-layer are only prominent within this near-wall region, with the effects vanishing outside the sub-layer (Sone, 2002; Sone, 2007). On the other hand, the results in Figures 9.1(a) and 9.2(a) reveal the presence of a *hydrodynamic* S-layer whose influence on the degree of slip is rather profound.

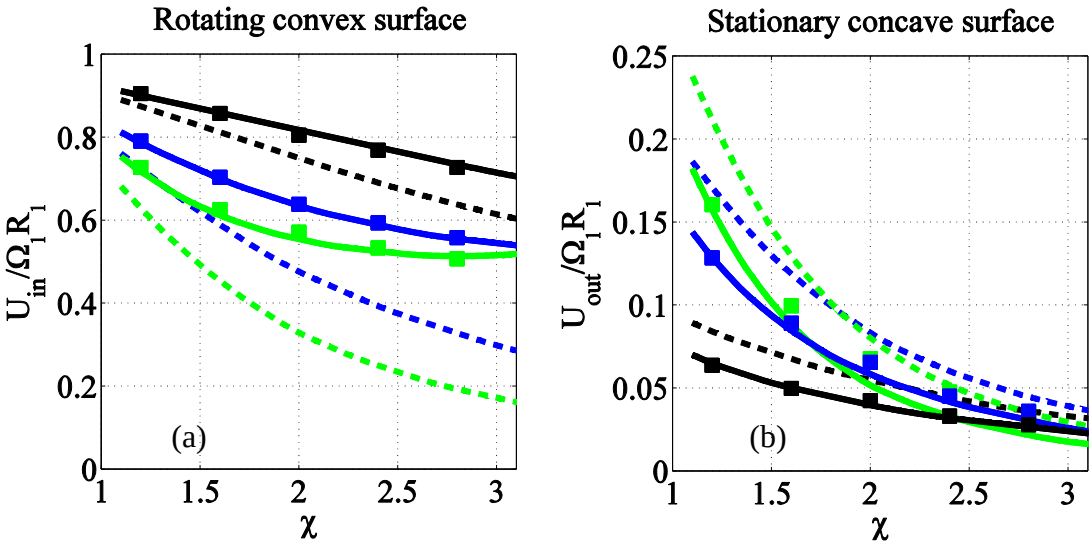

Figure 9.1: Nondimensional gas velocities at (a) the rotating inner (convex) cylinder, and (b) the stationary outer (concave) cylinder as a function of the ratio between the cylinder radii, $\chi = R_2/R_1$. The nondimensional boundary slip is $1-U_{in}/(\Omega_1 R_1)$ in Figure 9.1(a) and $U_{out}/(\Omega_1 R_1)$ in Figure 9.1(b). The black, blue and green colours denote Knudsen numbers of 0.1, 0.3 and 0.5, respectively. The square-shaped symbols show the DSMC solution, the solid curves show the gas velocities calculated using the boundary slip corrections, while the dashed curves show the predicted velocities obtained from Eq. (9.7) without corrections. The curvatures of both cylinders increase with χ. The accommodation coefficients are specified as unity on both cylinders (i.e. $\sigma_1 = \sigma_2 = 1$).

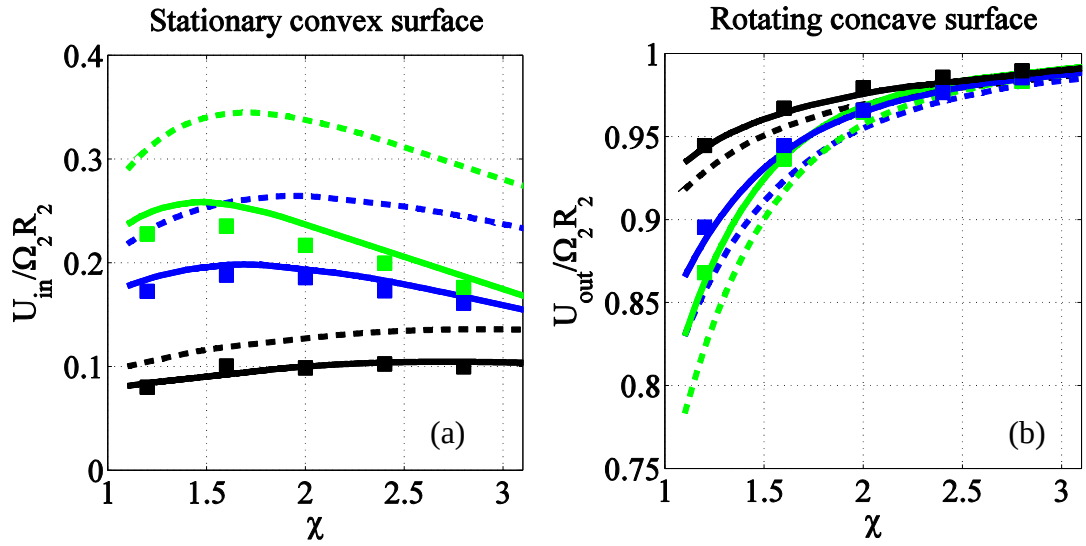

Figure 9.2: Nondimensional gas velocities at (a) the stationary inner (convex) cylinder, and (b) the rotating outer (concave) cylinder as a function of the ratio between the cylinder radii, $\chi = R_2/R_1$. The boundary slip is $U_{in}/(\Omega_2 R_2)$ in Figure 9.2(a) and $1-U_{out}/(\Omega_2 R_2)$ in Figure 9.2(b). See the caption in Figure 9.1 for further details.

The present chapter reveals that the degree of slip effectively depends on the surface shape. For example, the degree of slip becomes increasingly significant over a convex surface as the curvature increases while the boundary slip over a concave surface becomes negligible as the curvature increases. In the planar limit, $\chi = R_2/R_1 \to 1$, the boundary slips at both surfaces are equal but as curvature increases, the degree of slip over the convex surface (Figures 9.1(a) and 9.2(a)) becomes increasingly larger than the slip over the concave surface (Figures 9.1(b) and 2(b)). The boundary slip reaches almost 50% of the velocity of the rotating inner cylinder in Figure 9.1(a) while it is less than 20% of the velocity of the rotating outer cylinder and constantly decreases with curvature as shown in Figure 9.2(b). This demonstrates the profound effects of surface shape on the flow behaviour.

In addition to the important relationship between the magnitude of the shear stress and the degree of slip, our theoretical approach suggests that when the magnitude of the shear stress tends to zero, the boundary slip must be negligible at any Knudsen number. In fact, this is the case for a gas flow inside a rotating cylinder (in the limit of vanishing inner cylinder radius, $R_1 \to 0$), where it can easily be shown that the Navier-Stokes shear stress is zero (i.e. $\tau = 0$). For this particular case of flow inside a rotating cylinder (i.e. flow driven by a concave surface), Maxwell (1877) formally

predicted zero boundary slip for all Knudsen numbers, and this has subsequently been confirmed by Soga and Ooue (2002) using both kinetic theory and the DSMC method.

When modelling the flow behaviour in gas-phase microdevices, the Knudsen layer which extends just over one mean free path from the wall, is crucially important. The Knudsen layer manifests itself as a significant boundary slip at the wall, and the formation of the Knudsen layer and the transport properties within this layer are of great importance to the overall flow characteristics. When the Knudsen number increases beyond Kn ~ 10^{-3}, the growing influence of the Knudsen layer causes a noticeable boundary slip at a planar wall (Loyalka, 1975; Reese and Zhang, 2009; Zhang et al., 2006). It is commonly thought that the Knudsen layer is equally effective over nonplanar surfaces. However, the present results in Figures 9.1(b) and 9.2(b) show that the formation of the Knudsen layer can sometimes be negligible over a concave surface. It is important to note that the Knudsen layer will exist while the flow is developing towards the steady-state due to the non-zero shear stress, even though it is completely absent at steady-state (Dinler et al., 2011b). On the other hand, without the influence of the outer cylinder surface, i.e. when flow is driven solely by a convex inner cylinder, Eq. (9.7) in limit of $R_2 \to \infty$ gives

$$u(\hat{r}) = \frac{\sigma_1}{\hat{r}(2A_1\kappa_1(2-\sigma_1)+(1+4A_2\kappa_1^2)\sigma_1)}\Omega_1 R_1 \qquad \textbf{(9.14)}$$

where $\hat{r} = r/R_1$ is the nondimensional radial distance away from the cylinder and $\kappa_1 = \lambda/R_1$ is the nondimensional cylinder curvature. The boundary slip is then

$$1-u(1)/(\Omega_1 R_1) = 1-\frac{\sigma_1}{2A_1\kappa_1(2-\sigma_1)+(1+4A_2\kappa_1^2)\sigma_1} \qquad \textbf{(9.15)}$$

The denominator of Eq. (9.14) monotonically increases with curvature and thus the gas velocity in Eq. (9.14) constantly decreases at the convex surface as the curvature is increased. As a result, the boundary slip in Eq. (9.15) monotonically increases and the S-layer is capable of being increasingly influential with curvature.

9.5.2 The opposing effect of curvature and the phenomenon of velocity inversion

The boundary slip predictions obtained from both the DSMC and corrected slip solutions show that the degree of slip over a rotating convex surface increases with curvature. Conversely, the degree of slip over a concave surface decreases as the curvature increases. This suggests that surface curvature has an opposing effect on the boundary slip over concave and convex surfaces. A similar opposing effect on the slip lengths was first described by Einzel et al. (1990) for the flow of liquid helium (^{3}He) over curved walls covered by superfluid ^{4}He. The present results show that the opposing effect of curvature on boundary slip also occurs for rarefied gas flows, as can be seen in Figures 9.1(a), 9.1(b) and 9.2(b). However, in this particular chapter, the opposing effect is not present at the stationary inner (convex) cylinder in Figure 9.2(a) beyond $\chi \approx 1.5$ for Kn=0.3 and Kn=0.5.

The breakdown of the opposing effect for flow between two concentric rotating cylinders may be related to the phenomenon of velocity inversion. This intriguing phenomenon can only be observed for the specific case of a rotating inner cylinder and a stationary outer cylinder (Tibbs et al., 1997; Aoki et al., 2003; Yuhong et al., 2005; Jung, 2007; Kim, 2009; Guo et al., 2011). Under certain conditions of rarefaction (for gas flows) or with highly hydrophobic surfaces (for liquid flows), it is possible to obtain an inverted velocity profile where the velocity of the fluid anomalously increases from the moving inner cylinder to the stationary outer cylinder. In other words, the phenomenon of velocity inversion occurs when the velocity of the fluid at the outer cylinder exceeds the velocity at the rotating inner cylinder. In the case of gas flows, the phenomenon of velocity inversion was originally demonstrated by Tibbs et al. (1997) using a direct simulation Monte Carlo method. Their chapter revealed that velocity inversion occurs when the Knudsen number is relatively high and the accommodation coefficient of the outer cylinder is relatively low. This unusual phenomenon has often been attributed to the effects of curvature since it does not occur in the equivalent planar case of Couette flow between two parallel plates.

Using the corrected tangential velocities at the inner and outer cylinders, the occurrence of velocity inversion has been investigated for varying values of the Knudsen number and the outer cylinder accommodation coefficient. For the results

presented in Figures 9.3-9.5, each DSMC cell contains approximately 1000 simulation particles and the circumferential velocity of the inner cylinder is specified to be $\Omega_1 R_1 = 40\,\mathrm{m/s}$ (corresponding to a Mach number of approximately 0.12). In these simulations, the inner cylinder surface is assumed to be fully diffusive (i.e. $\sigma_1 = 1$). However, a number of DSMC simulations have considered cases where the value of the inner accommodation coefficient is less than unity. The results show that the inner accommodation coefficient has very little impact on the occurrence of velocity inversion as previously reported by Yuhong et al. (2005). When the inner cylinder accommodation coefficient is reduced, the DSMC data suggest that the critical accommodation coefficient at the onset of velocity inversion decreases very slightly.

Figures 9.3 and 9.4 show the variation of the nondimensional gas velocities near the inner and outer cylinder surfaces, respectively, as a function of the ratio between the cylinder radii, $\chi = R_2/R_1$ for Knudsen numbers of 0.15, 0.25 and 0.35. As shown in Figures 9.3 and 9.4, the boundary slip corrections obtained using Eqs. (9.10) and (9.11) significantly improve the accuracy of the boundary slip predictions which are shown to be in very good agreement with the DSMC data. Figures 9.4(a) and 9.4(b) show that the opposing curvature effect is not present at low values of the outer accommodation coefficient, since the boundary slip at the outer cylinder unexpectedly increases with curvature at moderate values ($\chi < 2$). The increase in the gas velocity near the outer cylinder disappears with increasing values of the outer accommodation coefficient. Since velocity inversion occurs when the gas velocity near the outer cylinder exceeds the gas velocity near the inner cylinder, a comparison of the gas velocities in Figures 9.3(a) and 9.4(a) suggests that velocity inversion occurs due to an abnormal acceleration of gas molecules at the outer cylinder while the presence of the S-layer lowers the gas velocity at the inner cylinder.

Figure 9.5 illustrates the conditions that will lead to velocity inversion for various values of the outer cylinder accommodation coefficient and the ratio between the cylinder radii, $\chi = R_2/R_1$. Figure 9.5 is plotted using the boundary slip formulae presented in Eqs. (9.10) and (9.11), and illustrates that the critical accommodation coefficient has a maximum value around $\chi \approx 2$. In addition, Figure 9.5 reveals that away from a curvature of $\chi \approx 2$, velocity inversion may not occur and the outer cylinder must have a smaller accommodation coefficient in order to lead to velocity inversion. The results show that the phenomenon of velocity inversion cannot be explained solely by the effects of curvature, although the effects of curvature do have an important role in the mechanism of velocity inversion. Figure 9.5 shows that a linear relationship between the effects of curvature and the occurrence of the velocity inversion cannot be made.

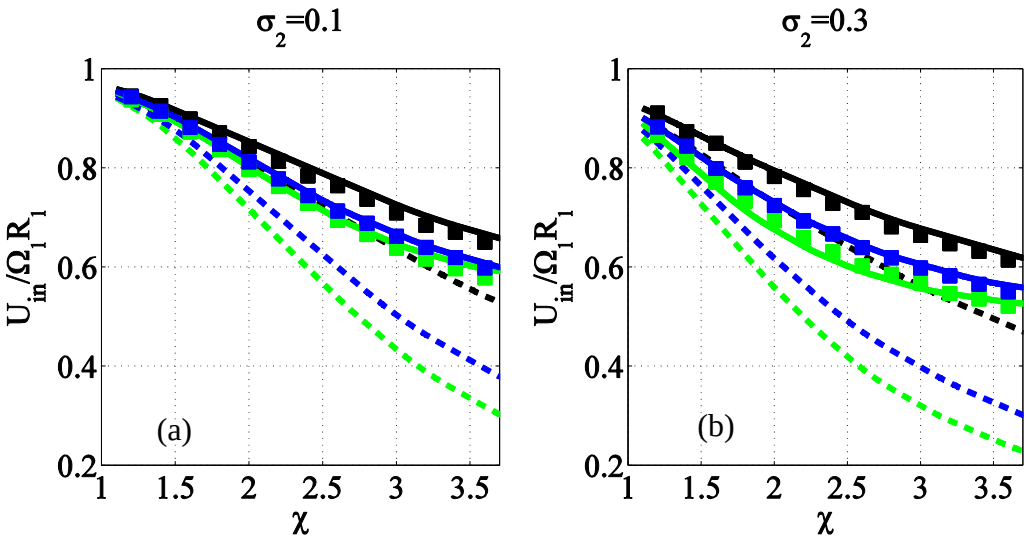

Figure 9.3: Nondimensional gas velocity near the convex (inner) rotating cylinder surface as a function of the ratio of the cylinder radii, $\chi = R_2/R_1$. The boundary slip is the difference between the nondimensional gas velocity and unity (i.e. $1-U_{in}/(\Omega_1 R_1)$). The black, blue and green colours denote Knudsen numbers of 0.15, 0.25 and 0.35, respectively. The square-shaped symbols show the DSMC solution, the solid curves show the gas velocities at the inner cylinder calculated using the boundary slip corrections, while the dashed curves show the predicted velocity without any corrections, as obtained from Eq. (9.7). The curvature of both cylinders increases with χ. The inner accommodation coefficient is unity (i.e. $\sigma_1 = 1$) and the outer accommodation coefficient is specified as (a) $\sigma_2 = 0.1$, and (b) $\sigma_2 = 0.3$.

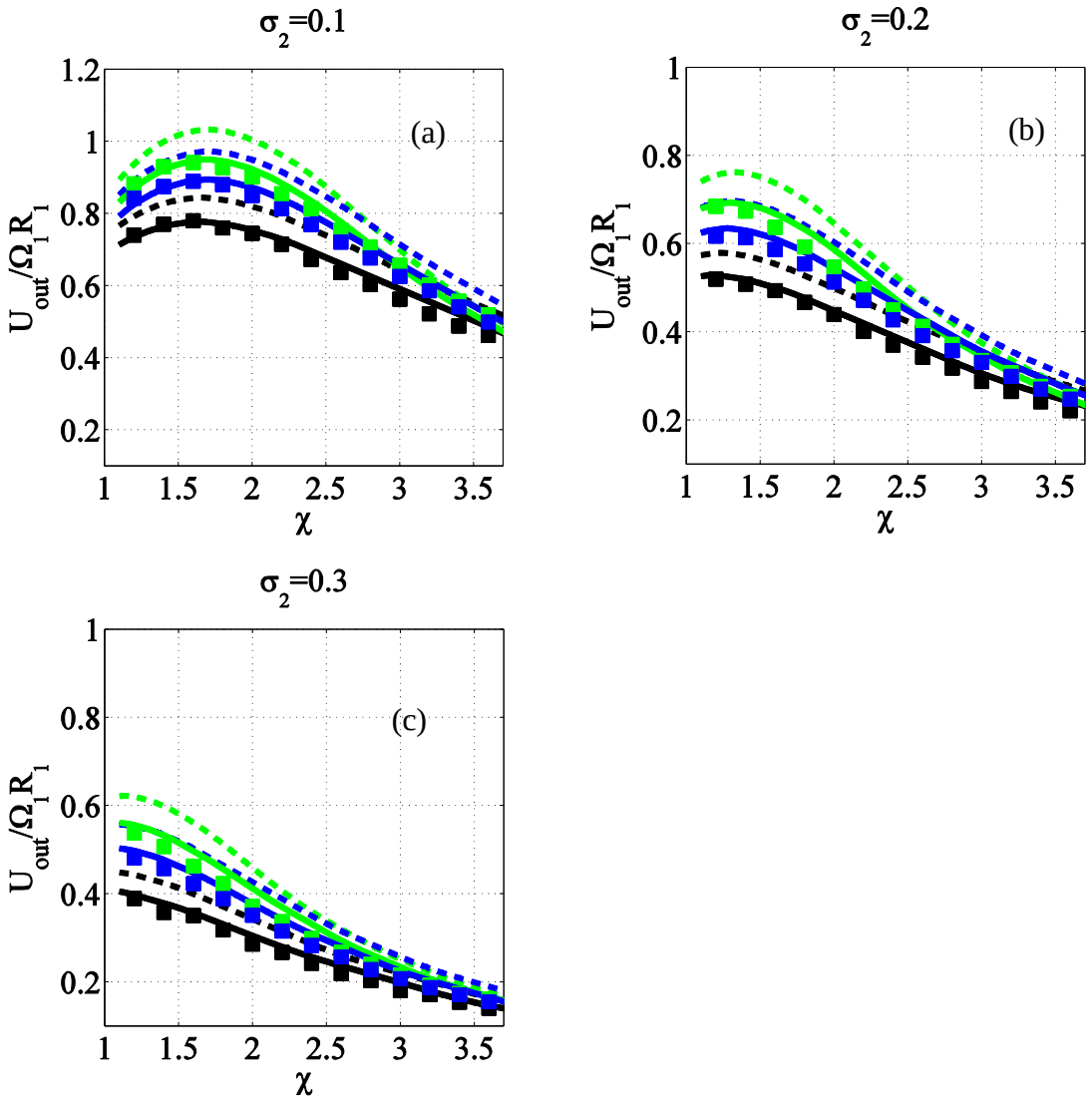

Figure 9.4: Nondimensional gas velocity (i.e. boundary slip) near the outer cylinder surface as a function of the ratio of the cylinder radii, $\chi = R_2/R_1$. The outer accommodation coefficient is specified as (a) $\sigma_2 = 0.1$, (b) $\sigma_2 = 0.2$ and (c) $\sigma_2 = 0.3$. See the caption in Figure 9.3 for further details

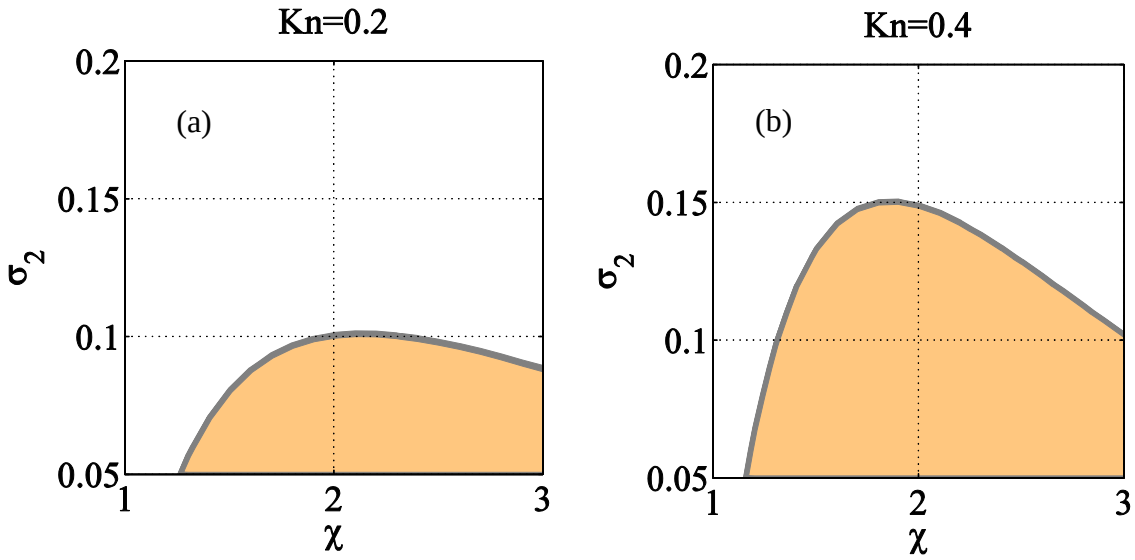

Figure 9.5: Occurrence of velocity inversion for varying values of the outer cylinder accommodation coefficient, σ_2, and the ratio between the cylinder radii, $\chi = R_2/R_1$. The shaded areas illustrate the flow conditions where velocity inversion occurs. (a) Kn=0.2 and (b) Kn=0.4.

The present results suggest that the phenomenon of velocity inversion is associated with an unusual increase in the boundary slip near the outer cylinder. This increase appears when the outer cylinder accommodation coefficient is small. The results also show that the effects of the S-layer play an important role in the occurrence of velocity inversion. The presence of the S-layer causes a significant boundary slip at the inner rotating cylinder as the curvature increases which lowers the gas velocity near the inner cylinder (i.e. boundary slip increases). This eventually allows the gas velocity at the outer cylinder to exceed the gas velocity at the inner cylinder. However, the increase in the slip obviously decreases the gas velocity near the rotating inner cylinder and eventually not enough momentum is transferred to the gas within the annular gap between the cylinders. This prevents the gas molecules near the outer cylinder from being accelerated enough to exceed the velocity at the inner cylinder and explains why, beyond a certain curvature value, the increase in the boundary slip at the outer cylinder disappears and velocity inversion is less likely to occur. On the other hand, for the case when the outer cylinder is rotating and the inner cylinder is stationary, the DSMC data show that the gas velocity near the rotating outer cylinder monotonically increases with curvature (i.e. boundary slip decreases). As a consequence, the gas velocity at the inner cylinder can never exceed

the gas velocity at the outer cylinder and the phenomenon of velocity inversion cannot occur in this particular case.

9.6 Conclusions

The present chapter has used a direct simulation Monte Carlo approach and a generic second-order slip Navier-Stokes continuum description to investigate rarefied Couette flow between two concentric rotating cylinders. The chapter employs a second-order slip boundary condition in order to extend the validity of the Navier-Stokes equations to higher Knudsen numbers. Comparison of the DSMC and the Navier-Stokes slip solution indicate that the accuracy of the slip boundary condition deteriorates over convex surfaces and should be used with caution due to the existence of the S-layer. A series of boundary slip correction formulae, which suggest a direct relationship between the boundary slip and the shear stress exerted on the wall, have been proposed in order to predict the degree of boundary slip accurately. These formulae have been found to be in excellent agreement with the DSMC data up to Kn=0.5. The effects of curvature and the surface shape, and the intriguing phenomenon of velocity inversion have then been investigated using these boundary slip corrections.

The results of the chapter reveal that the degree of slip depends essentially on the surface shape, with the surface curvature having an opposing effect on the boundary slip over rotating concave and convex surfaces. The results show that as the surface curvature increases, the boundary slip becomes negligible over a concave surface while it becomes increasingly influential for the flow over a convex surface. This dramatic effect of the surface shape on boundary slip, namely, the opposing effect of curvature, has been investigated in detail. It is shown that for rarefied Couette flow between two concentric cylinders, the opposing effect can sometimes break down over a stationary cylinder or over a rotating cylinder with a low accommodation coefficient.

The present chapter also reassesses the intriguing and highly non-intuitive phenomenon of velocity inversion which can occur when the inner cylinder is rotating and the outer cylinder is stationary. Under certain conditions, namely when

the Knudsen number is relatively high and the accommodation coefficient of the outer cylinder is relatively low, it is possible to obtain an inverted velocity profile where the velocity increases from the rotating inner cylinder to the stationary outer cylinder. This unusual phenomenon has often been attributed to the effects of curvature since it does not occur in the equivalent planar case of Couette flow between two parallel plates. However, the present chapter demonstrates that the phenomenon of velocity inversion cannot be explained solely by the effects of curvature. Instead, the results show that velocity inversion occurs due to an acceleration of the gas molecules at the outer cylinder associated with the breakdown of the opposing effect. The chapter also shows that the presence of the hydrodynamic S-layer at the convex surface plays an important role in the velocity inversion mechanism.

REFERENCES

Albertoni, S., Cercignani, C., and Gotusso, L. (1963). Numerical evaluation of the slip coefficient, *Phys. Fluids*, **6**, 993-996.

Aoki, K., Yoshida, H., and Nakanishi, T. (2003). Inverted velocity profile in the cylindrical Couette flow of a rarefied gas, *Phys. Rev. E*, **68**, 016302.

Baaquie, B.E., and Willeboordse, F.H. (2009). *Exploring Integrated Science* (CRC Press, 1st Edition).

Bailey, C.L., Barber, R.W., Emerson, D.R., Lockbery, D.A., and Reese, J.M. (2005). A critical review of the drag force on a sphere in the transition flow regime, *24th Rarefied Gas Dynamics Symposium*.

Barber, R.W., and Emerson, D.R. (2006). Challenges in modeling gas-phase flow in microchannels: from slip to transition, *Heat Transfer Eng.*, **27**, 3-12.

Bhatnagar, P.L., Gross, E.P., and Krook, M. (1954). A model for collision processes in gases. I. Small amplitude processes in charge and neutral one-component systems, *Phys Rev*, **94**, 511–525.

Bird, G.A. (1994). *Molecular Gas Dynamics and the Direct Simulation of Gas Flows*, Oxford Press.

Cao, B.Y., Sun, J., Chen, M., and Guo, Z.Y. (2009). Molecular momentum transport at fluid-solid interfaces in MEMS/NEMS: a review, *Int. J. Mol. Sci.*, **10**, 4638-4706.

Carslaw, H.S., and Jaeger, J.C. (1963). *Operational Methods in Applied Mathematics*, New York, Dover Publications.

Cengel, Y.A. (2006). *Heat and Mass Transfer: A Practical Approach*, McGraw-Hill.

Cercignani, C., and Daneri, A. (1963). Flow of a rarefied gas between two parallel plates, *J. Applied Physics*, **34**, 3509–3513.

Cercignani, C., and Lampis, M. (1971). Kinetic models for gas-surface interactions, *Transp. Theory Stat. Phys.*, **1**, 101-114.

Cercignani, C. (2000). *Rarefied Gas Dynamics: From Basic Concepts to Actual Calculations*, Cambridge University Press, Cambridge.

Cercignani, C., and Lorenzani, S. (2010). Variational derivation of second-order slip coefficients on the basis of the Boltzmann equation for hard-sphere molecules, *Phys. Fluids*, **22**, 062004.

Chaaf, S.A., and Chambre, P.L. (1961). *Flow of Rarefied Gases, Princeton University Press*, Princeton Press.

Chapman, S., and Cowling, T.G. (1970). *The Mathematical Theory of Non-Uniform Gases* (3rd ed., Cambridge University Press, Cambridge).

Chu, C.K. (1965). Kinetic-theoretic description of the formation of a shock wave, *Phys. Fluids*, **8,** 12.

Colin, S. (2012). Gas Microflows in the Slip Flow Regime: a Critical Review on Convective Heat Transfer, *Transactions-American Society of Mechanical Engineers Journal of Heat Transfer*, **134**, 020908.

Colin, S., Lalonde, P., and Caen, R. (2004). Validation of a second-order slip flow model in rectangular microchannels, *Heat Transfer Eng.*, **25**, 23-30.

Deissler, R.G. (1964). An analysis of second-order slip-flow and temperature-jump boundary conditions for rarefied gases, *Int. J. Heat and Mass Transfer*, **7**, 681–694.

Dinler, A., Barber, R.W., and Emerson, D.R. (2010a). Can the validity of slip models be extended into the transition regime?, *The Proceedings of 2nd Workshop of GASMEMS*, Les Embiez, France July 9-10.

Dinler, A., Barber, R.W., and Emerson, D.R. (2010b). The effects of curvature on nonplanar oscillatory microflows, in Proceedings on CDROM of 2nd European Conference on Microfluidics (μFlu'10), Toulouse, France, S. Colin and G. L. Morini, Eds. SHF (Publisher), ISBN 978-2-906831-85-8, μFLU2010-110:1-8.

Dinler, A., Barber, R.W., and Emerson, D.R. (2011a). The role of the S-layer on the accuracy of slip models, in Proceedings on CDROM of 3rd International GASMEMS Workshop (GASMEMS11), Bertinoro, Italy, GASMEMS11-5:1-6.

Dinler, A., Barber, R.W., and Emerson, D.R., and Orucoglu, K. (2011b). Does the Knudsen layer exist over convex surfaces, Proceedings of the International Symposium on Thermal and Materials Nanoscience and Nanotechnology, ICHMT Digital Library, Begell House, May 29-June 3, Antalya, Turkey, pp. 1-8.

Doi, T. (2010). Numerical analysis of oscillatory Couette flow of a rarefied gas on the basis of the linearized Boltzmann equation, *Vacuum*, **84**, 734.

Einzel, D., Panzer, P., and Liu, M. (1990). Boundary condition for fluid flow: curved or rough surfaces, *Phys. Rev. Lett.*, **64**, 2269–227.

Emerson, D.R., Gu, X.J., Stefanov, S.K., Yuhong, S., and Barber, R.W. (2007). Nonplanar oscillatory shear flow: from the continuum to the free-molecular regime, *Phys. Fluids*, **19**, 107105.

Fan, J., and Shen, C. (2001). Statistical simulation of low-speed rarefied gas flows. *J. Comput. Phys.*, **167**, 393-412.

Frangi, A., Ghisi, A., and Coronato, L. (2009). On a deterministic approach for the evaluation of gas damping in inertial MEMS in the free-molecule regime, Sens. Actuators A, **149**, 21.

Gad-El-Hak, M. (1995). Questions in Fluid Mechanics: Stokes' Hypothesis for a Newtonian, Isotropic Fluid, *Trans. ASME, J. Fluids Engineering*, **117**, 3-5.

Gad-El-Hak, M. (1999). The Fluid Mechanics of Microdevices-The Freeman Scholar Lecture, Trans. *ASME, J. Fluids Engineering*, **121**, 5-33.

Goldstein, S. (1932). Some two-dimensional diffusion problems with circular symmetry, *Proc. London Math. Soc.*, **1**, 51-88.

Glaeske, H.J., Prudnikov, A.P., and Skornik, K. (2006). *Operational Calculus and Related Topics*, Boca Raton, FL, Chapman & Hall/CRC.

Grad, H. (1949). On the Kinetic Theory of Rarefied Gases, *Communications on Pure and Applied Mathematics*, **2**, 331–407.

Graur, I.A., Perrier, P., Ghozlani, W., and Meolans, J.G. (2009). Measurements of tangential momentum accommodation coefficient for various gases in plane microchannel, *Phys. Fluids*, **21**, 102004.

Graur, I.A., and Polikarpov, A.P. (2009). Comparison of different kinetic models for the heat transfer problem, *Heat Mass Transfer*, **46**, 237-244.

Gu, X.J., and Emerson, D.R. (2011). Modeling oscillatory flows in the transition regime using a high-order moment method, *Microfluid Nanofluid*, **10**, 389.

Gu, X.J., Emerson, D.R., and Tang, G.H. (2010). Analysis of the slip coefficient and defect velocity in the Knudsen layer of a rarefied gas using the linearized moment equations, *Phys Rev E*, **81**, 016313.

Guo, Z., Shi, B., and Zheng, C. (2011). Velocity inversion of micro cylindrical Couette flow: a lattice Boltzmann study, *Comput. Math. Appl.*, **61**, 3519–3527.

Haddad, O.M., Al-Nimr, M.A., and Abuzaid, M.M. (2005). The effect of frequency of fluctuating driving force on basic gaseous micro-flows, *Acta Mech.*, **179**, 249.

Hadjiconstantinou, N.G. (2003). Comment on Cercignani's second-order slip coefficient, *Phys. Fluids*, **15**, 2352-2354.

Hadjiconstantinou, N.G. (2005). Validation of a second-order slip model for dilute gas flows. *Microscale Thermophysical Engineering*, **9**, 137-153.

Hadjiconstantinou, N.G. (2005). Oscillatory shear-driven gas flows in the transition and free-molecular-flow regimes, *Phys. Fluids*, **17**, 100611.

Harris, S. (2004). *An Introduction to the Theory of the Boltzmann Equation*, Dover.

Holt, J.K., Park, H.G., Wang, Y., Stadermann, M., Artyukhin, A. B., Grigoropoulos, C.P., Noy, A., and Bakajin. O. (2006). Fast mass transport through sub-2-nanometer carbon nanotubes, *Science*, **312**, 1034-1037.

Homolle, T.M.M., and Hadjiconstantionu, N.G. (2007). Low-variance deviational simulation Monte Carlo, *Phys. Fluids*, **19**, 041701.

Hsia, Y.T., and Domoto, G.A. (1983). An experimental investigation of molecular rarefaction effects in gas lubricated bearings at ultra-low clearances, *Trans. ASME, J. Lubrication Tech.*,**105**, 120–130.

Jeffreys, H. and Jeffreys, B. (1999). *Methods of Mathematical Physics* (Cambridge University Press, Cambridge).

Jung, Y. (2007). Velocity inversion in nanochannel flow, *Phys. Rev. E*, **75**, 051203.

Karniadakis, G.E., Beskok, A. and Aluru N. (2005). *Microflows and Nanoflows: Fundamentals and Simulation* (Springer, 2nd Edition).

Kim, S. (2009). Slip velocity and velocity inversion in a cylindrical Couette flow, *Phys. Rev. E*, **79**, 036312.

Knudsen, M. (1915). The cosine law in the kinetic theory of gases, *Annalen der Physik*, **48**, 1113-1121.

Kogan, M.N. (1969). *Rarefied Gas Dynamics* (Plenum Press, New York).

Lauga, E., Brenner, M.P., and Stone, H.A. (2007). Microfluidics: the no-slip boundary condition, in *Handbook of Experimental Fluid Dynamics*, Edited: Tropea, C., Yarin, A., and Foss, J.F., Chapter 19, New York, Springer.

Liou, W.W., and Fang, Y. (2005). *Microfluid Mechanics: Principles and Modeling*, McGraw-Hill Professional.

Lockerby, D.A., Reese, J.M., Emerson, D.R. and Barber, R.W. (2004). Velocity boundary condition at solid walls in rarefied gas calculations, *Phys. Rev. E*, **70** (017303).

Lockerby, D.A., Reese, J.M., and Gallis, M.A. (2005). The usefulness of higher-order constitutive relations for describing the Knudsen layer, *Phys. Fluids*, **17**, 100609.

Lord, R.G. (1991). Some extensions to the Cercignani-Lampis gas- surface scattering kernel, *Phys. Fluids*, **3**, 706-710.

Lord, R.G. (1995). Some further extensions of the Cercignani-Lampis gas-surface interaction model, *Phys. Fluids*, **7**, 1159-1161.

Loyalka, S.K. (1971). Approximate method in kinetic theory, *Phys. Fluids*, **14**, 2291-2294.

Loyalka, S.K. (1975). Velocity profile in the Knudsen layer for the Kramer's problem, *Phys. Fluids*, **18**, 1666-1669.

Loyalka, S.K., Petrellis, N., and Storvick, T.S. (1975). Some numerical results for the BGK model: thermal creep and viscous slip problems with arbitrary accommodation at the surface, *Phys. Fluids*, **18**, 1094.

Macrossan, M.N. (2001). ν-DSMC: a fast simulation method for rarefied flow, *J. Comput. Phys.*, **173**, 600-619.

Majumder, M., Chopra, N., Andrews, R., Hinds, B.J. (2005). Nanoscale hydrodynamics: enhanced flow in carbon nanotubes, *Nature*, **438**, 44.

Maurer, J., Tabeling, P., Joseph, P., and Willaime, H. (2003). Second-order slip laws in microchannels for helium and nitrogen, *Phys. Fluids*, **15**, 2613-2621.

Maxwell, J. C. (1877). Book review: A treatise on the kinetic theory of gases, *Nature*, **16**, 242-246.

Maxwell, J.C. (1879). On stresses in rarefied gases arising from inequalities of temperature, *Phil. Trans. R. Soc. London*, **170**, 231–256.

McOwen, R.C. (1996). *Partial Differential Equations: Methods and Applications*, Prentice Hall.

Mitsuya, Y. (1993). Modified Reynolds equation for ultra-thin film gas lubrication using 1.5-order slip-flow model and considering surface accommodation coefficient, *J. Trib.*, **115**, 289-294.

Myong, R.S. (2004). Gaseous slip models based on the Langmuir adsorption isotherm, *Phys. Fluids*, **16**, 104.

Myong, R.S., Reese, J.M., Baber, R.W., and Emerson D.R. (2005). Velocity slip in microscale cylindrical Couette flow: the Langmuir model, *Phys. Fluids*, **17**, 87105.

Neto, C., Evans, D.R., Bonaccurso, E., Butt, H.-J., and Craig, V.S.J. (2005). Boundary slip in Newtonian liquids: a review of experimental studies, *Rep. Prog. Phys.*, **68**, 2859-2897.

Nguyen, N.T., and Wereley, S.T. (2006). *Fundamentals and Applications of Microfluidics*, Boston, Artech House.

Ohwada, T., Sone, Y., and Aoki, K. (1989). Numerical analysis of the shear and thermal creep flows of a rarefied gas over a plane wall on the basis of the linearized Boltzmann equation for hard-sphere molecules, *Phys. Fluids A*, **1**, 1588.

Oran, E.S., Oh, C.K. and Cybyk, B.Z. (1998). Direct simulation Monte Carlo: Recent advances and applications, *Annual Review of Fluid Mechanic*, **30**, 403-441.

Pan, L.S., Liu, G.R., and Lam, K.Y. (1999). Determination of slip coefficient for rarefied gas flows using direct simulation Monte Carlo, *J. Micromech. Microeng.*, **9**, 89-96.

Pan, L.S., Ng, T.Y., Xu, D., Liu, G.R., and Lam, K.Y. (2002). Determination of temperature jump coefficient using the direct simulation Monte Carlo method, *J. Micromech. Microeng.*, **12,** 41-52.

Pantazis, S., and Valougeorgis, D.).2010). Heat transfer through rarefied gases between coaxial cylindrical surfaces with arbitrary temperature difference, *Eur. J. Mech. B/Fluids*, **29**, 494.

Park, J.H., Bahukudumbi, P., and Beskok, A. (2004). Rarefaction effects on shear driven oscillatory gas flows: a direct simulation Monte Carlo study in the entire Knudsen regime, *Phys. Fluids*, **16**, 317.

Pennel, W.O. (1929). A generalization of Heaviside's expansion theorem, *Bell System Technical Journal*, **8**, 482-492.

Perrier, P., Graur, I.A., Meolans, J.G., and Ewart, T. (2011). Mass flow rate measurements in microtubes: from hydrodynamic to near free molecular regime, *Physics of Fluids*, **23**, 042004.

Radtke, G.A., Hadjiconstantinou, N.G., and Wagner, W. (2011). Low-noise Monte Carlo simulation of the variable hard spheres gas, *Phys. Fluids*, **23**¸ 030606.

Pelesko, J.A., and Bernstein, D.H. (2003). *Modeling MEMS and NEMS*, Boca Raton, FL, Chapman & Hall/CRC.

Reese, J.M., and Zhang, Y.H. (2009). Simulating fluid flows in micro and nano devices: the challenge of non-equilibrium behaviour, *J. Comput. Theor. Nanosci.*, **6**, 2061-2074.

Richardson, S.M. (1989). *Fluid Mechanics*, Hemisphere Publishing Corp.

Rjasanov, S., and Wagner, W. (2005). *Stochastic Numerics for the Boltzmann Equation* (Stochastic numerics for the Boltzmann equation), Berlin, Heidelberg: Springer-Verlag Berlin Heidelberg.

Schamberg, R. (1947). The fundamental differential equations and the boundary conditions for high speed slip-flow, and their application to several specific problems, Ph.D. thesis, California Institute of Technology.

Schlichting, H. (1979). *Boundary-Layer Theory*, McGraw-Hill.

Schrag, G., and Wachutka, G. (2002). Physically based modeling of squeeze filmdamping by mixed-level system simulation. Sens. Actuators A, **97-98**, 193.

Shakhov, E.M. (1968a). Approximate kinetic equations in rarefied gas theory, *Fluid Dynamics*, **3,** 156-161.

Shakhov, E.M. (1968b). Generalization of the Krook kinetic relaxation equation, *Fluid Dynamics*, **3,** 142-145.

Sharipov, F. (2011). Data on the velocity slip and temperature jump on a gas-solid interface, *J. Phys. Chem. Ref. Data*, **40,** 023101

Sharipov, F., and Bertoldo, G. (2006). Heat transfer through a rarefied gas confined between two coaxial cylinders with high radius ratio, *J. Vac. Sci. Technol. A*, **24**, 2087.

Sharipov, F., and Kalempa, D. (2007). Gas flow near a plate oscillating longitudinally with an arbitrary frequency, Phys. Fluids, **19**, 017110.

Sharipov, F., and Seleznev, V. (1998). Data on internal rarefied gas flows, *J. Phys. Chem. Ref. Data*, **27**, 657.

Shen, C. (2005). *Rarefied Gas Dynamics Fundamentals, Simulations and Micro Flow*, Springer Berlin Heidelberg.

Shonkwiler, R.,W., and Mendivil, F. (2009). *Explorations in Monte Carlo Methods*, Springer.

Smoluchowski, von M. (1898). Ueberwarmeleitung in verdunntengasen, *AnnalenderPhysik und Chemie*, **64**, 101-130.

Soga, T., and Ooue, K. (2002). On the numerical simulation of rotating rarefied flow in the cylinder with smooth surface, *Proceedings of the 23rd International Symposium on Rarefied Gas Dynamics*, British Columbia, Canada, July 20-25, 210-217.

Sone, Y. (1969). Asymptotic theory of flow of rarefied gas over a smooth boundary I, Proceedings of the 6th International Symposium on *Rarefied Gas Dynamics*, edited by L. Trilling and H. Y. Wachman, Academic Press, New York, 243-253.

Sone, Y. (1973). New kind of boundary layer over a convex solid boundary in a rarefied gas, *Phys. Fluids*, **16**, 1422-1424.

Sone, Y. (2002). *Kinetic Theory and Fluid Dynamics*, Birkhauser, Boston.

Sone, Y. (2007). *Molecular Gas Dynamics: Theory, Techniques, and Applications*, Birkhauser, Boston.

Sone, Y., and Sugimoto, H. (1993). Kinetic theory analysis of steady evaporating flows from a spherical condensed phase into a vacuum, *Phys. Fluids* A, **5**, 1491.

Sone, Y., and Takata, S. (1992). Discontinuity of the velocity distribution function in a rarefied gas around a convex body and the S layer at the bottom of the Knudsen layer, *Transport Theory and Statistical Physics*, **21**, 501.

Sreekanth, A.K. (1969). Slip flow through long circular tubes, Proceedings of the 6th International Symposium on Rarefied Gas Dynamics, edited by L. Trilling and H. Wachman, Academic Press, New York, 667-680.

Sudarsan, A.P., and Ugaz, V.M. (2006). Fluid mixing in planar spiral microchannels, *Lab Chip*, **6**, 74-82.

Sugimoto, H., and Sone, Y. (1992). Numerical analysis of steady flows of a gas evaporating from its cylindrical condensed phase on the basis of kinetic theory, *Phys. Fluids A*, **4**, 419.

Stefanov, S., Gospodinov, P., and Cercignani, C. (1998). Monte Carlo simulation and Navier-Stokes finite difference calculation of unsteady-state rarefied gas flows, *Phys. Fluids*, **10**, 289-300.

Stefanov, S. (2011). On DSMC calculations of rarefied gas flows with small number of particles in cells, *SIAM J. Sci. Comput.*, **33**, 677-702.

Stokes, G.G. (1851). On the effect of the internal friction of fluids on the motion of pendulums, *Trans. Cambridge Philos. Soc.*,**9**, 8-106.

Struchtrup, H. (2005). *Macroscopic Transport Equations for Rarefied Gas Flows*, Springer-Verlag, Berlin.

Struchtrup, H., and Torrilhon, M. (2003). Regularization of Grad's 13-moment-equations: derivation and linear analysis, *Phys. Fluids*, **15**, 2668–2680.

Taheri, P. and Struchtrup, H. (2009). Effects of rarefaction in microflows between coaxial cylinders, *Phys. Rev. E*, **80**, 066317.

Tang, G.H., Gu, X.J., Barber, R.W., Emerson, D.R., and Zhang, Y.H. (2008). Lattice Boltzmann simulation of nonequilibrium effects in oscillatory gas flow, *Phys. Rev. E*, **78**, 026706.

Tibbs, K.W., Baras, F., and Garcia, A.L. (1997). Anomalous flow profile due to the curvature effect on slip length, *Phys. Rev. E*, **56**, 2282-2283**.**

Vargas, M., and Stefanov, S. (2011). Transient heat transfer flow through a rarefied gas confined between coaxial cylinders, *Proceedings on CDROM of 3rd International GASMEMS Workshop (GASMEMS11)*, Bertinoro, Italy.

Veijola, T., Kuisma, H., Lahdenperä, J., and Ryhänen, T. (1995). Equivalent-circuit model of the squeezed gas film in a silicon accelerometer. Sens. Actuators A, 48, 239.

Villani, C. (2002). *Handbook of Mathematical Fluid Dynamics (Vol. 1),* Edited by S. Friedlander and D. Serre, Elsevier Science.

Vinogradova, O.I. (1999). Slippage of water over hydrophobic surfaces, *International Journal of Mineral Processing*, **56**, 31–60.

Wadsworth, D.C. (1993). Slip effects in a confined rarefied gas. I: temperature slip, *Phys. Fluids A,* **5**, 1831-1839.

Wagner, W. (1992). A convergence proof for Bird's direct simulation Monte Carlo method for the Boltzmann equation, *J. Stat. Phys.*, **66**, 1011-1044.

Wagner, W. (2011). Stochastic models in kinetic theory, *Phys. Fluids*, 23, 030602.

Whitby, M., and Quirke, N. (2007). Fluid flow in carbon nanotubes and nanopipes, *Nature Nanotechnology*, **2**, 87-94.

White, F.M. (1991). *Viscous Fluid Flow*, McGraw-Hill.

Wu, L.A. (2008). Slip model for rarefied gas flows at arbitrary Knudsen number, *Appl. Phys. Lett.*, **93**, 253103.

Yuhong, S., Barber, R.W., and Emerson, D.R. (2005). Inverted velocity profiles in rarefied cylindrical Couette gas flow and the impact of the accommodation coefficient, *Phys. Fluids*, **17**, 047102.

Zhang, Y.H, Gu, X.J., Barber, R.W., and Emerson, D.R. (2006). Capturing Knudsen layer phenomena using a lattice Boltzmann model, *Phys. Rev. E,* **74**, 046704.

Zhu, Y., and Granick, S. (2002). Limits of the hydrodynamic no-slip boundary condition, *Phys. Rev. Lett.*, **88**, 106102.

Zhuk, V.I., Rykov, V.A., and Shakhov, E.M. (1973). Kinetic models and the shock structure problem, *Fluid Dynamics*, **8,** 620-625.

CURRICULUM VITAE

Name Surname **:** Ali Dinler

E-Mail **:** ali_dinler@yahoo.com

B.Sc. **:** Istanbul Technical University, Mathematics Engineering

M.Sc. **:** Istanbul Technical University, Informatics Institute, Computational Science and Engineering

Awards:

Marie Curie Fellowship for three years at STFC Daresbury Laboratory in United Kingdom, which is one of the Excellence Centres of UK Research Councils

List of Peer-Reviewed Publications

Journal Papers

Dinler, A., Barber, R. W., Emerson, D. R., Stefanov, S. K. and Orucoglu, K., The effects of S-layer on nonplanar microfluidic gas flows: A critical view on the accuracy of the slip models, **accepted** by *Journal of Computational Theoretical Nanoscience*

Dinler, A., Barber, R. W., Emerson, D. R., Stefanov, S. K. and Orucoglu, K., Role of surface shape on boundary slip and velocity defect, *Physical Review E* 86, 016314, **2012**

Akdag, S., **Dinler, A.**, A new method to estimate Weibull parameters for wind energy application, Journal of Energy Conversion and Management, 50, 1761-1766, **2009**

Unal, G., **Dinler, A.**, Exact linearization of one dimensional Itô equations driven by fBm: Analytical and numerical solutions, Journal of Nonlinear Dynamics, 53, 251-259, **2008**

International Conference Papers

Dinler, A., Barber, R. W., Emerson, D. R., Stefanov, S. K., Velocity Inversion and Predicting velocity slip on Curved surfaces, 28th Rarefied Gas Dynamics Conference, Zaragoza 9-13 July **2012**

Dinler, A., Graur, I. A., Barber, R. W., Emerson, D. R., and Perrier, P., On the role of surface shape in a micro-scale heat conduction problem, J. Phys.: Conf. Ser. 362, 012017 **2012**

Dinler, A., Barber, R. W., and Emerson, D. R., The role of the S-layer on the accuracy of slip models, in Proceedings on CDROM of 3rd International GASMEMS Workshop (GASMEMS11), Bertinoro, Italy, GASMEMS11-5:1-6, **2011**

Dinler, A., Barber, R. W., Emerson, D. R., and Orucoglu, K., Does the Knudsen layer exist over a concave surface?, in Proceedings of the International Symposium on Thermal and Materials Nanoscience and Nanotechnology (TMNN-2011) - ICHMT Digital Library, Antalya, Turkey. Begell House (Publisher), 1-8, **2011**

Dinler, A., Hasan, C., Orucoglu, K., and Barber, R. W., On an efficient Marie Curie initial training network, in Proceedings on CDROM of the International Conference on Mathematical Finance and Economics (ICMFE-2011), Istanbul, Turkey. ITU Foundation Press (Publisher), ISBN 9789755613994, 336-342, **2011**

Dinler, A., Barber, R. W., and Emerson, D. R., Can the validity of slip models be extended into transition regime?, in Proceedings on CDROM of 2nd International GASMEMS Workshop (GASMEMS10), Les Embiez, France, GASMEMS2010-GM04:1-8, **2010**

Dinler, A., Barber, R. W., and Emerson, D. R., The effects of curvature on nonplanar oscillatory microflows, in Proceedings on CDROM of 2nd European Conference on Microfluidics (µFlu'10), Toulouse, France, S. Colin and G. L. Morini, Eds. SHF (Publisher), ISBN 978-2-906831-85-8, µFLU2010-110:1-8, **2010**

Gulcat, U., **Dinler, A**., Parallel solution of flows with high velocity and/or enthalpy gradients, *Lecture Notes in Computational Science and Engineering***,** 67, 425-432, Springer, **2009** (Parallel Computational Fluid Dynamics Conference, Parallel CFD 2007, Antalya)

National Conference Papers

Dinler, A., Orucoglu K., Efficient solution of parameter-dependent 3D Poisson equation with a spectral method, *XVI. National Mechanics Conference*, Kayseri, **2009**

Gulcat, U., **Dinler, A**., Stability analysis of a 1D flow with high temperature gradients, *XVI. National Mechanics Conference*, Kayseri, **2009**

Orucoglu K., **Dinler, A.**, Ideas behind Green's functional, *XVI. National Mechanics Conference*, Kayseri, **2009**

Akdağ, S., **Dinler, A.**, Calculation of wind energy cost with Weibull distribution for various wind turbines, *IV. Ege Energy Symposium*, Izmir, **2008**

Oruçoğlu, K., **Dinler, A.**, Fundamental and numerical solutions of second-order differential equations with nonlocal and intermediate-point conditions, *XXI. National Mathematic Symposium*, Istanbul, **2008**

Gulcat, U., **Dinler, A.**, Parallel solution of a 3D flow with high velocity and/or enthalpy gradients, *XV. National Mechanics Conference*, Isparta, **2007**

Akdağ, S., **Dinler, A.**, Menteş, Ş., Analysis of wind characteristics, *IV. Renewable Energy Resources Conference*, Gaziantep, **2007**

Technical Note

Dinler, A., Orucoglu, K., High performance implementation of block Krylov methods, *Istanbul Technical University Physical Sciences Bulletin*, 7, 159-165, **2009**